

UNCLASSIFIED

AD

426664

DEFENSE DOCUMENTATION CENTER

FOR

SCIENTIFIC AND TECHNICAL INFORMATION

CAMERON STATION, ALEXANDRIA, VIRGINIA



UNCLASSIFIED

NOTICE: When government or other drawings, specifications or other data are used for any purpose other than in connection with a definitely related government procurement operation, the U. S. Government thereby incurs no responsibility, nor any obligation whatsoever; and the fact that the Government may have formulated, furnished, or in any way supplied the said drawings, specifications, or other data is not to be regarded by implication or otherwise as in any manner licensing the holder or any other person or corporation, or conveying any rights or permission to manufacture, use or sell any patented invention that may in any way be related thereto.

64-6

RTD
TDR
63-3080

RTD TDR-63-3080

CATALOGED BY DDC
AS AD NO.

426664

426664

BEHAVIOR OF PLASTICS UNDER IMPULSIVE STRESS

December 1963

TECHNICAL DOCUMENTARY REPORT NO. RTD TDR-63-3080

Research and Technology Division
AIR FORCE WEAPONS LABORATORY
Air Force Systems Command
Kirtland Air Force Base
New Mexico

JAN 14 1964

Project No. 5776, Task No. 58043

This research has been funded by the
Defense Atomic Support Agency under WEB No. 15.027

(Prepared under Contract AF 29(601)-4418
by D. G. Flom, F. A. Lucy, and H. W.
Semon, Space Sciences Laboratory,
Missile and Space Division, General
Electric Company, Philadelphia, Penna.)

Research and Technology Division
Air Force Systems Command
AIR FORCE WEAPONS LABORATORY
Kirtland Air Force Base
New Mexico

When Government drawings, specifications, or other data are used for any purpose other than in connection with a definitely related Government procurement operation, the United States Government thereby incurs no responsibility nor any obligation whatsoever; and the fact that the Government may have formulated, furnished, or in any way supplied the said drawings, specifications, or other data, is not to be regarded by implication or otherwise as in any manner licensing the holder or any other person or corporation, or conveying any rights or permission to manufacture, use, or sell any patented invention that may in any way be related thereto.

This report is made available for study upon the understanding that the Government's proprietary interests in and relating thereto shall not be impaired. In case of apparent conflict between the Government's proprietary interests and those of others, notify the Staff Judge Advocate, Air Force Systems Command, Andrews AF Base, Washington 25, DC.

This report is published for the exchange and stimulation of ideas; it does not necessarily express the intent or policy of any higher headquarters.

Qualified requesters may obtain copies of this report from DDC. Orders will be expedited if placed through the librarian or other staff member designated to request and receive documents from DDC.

RTD TDR-63-3080

FOREWORD

The authors express their appreciation to Dr. W. T. Barry, who was principal investigator during the first half of this program, and Dr. J. P. Berry for their continued interest and helpful suggestions. The valuable assistance of Mr. T. F. Geib, Mr. J. C. Fries, and Mr. E. G. Muziani in the experimental work and data reduction is also gratefully acknowledged.

ABSTRACT

Under brief impulsive loading by flying plates, fractures formed in rubbery resins differ from those formed in glassy resins. The latter usually crack by spreading of well-defined ridged disks roughly parallel to the wave front. Fractures in rubbery resins may be bursts of feathery cracks, ridged cones, or nearly featureless disks. The fracture orientation usually departs widely from that of the wave front. The fracture threshold for a glassy resin was found to lie between 0.4 and 0.6 kb; whereas the threshold for a chemically similar rubbery resin lay between 1.0 and 1.4 kb.

Changes of pulse height and pulse shape with travel were found to be rapid within the first pulse length but quite slow thereafter. Pulse steepness was shown to be lost faster in rubbery than in glassy material. The observations were made with quartz transducers. Electron and optical micrography of fracture surfaces, x-ray diffraction, and measurements of Poisson's ratio and compressibility under dynamic conditions all contributed to an explanation of differences in strength and type of fractures.

PUBLICATION REVIEW

This report has been reviewed and is approved.



RICHARD C. BRIGHTMAN
Lt USAF
Project Officer



JOHN J. NEUER
Colonel USAF
Chief, Physics Branch



PERRY L. HUIE
Colonel USAF
Chief, Research Division

CONTENTS		PAGE
	ABSTRACT	iii
1.	INTRODUCTION	1
2.	EXPERIMENTAL	4
	a. Impacting with a Compressed-Air Gun	4
	b. Quartz Crystal Transducer Technique	14
	(1) Theoretical basis	14
	(2) Circuitry and geometry	19
	c. Light Transmission Technique	21
	d. Framing Camera Technique	24
3.	DISCUSSION OF RESULTS	28
	a. Equations of State	28
	b. Pulse Profiles in Rigid Resin	40
	(1) General description	40
	(2) Comparison of quartz data with equation of state	42
	c. Pulse Profiles in Rubbery Resin	44
	d. Light Transmission Results	44
	e. Fracture Formation	65
	(1) Fractures in rigid BC323 resin	65
	(2) Fractures in rubbery BC326 resin	66
	(3) Comparison of rigid and rubbery resins	95
4.	SUMMARY	103
	REFERENCES	106
	DISTRIBUTION	108

1. INTRODUCTION

The purpose of this program was to obtain a greater understanding of the process of fracture in plastics under short-duration stress pulses. The basis for this objective was recognition that many material properties are highly dependent on rates of loading. This is particularly true for polymers.

Since the usual materials-testing machines are limited to relatively low strain rates, the flying-plate technique was adopted for producing the short-duration, high-pressure pulses. This technique consists basically of allowing a driver plate to impact a target at known velocity; thus causing a shock-fronted compression pulse to run into the target. By varying the impact velocity, the driver and target densities, and the shock velocities, the magnitude of the shock pulse can be varied over a broad range. Since the pulse duration is equal to the time required for the shock in the driver to travel to the rear of the driver, to be reflected as a tensile pulse, and then to return to the impact surface, it is apparent that pulses of a few microseconds or even less than a microsecond can be produced by this technique. Early in this program, it was found that the most reproducible method of propelling the driver plates at the velocities required (~ 30 to 150 m/sec) was by use of a compressed-gas gun. Details of this procedure have been discussed in the Interim Final Report for the present program (Ref. 1).

The materials chosen for the program were based on the GE Century Series Resins, which are clear, castable ablation materials. Because these materials are homogeneous and isotropic, the number of complicating variables in the study of possible damage behavior is reduced. Their clarity allows easy inspection of quality and damage.

Chemically, these resins are based on a char-forming substructure which is primarily phenolic. To this substructure glycidyl ether groups are attached, which are cured by reaction with a liquid carboxylic acid anhydride. Certain long chain polyether glycols and other additives are added to provide internal plasticization.

The two materials studied in most detail were resins designated as BC323 and BC326. The BC323 contained no flexibilizer, and exhibited glassy behavior below 100°C . The BC326 contained sufficient plasticizer to make it rubbery at room temperature (20°C). The mechanical properties for these materials and for a standard Century formulation, 123C, are given in Ref. 1, together with details of preparation.

During the first phase of the program it was found that the impact behavior of BC326, the rubbery material, differed radically from that of BC323, the more glassy type. Although a threshold initial impact pressure (IIP) for fracture for BC326 could not be determined, because of difficulty in

obtaining a reliable equation of state for that material, the impact velocity required for fracture was much higher than that required for fracture in BC323. This was thought to be the result of greater energy dissipation within the rubbery material leading to a lowering of the shock-pulse amplitude. However, the present work has shown that the equation of state and pulse propagation in BC326 are not widely different from those in BC323; so that other factors also affect the spall resistance.

The fractures obtained in the glassy, more rigid materials were well-defined circular disks, having central initiation sites of irregular shape. Both the fracture disk and initiation site diameters increased with increasing driver thickness.

The fractures obtained initially in the rubbery material differed markedly from those in the glassy materials, more closely resembling what might be expected from a tearing process. The fractures were conical and in the form of rosettes. Only a few specimens were produced, however, and, as will be discussed in more detail presently, fractures obtained in BC326 during the second phase of the program were often found to be devoid of features visible to the unaided eye.

Particularly within the glassy materials, on which most effort was concentrated during the first phase of the program, the disk-type fractures were roughly parallel to the rear surface of the target and in a plane approximately one driver-plate thickness from the rear surface. This is the type of primary fractures one might expect by considering the propagation of a compression pulse through the target and reflection from the rear surface as a tensile pulse. If the material were ideally homogeneous and the initially rectangular compression pulse did not change shape, the superposition of reflected and advancing pulses would result in a net tensile stress which would reach a maximum value (equal, in the case of a straight stress-strain plot, to the initial compressive stress) instantaneously in a plane one-half the pulse width in from the rear surface. Actually, however, the materials were not ideally homogeneous and the pulses probably did not remain perfectly rectangular. Hence, the tensile stress in the target material would not change from zero to a maximum value instantaneously but would do so in a finite time. As in gases, the characteristics (plots of particle position vs time) fan out during rarefaction, causing the wave front to become less steep. However, breaks or inflections in the stress-strain plot, which cannot occur in gases, mark transitions of a solid between elastic and plastic behavior, or transitions between different types of bonding. These inflections, produced by an increase in wave speed for the later, stronger, components of resultant tension, can produce steep-fronted portions of tension-wave profile, affecting the fracture behavior.

It was obvious that since both the initiation site and disk diameters varied with driver-plate thickness, these were somehow dependent on the duration and perhaps the shape of the stress pulse. It was especially desirable to know more about the stress within the region where damage occurred. To this end, efforts during the second phase of the program were concentrated on measuring stress profiles, using a quartz crystal transducer method recommended by AFWL and developed initially by Sandia Corporation (Ref. 2). Attempts were made to supplement these measurements with an optical-density technique.

Further studies of fracture in the more rubbery material were also made to determine more closely the differences in fracture morphology between this resin and the more glassy material.

2. EXPERIMENTAL

a. Impacting With a Compressed-Air Gun

As stated in the Introduction, the method of impacting in this program was basically an extension and refinement of the flying-plate technique, using a compressed-air gun to provide the necessary relative velocity between target and driver plate. This technique was discussed in detail in Ref. 1 and will be discussed here only where necessary to provide a background for the changes that were necessary to improve the technique.

Measurement of the shock-pulse profile within a target material without introducing factors that excessively distort the pulse is a formidable problem. It is especially complicated if the observer is interested in the tensile phase of the shock pulse, as one must be to understand fracture. Furthermore, if the observer is interested in the fine structure of the shock pulse, the measuring system must have extremely fast response.

Because of the great difficulty in making direct measurement of shock parameters at the point of failure, it was decided that measurements should first be made to try to determine how a shock pulse would change shape in passing through various thicknesses of target material. This can be done by using an experimental technique in which a pulse of known shape is introduced into the front face of a target and is measured at the rear surface of the target by the use of an x-cut quartz crystal (Ref. 2). Thus by observing how the pulse changes in going through various thicknesses of target, one should be able to get a much better understanding of the mechanism of pulse propagation. Since this technique embodies some uncertainty in simultaneity of impact on the target face where the shock pulse is generated and at the interface between the target and crystal, it is highly desirable to be able to make several measurements at different thicknesses on the same target. This required a driver and target system capable of producing the shock pulses and large enough to accommodate several crystals. At the time the program started, General Electric had the only large-diameter (six inch) compressed-air gun in use for shock pulse study work. This gun is shown to the right of center in Figure 1. With a gun of this size, it appeared possible to mount as many as four crystals on a single target. Thus, by comparing the signal produced at different distances from the impact face of the stepped target, uncertainties in the initial generation of the shock pulse and in the pulse travelling through the interface between crystal and target become relatively unimportant; since one can assume they are comparable for all depths.

Unfortunately the electrical output from a quartz crystal is a function of the tensorial average strain in the crystal between the electrodes. Thus unless the shock pulse being studied is truly planar and parallel to the faces of the crystal, the electrical output of the crystal will be a distorted replica

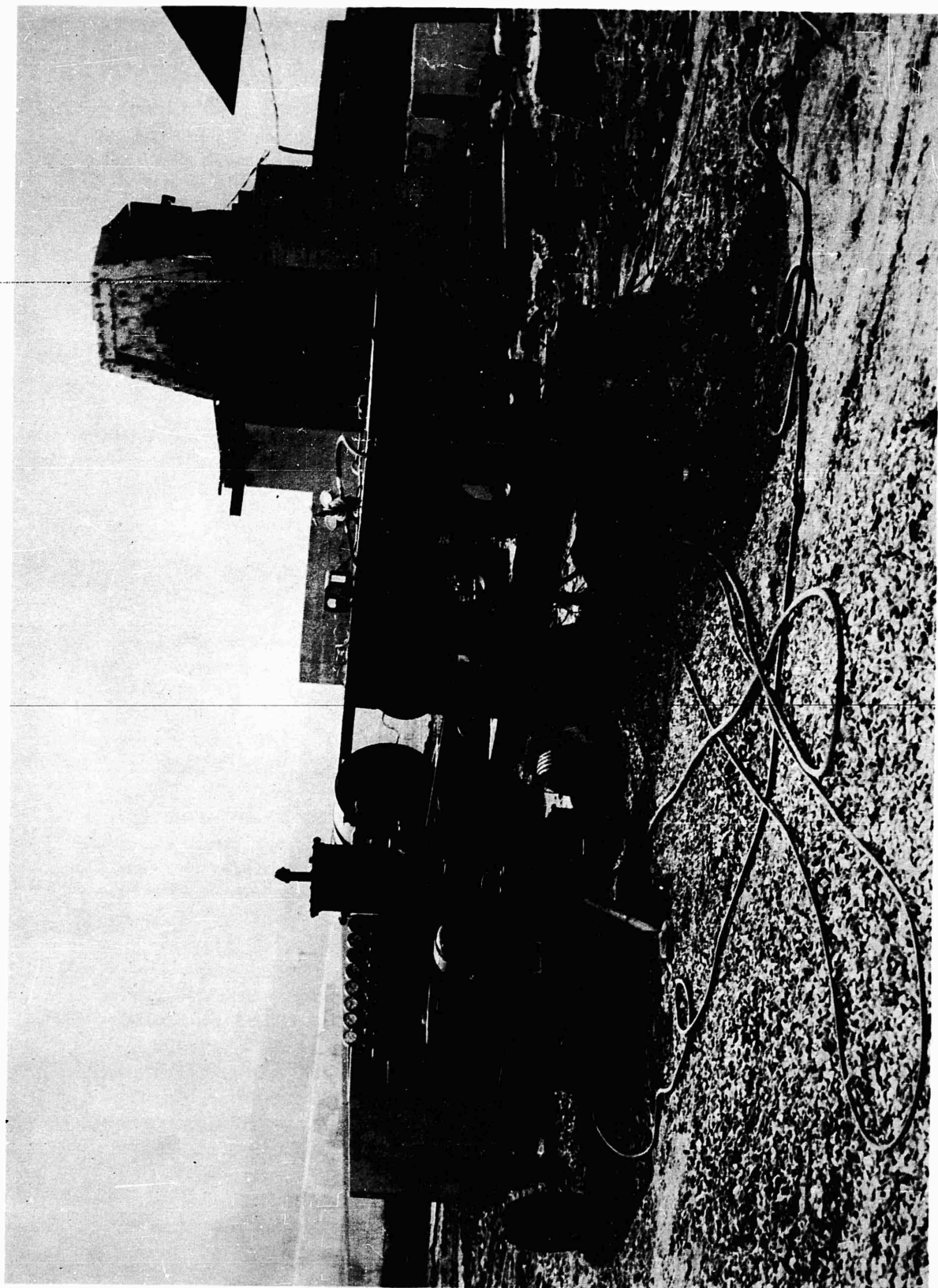


Figure 1. The G.E. Compressed Air Gun

of the strain seen by the crystal. With the crystals used in this program (1.250-inch diameter and 0.375-inch thick) it takes only about 1.66 microseconds for a shock pulse to run entirely through the crystal. It was immediately evident that unless the impact asimultaneity of the driver plate on the target was less than 1.66 microseconds, part of the crystal would be first sensing compression after the release wave had entered the back face of another part of the crystal. Thus it would be essentially impossible to interpret the electrical output of the crystal in terms of the strain that produced the output; since various different tensor fields can produce identical space-integrated potentials at the electrodes. Thus, unless the stress conditions are simple, the electrical record cannot be unequivocally converted to a stress record. Securing the necessary high impact simultaneity proved to be a very formidable problem.

It can be shown readily that the impact asimultaneity, S , achieved by a given target and driver combination is

$$S = \frac{D \cdot \tan \Delta}{u} , \quad (1)$$

where D = the diameter over which asimultaneity is being measured,

Δ = the error angle between target and driver at first contact,

u = the relative velocity between target and driver.

Here both target and driver are assumed to be perfectly plane at first contact. Expressing the above formula in a slightly different way, it may be said that the asimultaneity obtained is proportional to the diameter over which the asimultaneity is measured, proportional to the tangent of the error angle and inversely proportional to the relative velocity at the time of impact, still assuming target and driver are perfectly plane. Thus, the larger the gun, the more difficult it is to get high impact simultaneity over the entire target surface. Furthermore, the lower the impact velocity, the more difficult it is to achieve high impact simultaneity.

It can be readily appreciated that of the three factors that determine the impact simultaneity, two factors (the diameter over which high impact simultaneity is desired and the impact velocity) are more or less fixed by the design of the experiment. There may be some question as to how much of the area of impact requires good simultaneity. At first glance it would appear that it need be no larger than the face of a single crystal and perhaps only as large as the area inside the guard ring on the crystal. This is not quite the case. Outside the cylinder based on the output electrode, the electrical dipole moment in a volume element of shocked quartz has progressively less effectiveness in inducing charge on the electrode. For a dipole, the effect drops with the inverse cube of the slant range and with

the reduction in solid angle subtended by the obliquely seen disk of the electrode, as well as with the reduction in the scalar product of the moment vector by the position vector of the volume element relative to an area element of the electrode. Thus an element of quartz close to the target-crystal interface and only 1 cm distant from the axis would have its effect reduced, relative to an element on the axis, by a factor of 0.171 for the range effect, and by about $(2)^{1/2}$ for each of the other effects, for a total reduction to 0.08 times the effect of an axial element. Therefore, a general tilt producing an asimultaneity of 0.20 μsec , say, over the diameter of the output electrode would have about the effect of an asimultaneity of 0.22 μsec over the electrode, if there were simultaneity everywhere else. Since, at impact speeds of interest, this tilt makes a difference of less than 0.01 mm in position along the gun axis, and since errors of target and driver flatness exceed 0.01 mm, it would be pedantic to compute the integrated effect more exactly.

In regard to the desired impact velocity, it was essential to work in the region where fractures were just beginning to form; since the purpose of the program was to try to understand the mechanism of formation of such fractures. For the two plastic materials of most interest in this program, this meant working in the range of 0.03 mm/ μsec (100 feet per second) impact velocity.

The error angle is determined basically by geometric considerations that primarily involve the degree of precision to which the gun bore can be made to approach a rigid perfect cylinder, the necessary clearance between the gun bore and the sabot, the shape, precision and rigidity of the sabot, and the precision to which the target is initially aligned parallel to the driver plate. It should be noted that any departure from perfect planarity in either the target or the driver plate may degrade the simultaneity in a manner essentially similar to an increase in error angle. For practical reasons, there are rather firm limits on each of these factors. It is of considerable interest to put some numbers into the calculations to see how critical these limits really are.

Since the damage threshold for BC323 plastic occurs for an impact velocity of approximately 0.03 mm/ μsec , an error exceeding 0.05 mm will permit the leading edge of the shock to pass entirely through the first-struck part of the crystal before the wave front traverses the diameter of the entrance face of the crystal. Thus, if the central 2 cm of the driver and target plate each depart from flatness by as much as 0.025 mm (0.001 inches), the impact simultaneity may be unsatisfactory even if the average angular error is reduced to zero. It should be noted that this flatness requires the damping out of deformations from any buckling that might occur as a result of the target assembly being accelerated in the gun.

In view of the close tolerance required on flatness, a check was made to see whether or not the surface roughnesses of the as-molded targets might lead to difficulty in simultaneity. Surface roughness measurements with a Talysurf stylus and with a multiple-beam interference microscope were therefore made. Photographs of representative traces obtained with the former are shown in Figure 2. Although the localized roughness was greater with the stylus moving across mold machine marks than moving along mold machine marks, even the worst condition did not result in a CLA roughness of more than 7 microinches. This appeared to be well within the required limits just discussed.

Photographs of interference fringes across as-molded BC323 are shown in Figure 3. These pictures were obtained in a conventional microscope utilizing an interference objective (Watson Company). The results corroborate those obtained with the Talysurf instrument and indicate that the roughnesses observed were not excessive for good simultaneity.

More important than the surface roughness was the lack of parallelism in the surfaces of molded targets. This was probably due, among other factors, to uneven shrinkage during cure. On some targets the difference in thickness from one corner to the other amounted to several mils. After this observation, both impact and rear surfaces of all targets were machined prior to impact.

It is assumed that simultaneity is necessary over a diameter of 7.5 cm (two 1.250-inch diameter crystals with a 0.5-inch space between them) the maximum allowable tilt angle is

$$\tan^{-1} \frac{.0020}{3.0} = \tan^{-1} .00066.$$

This angle can result from imperfect initial alignment, lack of perfect rigidity in the sabot, or sabot tilt resulting from clearances necessary for proper gun operation. Considerable effort was expended to reduce each of these factors to an absolute minimum.

The General Electric compressed-air gun as originally constructed utilized a piece of "Rockrite" tubing for the barrel that was cold finished to an inside diameter of 6.00 inches $\begin{smallmatrix} +0.000 \\ -0.010 \end{smallmatrix}$ inches. This tubing was not machined on the inside diameter after assembly, except to remove distortions resulting from welding the flanges to the end of the gun tube. During the course of the present program, the gun barrel was bored out to an inside diameter of 6.000 inches $\begin{smallmatrix} +0.000 \\ -0.001 \end{smallmatrix}$ inches, for a tenfold reduction of allowed fluctuation. This was done after all welding on the gun tube was completed and after the welds were aged to the point of good stability. Thus, the bore of the gun was probably about as precise as economically possible for a bore as large as six inches. This change helped but still did not give adequate simultaneity.

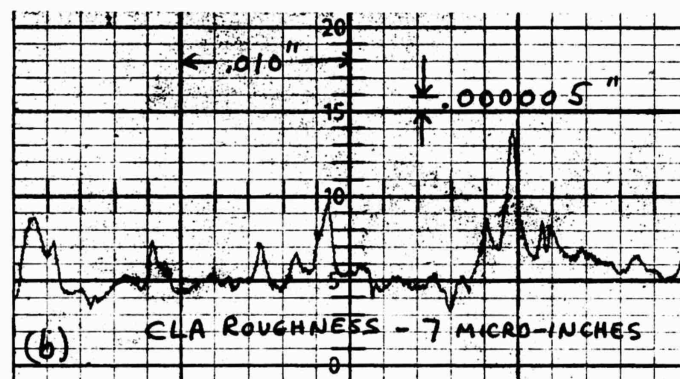
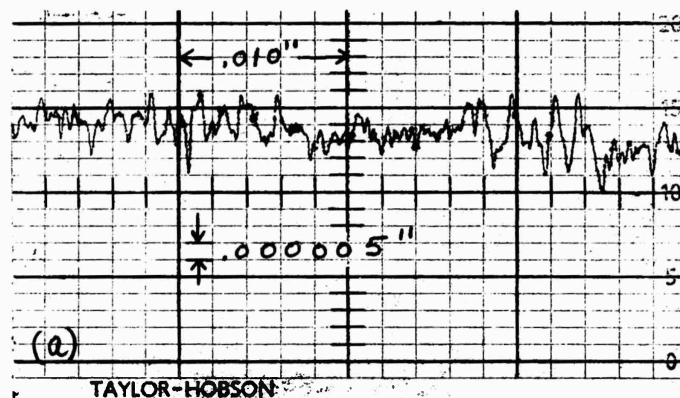
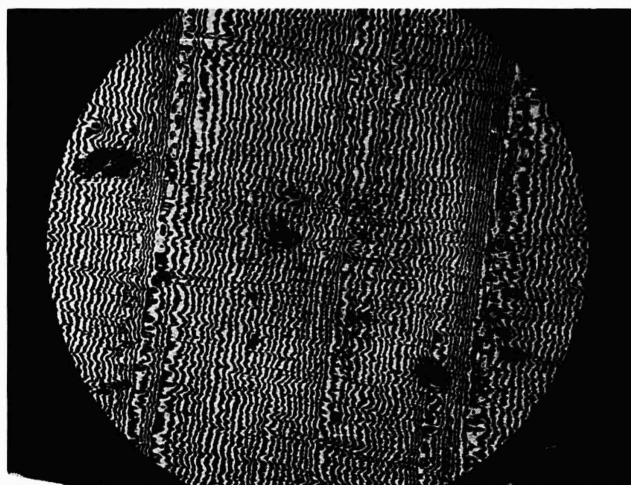
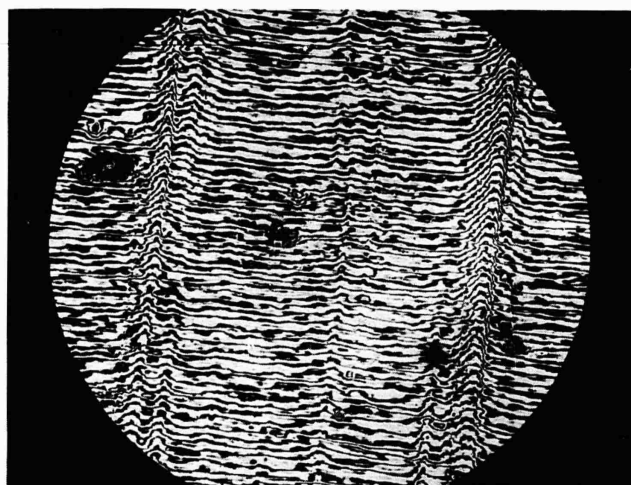


Figure 2. Talysurf Roughness Measurements of As-Molded BC323
 (a) Stylus Moving with Mold Machine Marks
 (b) Stylus Moving Across Mold Machine Marks



(a)



(b)

Figure 3. Interference Fringes (Hg Line) On a Surface of "As-Molded" BC323. (a) Fringes Parallel to Mold Machine Marks, (b) Fringes Perpendicular to Mold Machine Marks. Magnification 65x

The next step in the quest of better simultaneity was to attempt to improve the initial alignment of target and driver plate. After considerable thought about methods of doing this, including even consideration of rather complex optical techniques for setting alignment, it was decided that the best approach would be to bring the sabot to the impact point in the gun and then to mount the target in the gun in such a way that it was in contact over the face of the driver and so that it would not shift position when the sabot was pulled back to firing position at the rear of the gun. This was accomplished by mounting the target on a rigid Lucite plate in the dump tank at the end of the gun. A thin metal strip approximately 4 cm wide was attached to the target so as to protrude 2.5 cm beyond the target and to extend around $3/4$ of the target circumference. This strip, combined with the target rear surface and the Lucite plate, formed an empty pocket or chamber. The target was attached with studs in such a way that it was free to move perpendicularly away from its Lucite holder. After the Lucite was securely fastened in the dump tank, the driver was brought into contact with the target. Quick-setting polyurethane foam was then poured into the target chamber, forcing intimate and parallel contact between driver and target as the foam expanded and hardened. Once the foam hardened, which required about twenty minutes, the sabot with the driver was pulled back into firing position. Figure 4a shows a little more of how that was done. It was recognized, of course, that such an approach was practical only if the sabot did not rotate in proceeding down the bore of the gun. Tests were performed to measure sabot rotation and it was established that the sabot did not rotate detectably: grease pencil marks on the sabot printed on the target within 1° of the original azimuths.

While the use of the foam plastic mounting technique was partially successful, it was still not so satisfactory as might have been desired. As Table I shows, some asimultaneities were far outside tolerance. An attempt was made, therefore, to try to achieve satisfactory results by a somewhat more convenient method. A system was devised in which the target, or driver plate in some instances, was supported by four screws in a plastic cross fixture in such a manner that each of the four screws could be adjusted individually to provide the appropriate positioning. This is shown in Figure 4b. This technique was used in essentially the same manner as described with the foam, except that the nuts on the four screws were adjusted until the proper target-driver alignment was achieved.

Measurements of simultaneity were made, using flush pins projecting through the target. The results of these tests using the rebored gun and after alignment of the target are included in Table I together with results of other procedural shots.

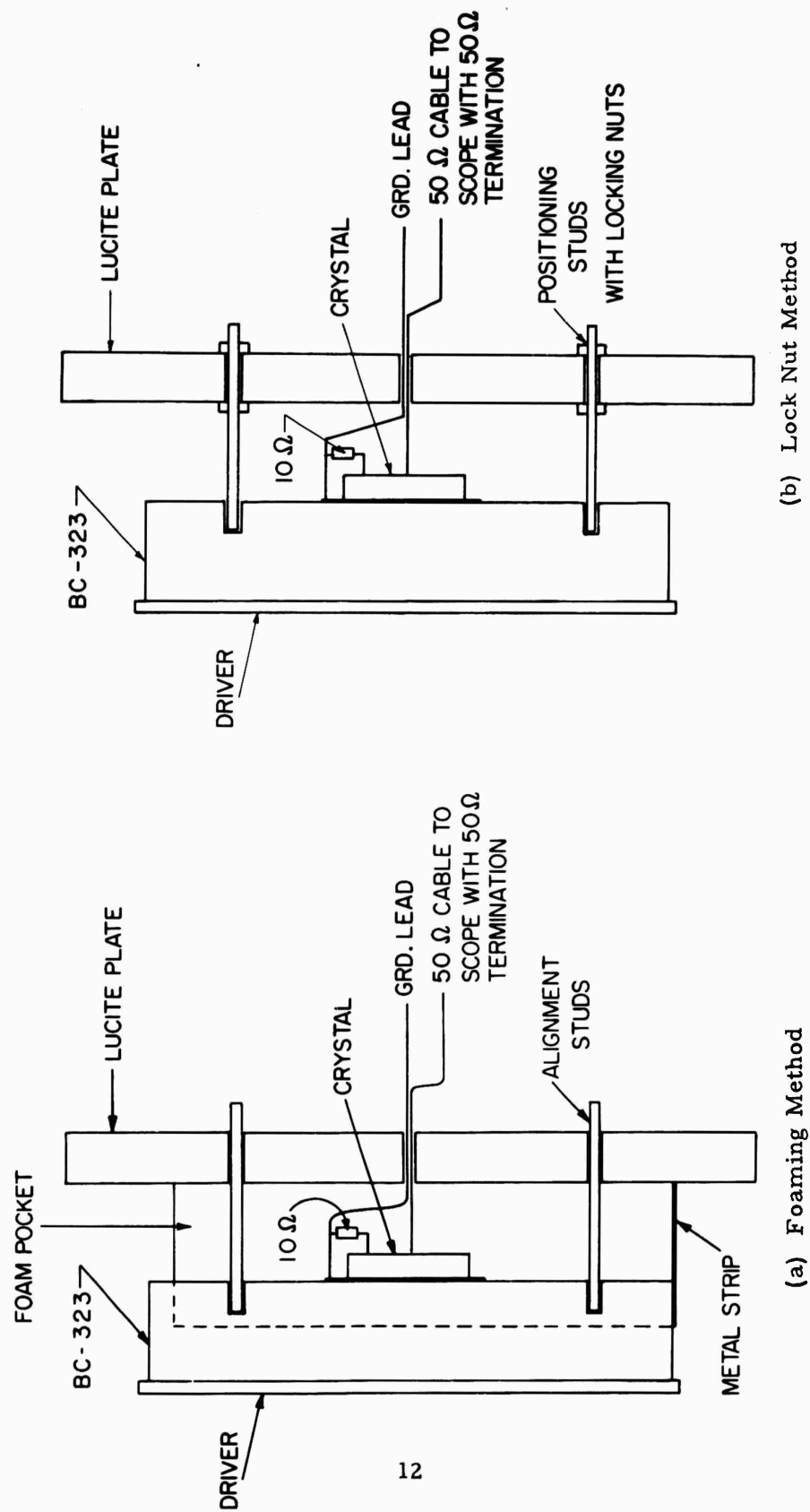


Figure 4. Target and Crystal Assembly During Alignment Prior to Impact Shot

TABLE I

PROCEDURAL IMPACT SHOTS IN REBORED GUN

Serial	Target	Driver	Sabot Vel. (ft/sec)	Sabot Vel. (mm/ μ sec)	Gas Pressure (Microns)	Max Asimultaneity (μ sec)	Tilt Angle	Remarks
1127	1"BC323	3/8" Al	317	0.097	5	7.3	5° 12'	(Target Positioned by foam method)
1129	1"BC323	3/8" Al	313	0.095	15	70	5° 4'	(Target Positioned by foam method)
1136	1"BC323	3/8" Al	303	0.093	25	79	4° 45'	(Target Positioned by foam method)
1140	1"BC323	3/8" Al	308	0.094	10	0.5	1° 32"	(Target Positioned by lock nut method)
1144	1"BC323	3/8" Al	294	0.090	25	2.3	9° 28"	(Target Positioned by lock nut method)
1177	1/4"BC323	1/8" Al	356	0.109	250	0.2	0° 42"	(Non-quadratic array: 4 pins on a radial arm position)
1182	Probe Board	1/8" Al	Not measured expected 0.05		75	2.1	3° 22"	(All aluminum cylin- drical sabot, welded aluminum tubing)
1241	None	None	Not measured expected 0.095		35	---	---	(Contact impedance check of moving crystal. Balsa pedestal. Clean, smooth closure of 6 v in less than 0.1 μ sec.)

b. Quartz Crystal Transducer Technique

(1) Theoretical basis

When a shock wave enters a piezoelectric quartz crystal, the dipole moment density (polarization) changes in the region behind the shock front. The affected volume increases with time as the wave traverses the crystal, with a consequent increase of polarization which depends on the volume swept over and on the input stress as a function of time. The piezoelectric polarization induces charges $+Q$ and $-Q$ on electrodes applied to the input and output crystal faces. These charges correspond to a voltage V which satisfies $Q=CV$, C being the capacitance of the crystal-electrode combination. The overall effect is not readily calculable, and is consequently described empirically, in terms of the coulombs of charge produced on a given area by a given force. This piezoelectric "constant" is 0.0204 microcoulomb per cm^2 for each kb of pressure for low pressures in the range $0 < P < 21$ kb, increasing to 0.0216 for high pressures (Ref. 2). Our work has remained well within this 21kb pressure range.

For an X-cut crystal all at the same pressure, the volume of polarized material varies directly as the thickness, but the electrical capacitance of the gauge varies inversely with thickness. Therefore, as long as the diameter is relatively large, Q , V and the piezoelectric constant are independent of thickness.

If the quartz is not stressed beyond its elastic limit, and if the pulse is 1-dimensional along the quartz X-axis, the stress profile does not change with travel through the crystal. Also, the history of the stress at any plane of atoms parallel to the wave front is the same as that at any other such plane of atoms. That is, within the quartz during the first transit of the pulse, the shock wave is assumed to be a steady disturbance, and

$$c_0 \left(\frac{\partial \sigma}{\partial x} \right)_t = \left(\frac{\partial \sigma}{\partial t} \right)_x, \quad (2)$$

where c_0 is dilatational wave speed, σ is stress, t is time and x is position in terms of (Lagrangian) coordinates moving with the material particles.

The total electric displacement (electric flux density) is

$$\underline{D} = \epsilon_0 \underline{E} + \underline{P}, \quad (3)$$

where \underline{E} is the electric field defined in terms of the potential gradient, i.e., the force experienced by a test charge, thus in terms of the electromotive force or voltage induced on the electrodes, \underline{P} is the integral of the normal components of the polarization produced by the pressure wave and that induced in the rest of the system, and ϵ_0 is the electric inductive capacity of

free space. Clearly, the same \underline{P} can result from different electric moment distributions; so that \underline{P} indicates a unique pressure distribution only if the latter is of a specified simple type. If \underline{P} is taken to be only the piezoelectric polarization, and if the wave front is perfect, then ϵ_0 in (3) should be replaced by ϵ_{xx} , the component of the electric inductive capacity of quartz normal to the gauge faces. It should be borne in mind that most solids are anisotropic. In particular, the mechanical and electrical properties of quartz should be expressed in tensor form, especially when computations are being made. In this report, therefore, any mention of pressure implies the appropriate component of the stress tensor.

If the electrodes are connected by a high-impedance path, i. e., an open circuit or a connection of which the impedance is well above 1000 ohm, the voltage developed during the first transit will describe the time integral of the polarization. In particular, if the pressure were to be raised to some P_{\max} all across the crystal and held there, the integrated charge would be characteristic of the total polarization of the whole crystal, thus of the pressure reached after the transients had damped out. This is the usual employment of a piezoelectric transducer. By Equation (2), the time derivative of the integrated charge during the first transit of the pressure wave would be proportional to the stress, as a function of time, at the input crystal face. If this stress were maintained constant, the amount of material polarized to a given extent (hence the polarization) would rise at a constant rate, while if the pressure at the input declines, the increase of polarization with time will also be less rapid, and if a tension develops at the input face, the integral of the normal component of the polarization will fall.

Thus a possible way of studying a pulse profile would have been to record the voltage produced as a function of time and then find its derivative, which would vary with stress per unit time as long as the crystal is in contact with the material through which the wave is being introduced. If the contact is broken, the subsequent oscillation of the crystal depends upon the properties of quartz, rather than of the material through which the pulse was introduced. Release from both surfaces of the crystal at once would produce a negative polarization as soon as the release waves had covered enough of the crystal, culminating in a negative value about equal to the maximum positive value reached earlier.

High impedance circuits give records which are not readily converted to pressure, and also are troubled by reflections and inductive pickup of noise. For the pressures of interest, the voltage developed would be many kv, which is inconveniently high. If, on the other hand, the electrodes are connected by a low-impedance path, the current through this will be $A dD/dt$, where A is the electrode area. That is, the crystal acts as a current generator, and the effects are studied by observing the voltage drop across a non-inductive resistor carrying this current.

The term in D involving the field strength can be expressed in terms of the capacitance C , and its effect on the current in terms of the RC time constant. The polarization can be expressed in terms of the stress, the volume swept over by the wave in a given time, and the piezoelectric constant. The result, together with some discussion, has been given in Ref. 2. The coaxial cable used in our work has a capacity of about 100 pf/m; whereas roughly 10^{-7} coulomb is made available by shocking the crystal, i.e., a thousand times the amount needed to charge 2 meters of the cable to 5v. It therefore seems appropriate to put the electrode-shunting resistor at the oscilloscope rather than at the crystal, as shown in Figure 1 of Ref. 2. The circuit used in the present work is shown in Figure 5 of this report. If the resistor is chosen equal to the characteristic cable impedance, it prevents the reflection which would otherwise occur at the oscilloscope termination. Cable charging, with $RC = 0.01 \mu\text{sec}$, should make the measured rise only very slightly less steep than the actual rise. The rise time ($0.03 \mu\text{sec}$) of the oscilloscope itself will have a similar and somewhat more marked effect.

Since the system time constant is only about $0.04 \mu\text{sec}$, most of the observed rise time must come from actual slope and asynchronicity of the wave front. In turn, the asynchronicity can come partly from impact asynchronicity and partly from inhomogeneity of the sample. This was discussed in Section 2a. Since the transit time of the crystal is $1.66 \mu\text{sec}$, records which do not peak well before this are hard to interpret, especially in the decay phase. It is further apparent that if $3.33 \mu\text{sec}$ is required for a double transit, the crystal will oscillate at 300 kc if detached from the plastic; whereas the frequency of oscillation of quartz still bonded to a target will generally differ (Ref. 9). Superposed on the 300 kc oscillation will be reflections of the original pulse from the crystal boundaries, including the cylindrical side, with consequent complication of the piezoelectric output. Altogether, it appears best to limit interpretations to the first $1.66 \mu\text{sec}$; since boundary effects make the later part of the record very difficult to interpret. Further, the pulses are not true shocks. Because of preferential attenuation of the higher Fourier components (Ref. 9), we can expect to find significant stress decay in the tail of a pulse only if the input pulse is decidedly shorter than $1.66 \mu\text{sec}$.

On the other hand, when the driver is projected against the target, the driver must be thick enough to maintain adequate stiffness. The shots of Table IV in Section 3.b (1) were made this way. Aluminum drivers 3.2 mm thick produce pulses with the peak pressure phase initially about $1 \mu\text{sec}$ long, during which the pressure will decay somewhat by attenuation effects in the target material. In the absence of thermal effects, the first release wave from the free surface of the driver would not drop the pressure at the impact interface to zero, since the particle motion would still be forward. However, expansion of trapped air (the vacuum being imperfect) and of shock-heated target material can quickly reverse the particle motion, producing a tension tail on the pulse which will soon release the driver and may ultimately break

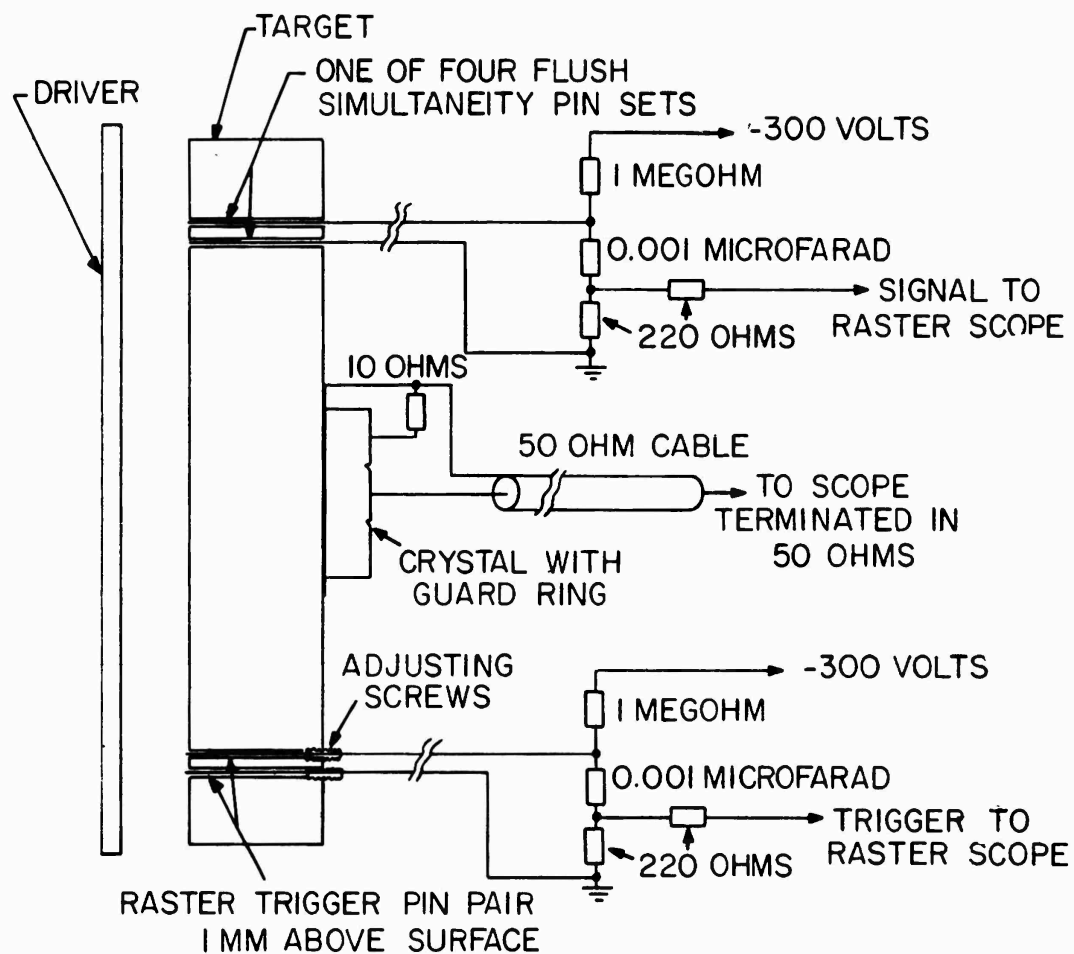


Fig. 5. Electrical Circuit for Quartz Crystal Transducer On Target. Triggering Accomplished Either By (1) Flush Pins (2) Simultaneity Flush Pins (3) Raster Trigger Pin, or (4) Internal Trigger

the bond between the target and the gauge crystal. As the pulse propagates through the target material, the release wave following the shock is expected to catch up to the shock front, shortening and ultimately eliminating the plateau behind the shock front.

Calculations (made for other programs at GE and elsewhere) of pulse profiles by the Richtmyer-von Neumann method, using smooth equations of state and no preferential absorption of various Fourier components, show sloping fronts, spikes behind the fronts, and oscillations. These effects are artifacts of the finite difference method, produced by the effective loss of high frequency components. Actual loss of the high-frequency components in a real target and in the recording apparatus will have similar effects. Preferential actual loss in the target of components elsewhere in the spectra will cause other deformation of the record, as will spurious losses or additions in the circuitry. These points will be discussed further in the coverage of experimental results.

Richtmyer-von Neumann calculations, using nonlinear fits to experimental data on equation of state, also show that the actual pressure change on reflection at an increase of motional impedance is greater than that computed by the acoustic approximation applied in Section 3.b(2); so that experimental observations of pressures higher than those expected on the basis of simple acoustic theory are not necessarily the result of experimental error. On the other hand, as simultaneity and boundary effects in the gauge crystal will lead to an indicated pressure lower than was actually developed in the center of the target.

Adequate simultaneity with short pulses was usually obtained when using stationary drivers and moving targets. The targets listed in Table V of Section 3.b (1) were thick enough to resist distortion during acceleration. Other sources of irregularity in the records include reflections at impedance mismatches such as the connection between the cable and the electrodes, fluctuations in the oscilloscope circuitry, frictional electricity ("static") produced by motions in the gun, including motions of the residual air, thermoelectric effects from shock heating of the residual air, variable contact resistances and contact electrification effects (especially in the moving contacts required for the stationary driver method). All these sources of irregularity were guarded against, but apparently not with uniform success, as is shown in the results to be discussed presently. Air trapped in the cement between the gauge and the target can be heated above 10^4 °K by reverberating shocks. Since the Thomson effect is quadratic, the resulting signal could be over 1v, in the sense of an apparent increase of pressure. The other effects mentioned could presumably also produce spurious signals comparable to the true signal; although this has not been experimentally proven in the present case.

(2) Circuitry and geometry

The circuitry for using the quartz crystals is fairly simple. The only complication is the requirement for the use of a guard ring technique and for reasonably good impedance matching to insure fast response and to minimize reflections or other spurious signals. Figure 5 shows the circuitry actually used. Figure 6 is a photograph of a crystal mounted on a target.

The pressure was obtained by use of the formula

$$P = \frac{IT}{AK} \quad , \quad (4)$$

where P = pressure in kilobars, I = current in amperes, A = active electrode area in cm^2 , K = piezoelectric constant ($= 2.04 \times 10^{-8}$ coulombs/ cm^2/kb between 0 and 10 kb), and T = shock transit time through the quartz.

The crystals used in this program were x-cut synthetic alpha quartz crystals obtained from the Valpey Crystal Corporation. They measure 1.250 inches in diameter and 0.375 inches thick. They are coated on both faces with vapor-deposited electrodes consisting of chromium 10 to 15 microinches thick followed by codeposited chromium and silver approximately 25 microinches thick, plus approximately 30 microinches of silver.

The guard-ring arrangement is achieved by machining a narrow groove one half inch in diameter through the positive electrode on the crystal. This is done on a lathe, using a pointed steel cutting tool. The center section of the electrode is connected through a coaxial cable to an oscilloscope shunted with a 50 ohm resistor to minimize reflections and possible spurious signals. To minimize the potential difference across the guard ring (the magnitude of which would otherwise be several kv), the inner electrode area multiplied by 50 ohms should equal the outer electrode area multiplied by the appropriate value of shunting resistance. This works out to require a 10 ohm resistor from the outer electrode to ground. For convenience, this resistor is normally placed right beside the crystal. Oscillations in this loop should be too fast to register.

It should be noted that in the crystal experiments performed by GE, the crystal signals were fed into Tektronix oscilloscopes having frequency response good to 15 megacycles. While higher performance oscilloscopes might have been desirable, there is no evidence that they would have appreciably improved the results obtained. A calibrating high frequency pulser was used before several of the tests, to insure that the measuring circuits would record the correct values.

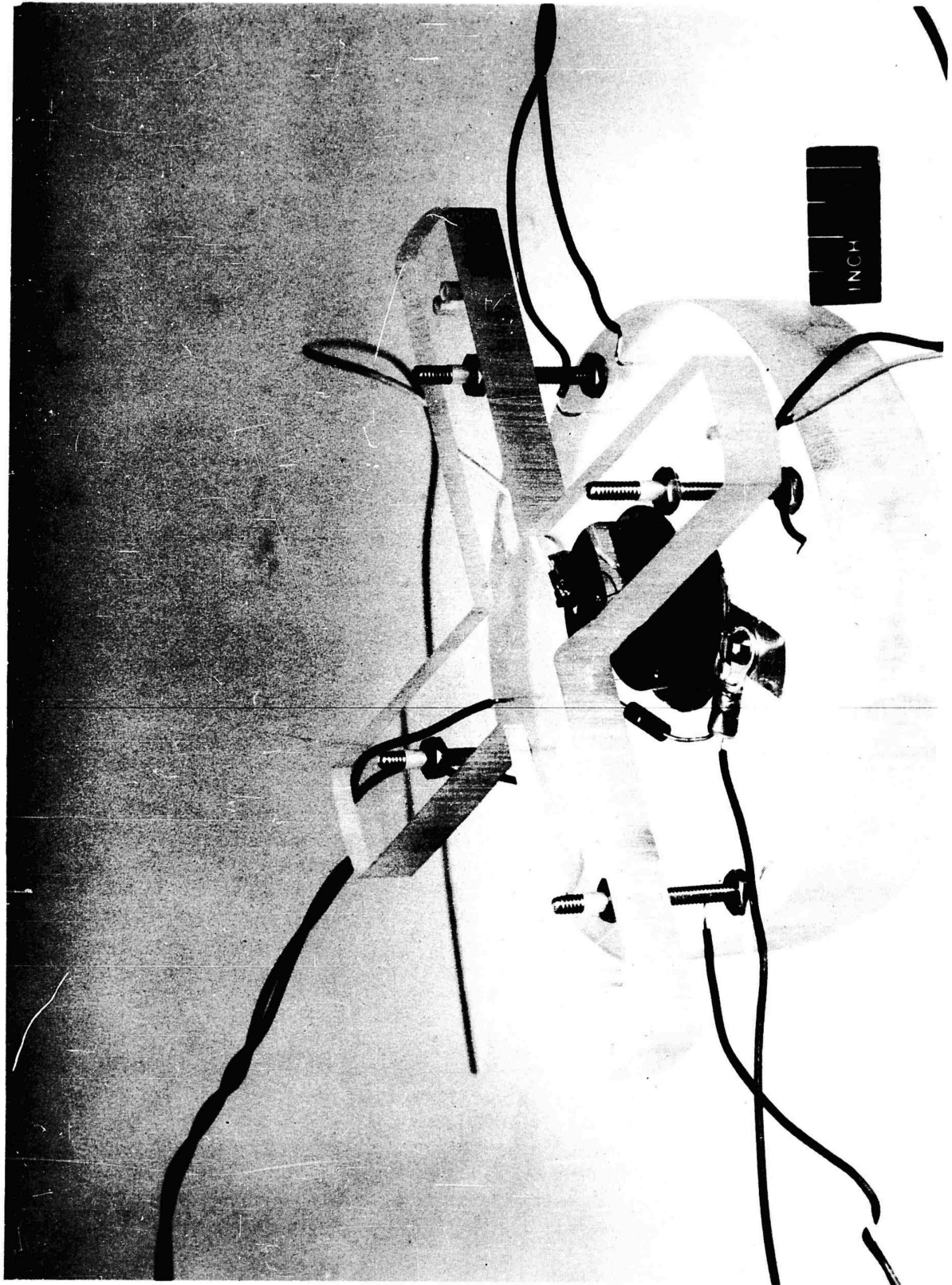


Figure 6. Photograph of Quartz Crystal Transducer Mounted on Target

Although the size of the targets used would have allowed the placement of four crystals on a single target, it was decided to restrict the multiple crystal shots to two and three crystals each and employ a fourth crystal only if the initial results so warranted and if the fourth crystal did not introduce edge effects. As will be discussed later, the pulse profiles obtained indicated only slight changes in shape in the pulse between the 1/4 inch and the 1/2 inch stations.

The geometry for the three-crystal shot is shown in Figure 7. Two of the crystals were recessed, at 1/2 inch and 1/4 inch from the impact surface, and the third crystal was attached to the rear surface. A calculation by Lt. R. Brightman and Lt. F. Vajda of AFWL indicated that edge effects from one crystal to another should have been negligible. The results corroborated this conclusion.

For the production of pulses of duration shorter than the transit time through the quartz crystal ($1.66 \mu\text{sec}$), it was necessary to use very thin drivers. For such impacts, it was necessary to mount the target on the sabot and keep the driver stationary. This required a means for providing electrical contacts to the moving crystal. Pointed rods were mounted adjacent to the driver and through the Lucite holder as shown in Figure 8. Crystal leads were soldered to foil-covered balsa blocks attached to the sabot adjacent to the target. Just prior to impact the rods would penetrate the foil-covered balsa and complete the circuit. As stated in the last entry in Table I, contact closure ordinarily was smooth and introduced no distortion into the circuit.

c. Light Transmission Technique

A difficulty with the quartz crystal technique, or any method which utilizes a transducer attached to the rear surface of a target, is that only the pulse crossing that interface is measured. For maximum information, it is necessary to see the compression pulse within the material, and it is even more desirable to see the reflected tensile pulse in the region where fracture is initiated. As a first approximation, one might assume that the tensile pulse is the inverted reflection of the compressive pulse. However, this approximation is inadequate for two reasons: (1) we generally do not have sufficient knowledge about the equation of state in tension of the target material, and (2) the integrated particle motion of the rear surface during reflection must be taken into account. Neither of these is a simple problem to treat.

In principle, at least, it is possible to measure strain in a material during shock propagation by using light transmission techniques. Such methods do not perturb the system being studied, and the tensile pulse, if observed, should be the true pulse responsible for fracture in a target with a free rear surface.

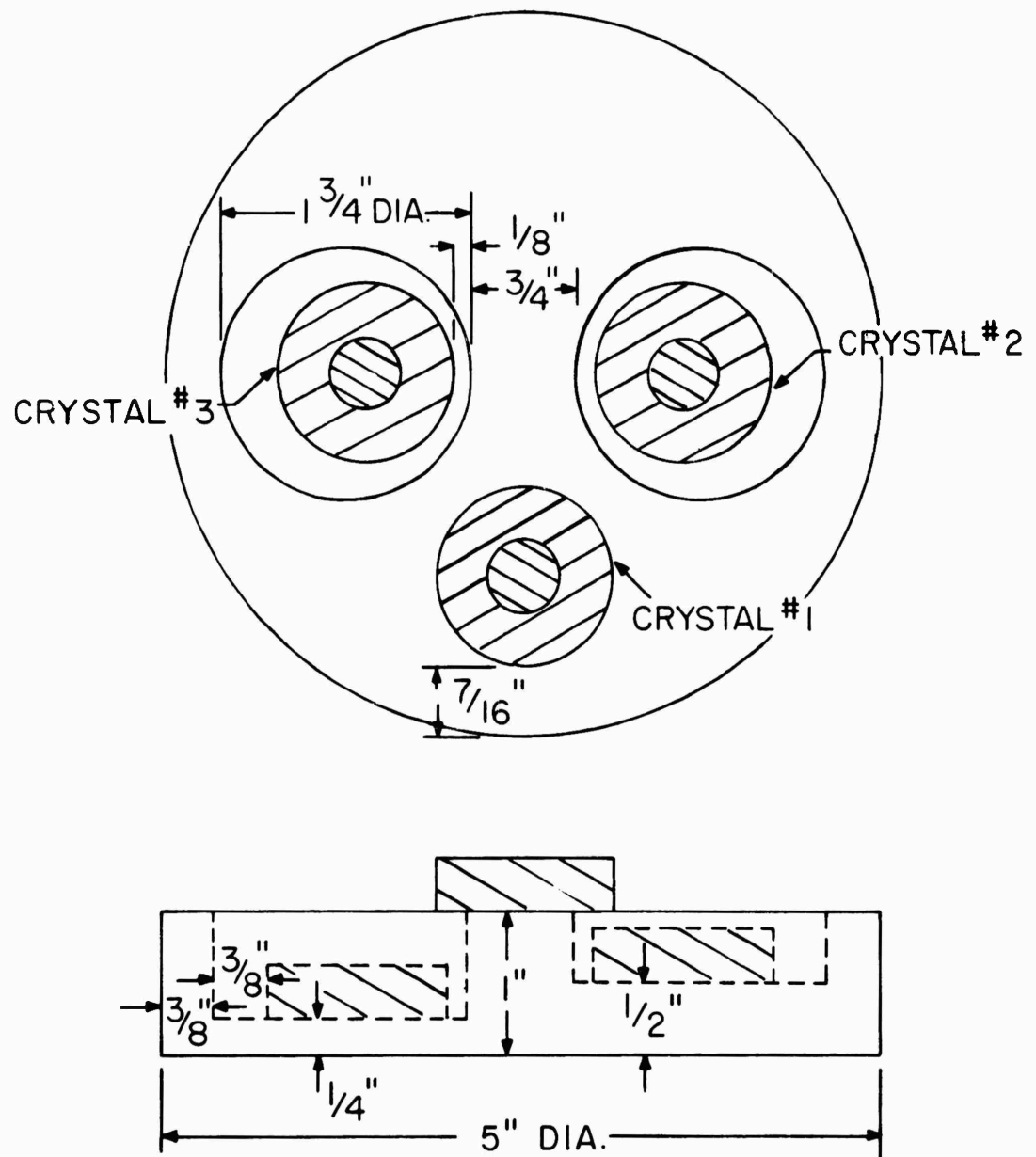


Fig. 7. Geometry For Target With Three Quartz Crystal Transducers

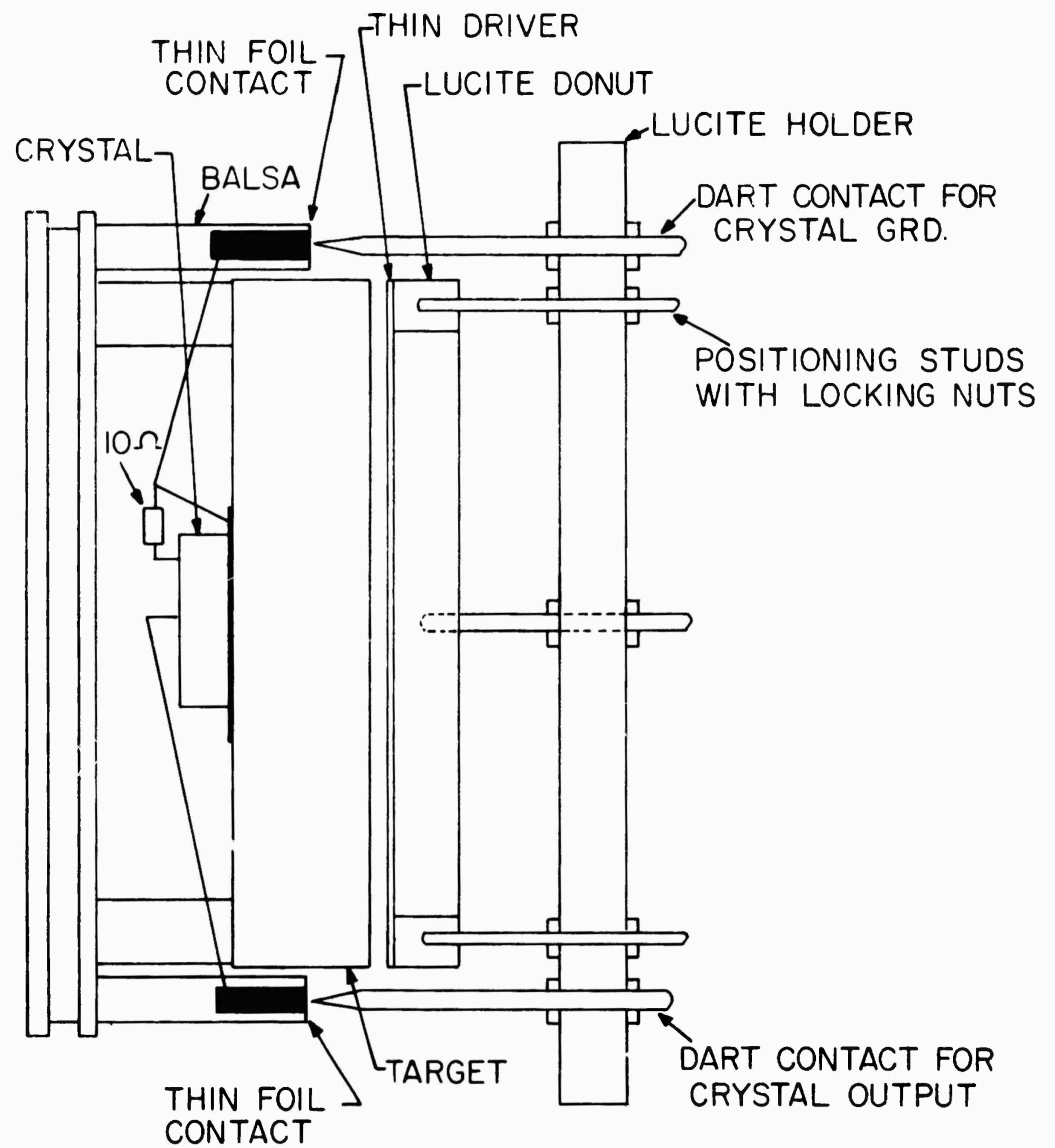


Fig. 8. Target and Crystal Assembly Prior To Moving Target Impact

One technique for making such a measurement depends on the change in optical density of a target when the material is compressed or pulled in tension. Calculations from the equation of state for the more rigid resin, BC323, indicate that this material compresses about 0.7% under a pressure pulse of 0.5 kb. The rubbery material, BC326, is also readily compressible. Since the coefficient of light absorption in a sample is proportional to the density change, and occurs in an exponent as a multiplier of the thickness, it should be possible to measure such a change in the region of spall threshold, providing the detector can resolve light changes in the order of a few percent.

Attempts were made to supplement the pulse measurements using quartz crystal transducers with pulse measurements using the light transmission technique. The procedure consisted of shining a narrow beam of light through the target perpendicular to the direction of the wave front and observing the change in light output with a photomultiplier. Under ideal conditions, the photomultiplier circuit output would then give a density change versus time record for a small region within the target.

A number of impacts were made using various experimental arrangements and including homogeneous as well as multiply cast and composite targets. The latter included targets which had the central portions dyed so that maximum light absorption would occur in those portions and possible edge effects would be eliminated. In some targets, the central portion (2.5 cm wide) consisted of the natural amber-colored resin, with 9 cm of clear Lucite attached to both sides. The 2.5 cm sample was opaque on all sides except for narrow vertical slits located at half the target thickness. A diagram of this target is shown in Figure 9, and a photograph of the complete arrangement at the firing test site is shown in Figure 10. As will be discussed later, initial results indicated that light transmission was increased on impact. Subsequent shots therefore included some in which no light source was used and in which the impact surface was "blacked out" to prevent observation of light from compressed residual gas in the gun barrel or from other extraneous sources.

d. Framing Camera Technique

There can be little doubt that one of the best guides to an understanding of almost any phenomenon is to be able to see it happen. Shock-induced fractures almost certainly would be a great deal easier to understand if we could see them forming. The problem, however, is that they form far too fast for the eye to follow. High speed cameras have been developed for use in just such situations and seemingly should be very useful in studying shock induced fracture. Unfortunately, there are some rather severe problems.

A serious effort was made to observe fracture formation using a Barr and Stroud high speed framing camera capable of taking pictures at a rate up

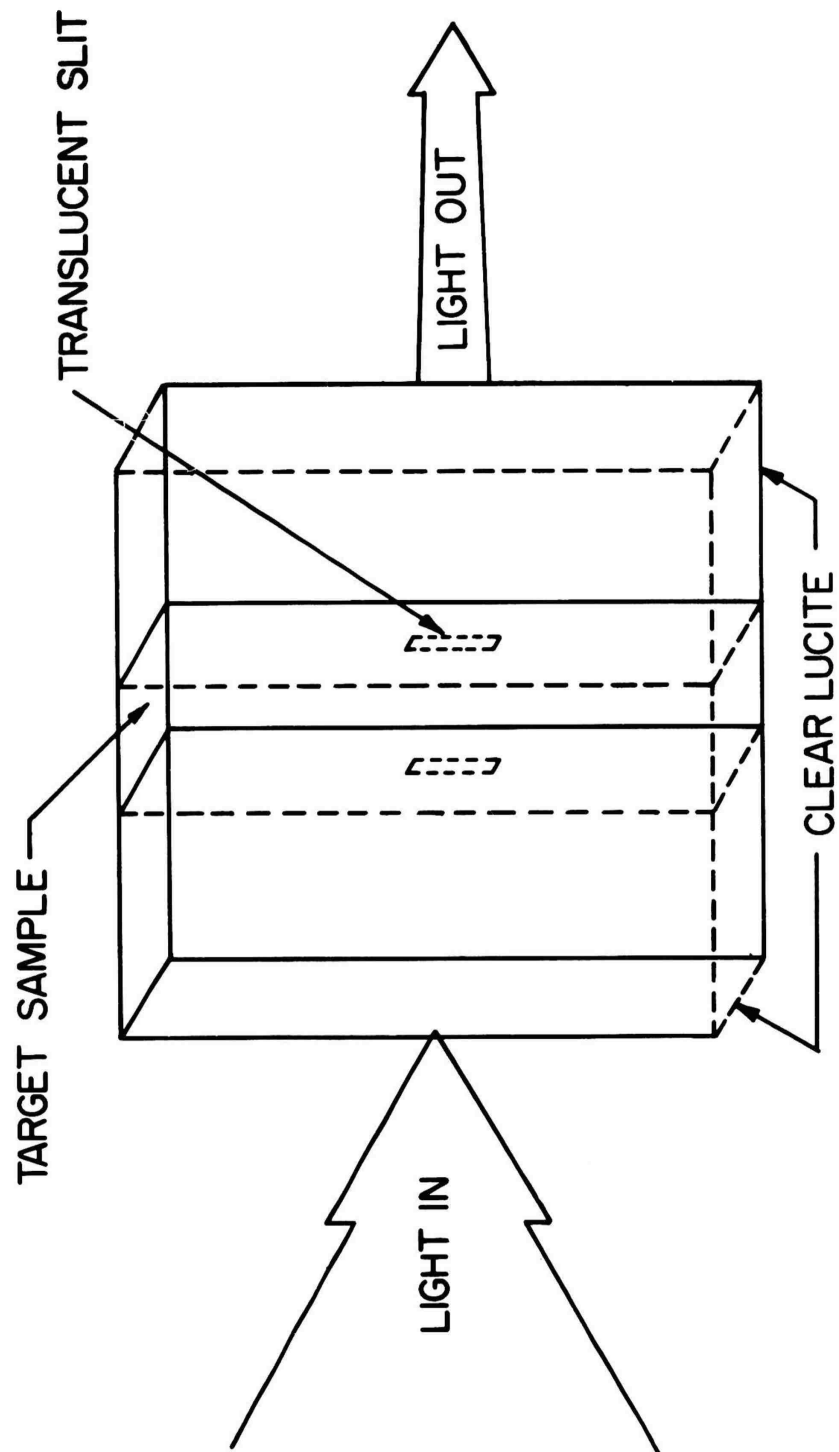


Figure 9. Composite Target for Light Transmission Study

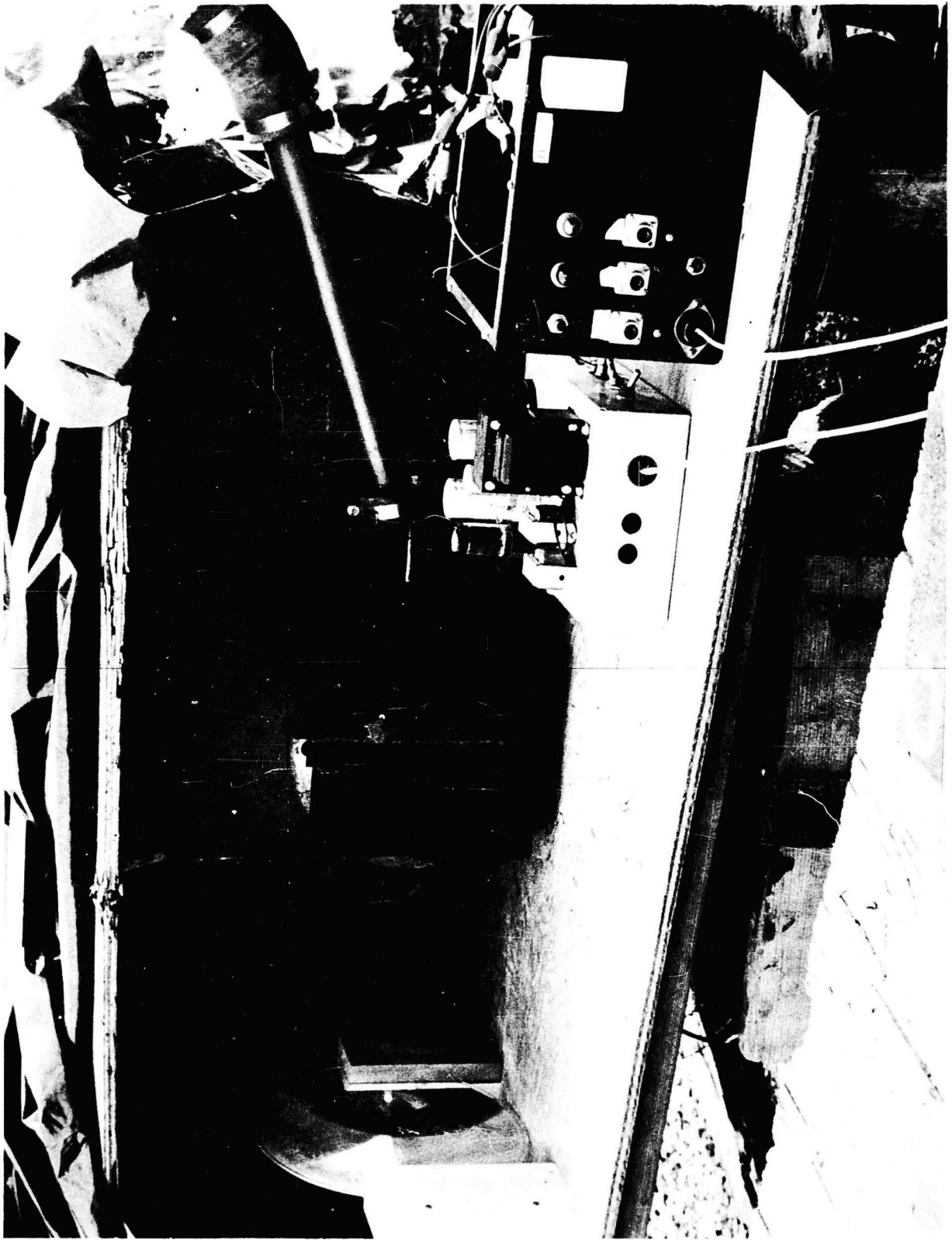


Figure 10. Photoelectric Pulse Measuring Apparatus

to 4×10^6 frames per second. The Barr and Stroud camera is a rotating mirror type camera in which the mirror is in a position to record on the film only approximately one-third of the time. Thus, for optimum performance the camera should be synchronized so that the event to be photographed starts just as the mirror comes into position to start exposing the film. At 4×10^6 frames per second, the total viewing time of the camera is approximately 14.5 microseconds; so synchronization to less than a microsecond is necessary. With a compressed-air gun, which requires something in the order of 125 milliseconds from firing until impact on the target, it is extremely difficult to achieve microsecond synchronization.

Since precise synchronization appeared to be beyond immediate reach, it was decided to do the next best thing and simply trigger the light source at the proper time so that the camera would see the fracture formation if the mirror happened to be in the proper position. This can be done fairly readily by the use of barrel probe pins. It was recognized that the chance of getting good data under these conditions was something less than one in three, but these were considered acceptable odds. Unfortunately, no photographic records were obtained even with the camera running at approximately 25% of its maximum speed. This was because of inability to get sufficient light through the sample to expose the film adequately.

The light source used for these experiments was an Ascor xenon flash unit that is about as bright as anything commercially available for such an application. Consideration was given to other more powerful light sources, such as an argon flash bomb, but nothing appeared really suitable. The flash bomb seemed to show the most promise, but the explosive environment associated with its use was considered excessively severe for the other equipment involved. Because of the lighting difficulty and the synchronization problem, it was decided not to do any further work with this technique.

It should be noted that the use of high-speed photography to study the fracture process is not considered wholly infeasible. It does appear infeasible when one is using a six-inch diameter compressed-air gun to produce the fracture; since this requires looking through approximately eight inches of target. It is possible that one might achieve some success by the use of laser techniques for illumination, but this would require a level of effort that was considered beyond the scope of the contract. It is believed that by the use of smaller samples, which would require a smaller gun, or by the use of some other technique for shocking the sample, and with a sufficient development effort on a suitable light source, the problems could be worked out and successful pictures obtained.

3. DISCUSSION OF RESULTS

a. Equations of State

At any instant, the state of a homogeneous sample of material is defined by describing simultaneously the density (or its reciprocal the specific volume), the stress (which may be a function of direction) and the various contributions to the energy content. It is usually adequate to indicate the energy by specifying the temperature.

In some cases, it is understood that the stress, temperature and density start at definite values and are changed by a specific process. Then it is adequate to specify the state after this process in terms of the new stress and the new density or specific volume, relative to these parameters before the process. The change of temperature will be implicitly controlled by the process and the material properties. Thus the Hugoniot equation of state relates the pressure and specific volume behind a macroscopically 1-dimensional shock front to the original values, without explicitly mentioning the temperature.

Stress is often symbolized by P , where $P > 0$ refers to compressive stress and $P < 0$ refers to tensile stress. When anisotropy must be considered, it is preferable to use σ to denote the stress tensor and σ_{ij} to denote a component of the stress tensor. Dimensionally,

$$P = E/V \quad (5)$$

where V is volume, and the energy content E is that part of the specific energy which affects the stress during the process being considered. The changes resulting from the process satisfy

$$\Delta P = \Delta E/V \quad (6a)$$

or

$$\Delta P = \Delta E/V_0, \quad (6b)$$

where subscript zero refers to initial conditions and a quantity without subscript is the value after the process, and where the correct ΔE is used in either case. Use of the final volume V , as in (6a), corresponds to the Lagrangian approach of considering the history of a given mass of material. Use of the initial volume V_0 , as in (6b), corresponds to the Eulerian approach of considering events in a fixed volume. Thus, for a compressional ΔP , the ΔE in (6b) is greater than the ΔE in (6a); because the additional mass pressed into V_0 introduces additional contained energy. It is also dimensionally accurate to state formally

$$\Delta P = \xi \Delta E / \Delta V, \quad (7)$$

where ξ is defined so as to make (7) a true equation. Since, as noted, stress is usually a function of direction as well as of position within the sample, a second rank tensor field more completely describes σ . Then ξ must also be a tensor. Elimination of $\Delta P/\Delta E$ between (5) and (6b) shows that

$$\xi = \Delta V/V_0, \quad (8)$$

where ξ is proportional to the trace of the strain tensor. When the compression is macroscopically 1-dimensional and ξ is referred to its principal axes, ξ is proportional to the resulting non-zero term on the principal diagonal (Ref. 9).

In the current program, broad flat samples were used, pulsed by compression waves. The first fractures were caused by reflection of the waves from free surfaces approximately parallel to the wavefront, before release waves from the lateral boundaries reached the region of failure. This macroscopically 1-dimensional motion is all that is considered in most of this report; so that the P which is discussed is usually the component of the stress tensor normal to the nominal wavefront. The average macroscopic particle motion, at speed u behind the front of an evenly supported shock causes a displacement $u\Delta t$ during the interval Δt . Meanwhile, the wave front, moving at an effective average speed U , has progressed the distance $U\Delta t$. Since no macroscopic lateral motion is allowed, the change ΔV in specific volume, relative to the initial V_0 , is thus u/U . This same fraction expresses the change in density relative to the final density ($\Delta\rho/\rho$), since the particle motion behind the shock has crowded the particles closer together into a smaller final volume. Denote the fraction by ξ :

$$u/U = \xi. \quad (9)$$

A plot showing the locus of the values of P reached by shocking to various ξ 's is a form of Hugoniot, where ξ comes from particle speed and wave speed by way of (9). These same two speeds also determine the stress. The amount of material swept over in Δt by a unit area of the wave front is $\rho_0 U\Delta t$. Since it is brought to the speed u , its momentum per unit area is $\rho_0 Uu\Delta t$, which is also the pressure-time product $P\Delta t$. The time interval cancels, leaving

$$P = \rho_0 Uu, \quad (10)$$

by conservation of momentum. Then knowledge of experimentally determined pairs of u and U leads to a plot of P against ξ , by (9) and (10), and allows us to tag the plot of U vs u with corresponding values of P and ξ .

Numerous analytical expressions have been suggested to fit the $P - \xi$ data. For instance, the plot of U against u can be extrapolated to give the

(finite) U_0 which corresponds to $u = 0$, i.e. to $P = 0$. Formally, for other wave speeds,

$$U = U_0 + \lambda u. \quad (11)$$

Eliminate u by (9), obtaining $P = \rho_0 U^2 \xi$, thus $U^2 = P/\rho_0 \xi$ from (10). Then (11) gives $U = U_0 + \lambda \xi U$, or $U = U_0/(1 - \lambda \xi)$, whence $U^2 = U_0^2/(1 - \lambda \xi)^2$. Elimination of U^2 gives

$$P = \frac{\rho_0 U_0^2 \xi}{(1 - \lambda \xi)^2}, \quad (12)$$

which yields the correct P for arbitrary ξ , provided correct values are introduced for ρ_0 and for U_0 , and provided the slope λ is read correctly, for the selected compression ξ , from the curve of U vs. u . Since the first use of Equation (12) was probably by R. G. McQueen and others, it will be called the McQueen equation.

As a stress-strain relation, Equation (12) has more than a formal utility, since λ turns out to be nearly constant over a wide range of P , allowing ready interpolation and even extrapolations to pressures much higher than those covered by a given set of experimental data. Strict constancy of λ would lead to an absurdity; when $\xi = 1/\lambda$, $P = \infty$, and when $\xi > 1/\lambda$, P will decrease from infinity for further increase of ξ . Clearly λ must drift toward unity as ξ approaches unity, so that ξ remains less than $1/\lambda$. Also, at low stress levels, λ cannot remain constant and single-valued; since extrapolated U_0 values are found to lie mostly in the range of 0.7 to 0.85 times the 1-dimensional sound speed c_0 , and since, throughout the elastic range, $\lambda = 0$. In the elastic range, (12) must be replaced by $P = \rho_0 c_0^2 \xi$, which is equivalent to Equation (10).

As mentioned, Equations (5), (6), (8) and (12) are by no means the only possible forms for analytical expression of the equation of state. Power series, exponentials, and other forms have been suggested, some with parts of the energy explicit, others with all the energy implicit.

Refs. 3 and 4, together with their bibliographies, give the background for most of the preceding discussion, in algebraically equivalent and more detailed form. The authors of Ref. 4 feel that substantial constancy of λ should extend to very high pressures, and suggest that there is a systematic error in the high-pressure Russian work (Ref. 5) which they quote. There may indeed be some such systematic error, but part of the drift of λ toward unity is very possibly real, and in line with our discussion above. Curvature of the U vs u plot for the rather compressible metal tin is noted by the authors of Ref. 5, and is marked in the plot for aluminum in Ref. 3. The much more compressible plastics studied in the work here reported can be expected to show still greater curvature of the U vs u plot.

In determination of the equation of state of plastics, difficulties arise from the experimental methods. By some writers, the particle velocity u is ordinarily taken to be half the measured free-surface speed resulting from relief of the shock pressure. However, compactibility of the material (flow of molecular segments into voids, whether on the molecular scale or a larger scale) tends to reduce the free-surface speed at first, but to produce heating which may ultimately raise the free surface speed to more than double the actual particle speed in the shock before it reaches the free surface. In the present work, u has been taken as $u_{fs}/2$ wherever the errors so introduced appear to be less than errors from other causes.

Dispersion arises from several sources, so that there is a spread of particle velocity and wave velocity within the pulse. For work on equation of state, it would be desirable to produce and measure pulses which are true shocks for which the stress is constant behind the front, and for which shock speed and particle speed are constant during the period of data acquisition. This requires absence of dissipation and also requires equal velocity for all Fourier components and for all wavefront vectors. In practice, lateral motion of molecular segments into regions of low density will produce preferential dissipation at higher frequencies, but not necessarily as a monotonic function of frequency (Ref. 6, especially pp. 131-135 and pertinent earlier discussion, Ref. 7, pp. 279-284 and elsewhere). The result will be an irregular rise of the pulse, at first rapid, then slower, rather than an instantaneous rise to a constant stress.

A wave front of this type, sweeping through the sample, will be headed by an elastic precursor in which the wave speed is high but the particle speed is much lower. As the stress rises, various relaxation mechanisms will be excited. The accompanying slippages increase the particle speed but temporarily reduce the effective stiffness and therefore the wave speed; so that further pressure rises are propagated more slowly (so-called plastic wave) than the elastic precursor. In metals and other crystalline material of relatively high rigidity, the spectrum of such relaxations is narrow, and the complete wave system for pressures somewhat above the dynamic elastic limit is an elastic precursor followed by a plastic wave of which the front rises almost discontinuously. In plastics, the relaxation spectrum tends to be broader, making the plastic wave front more gradual. Wave fronts for BC323 and BC326, however, still are steeper than those found earlier for the more rubbery material polyethylene (Ref. 8).

For specimens of not too great a thickness, the front is kept quite steep, despite the dissipation of the high frequency components, by the tendency of the high frequency components to propagate faster in compression than the low frequencies. The opposite tendency occurs in tension, thus causing the wave front reflected from a free surface to lose its slope more rapidly. Complexities, such as those resulting from time-integrated precursor motion and from the plastic wave running into material already relieved

by reflection of the elastic precursor, can be partially avoided in the equation of state work by starting to record the free-surface motion only after it has progressed a few hundred microns. The effects of these complexities, however, may not have vanished completely in the studies of spallation by unsupported pulses. The latter are those which have a duration less than the transit time across the sample. Further, they are probably incompletely allowed for in the current comparison of glassy and rubbery resins. Accordingly, in our data analyses, the points on the U vs u plot and on the Hugoniot graph must be provided with rather wide limits of probable error. In fact, the error limits are so wide that, in the previous report (Ref. 1), no attempt was made to describe the equation of state for BC326. More data, with somewhat better precision, are displayed in Tables II and III, and are plotted in Figures 11 and 12 for U vs. u . These include additional values for BC323 and tentative plots of the McQueen equation in Figure 13. Plots of IIP vs impact speed for BC326 and for aluminum against BC326 are given in Figures 14 and 15, respectively.

The data are not good enough to establish definite U vs u curves. Straight lines which minimize the weighted squares of the normal deviations are shown (solid lines), as well as possible lines expressive of possible curved fits (dashed). On the basis of work with related materials, it is to be expected that work at higher pressure would show a rapid drift toward much lower values of λ (the slope of the U - u plot). Thus the plots should not be extrapolated very far.

As mentioned in the preceding report, the chief reason for the large scatter in these results is the slope of the plastic wave front, which is far from vertical in these materials. Almost equally distressing is the large effect of even slight asynchronicity when the particle speed is only a few percent of the wave speed.

For consistency with the pin switch results, velocities which were derived from quartz crystal results were computed from the first arrival of the pulse. Actually, shock pressure is related to momentum transport, as is shown by the derivation of Equation (10). Also, pin measurements may overlook a precursor of small pressure. Therefore it might be preferable to use an average of the wave front speed, weighted to correspond to the effective average particle speed; since particle motion transports momentum. Such an adjustment would reduce the reported U values, thereby reducing the reported pressures and increasing the reported compressions, especially for BC326. However, since we do not yet know how to make the adjustment, the data are here reported in terms of first arrivals.

Pulse speed was measured in BC326 for samples of various length/diameter ratios, and pulse pressures of a few bars, so as to have near-sonic conditions. Extrapolation to $l/d = 0$ (plate conditions),

TABLE II. DATA FOR EQUATION OF STATE OF BC323 RESIN

Density, $\rho_o = 1.24$ gm/cc

Serial	$\frac{u_{fs}}{2}$ (mm/ μ sec)	$u^{(1)}$ (mm/ μ sec)	u_o (mm/ μ sec)	U (mm/ μ sec)	$Z_{Al} 10^{-5}$ (cgs $\times 10^{-5}$)	Z_{BC323} (cgs $\times 10^{-5}$)	IIP ⁽³⁾ kb (cgs $\times 10^{-9}$)	$\frac{v}{U}$
905	.050 \pm .002	.062 \pm .005	.072	2.36 \pm .13	17.7	2.93 \pm .16	1.80 \pm .04 ⁽²⁾	.0262
907	.075 \pm .005	.123 \pm .015	.145	2.53 \pm .17	17.7	3.14 \pm .20	3.86 \pm .20 ⁽²⁾	.0487
1061		.109 \pm .012	.130	2.69 \pm .16	17.7	3.34 \pm .20	3.64 \pm .18	.0406
1068		.107 \pm .005	.123	2.15 \pm .05	17.7	2.66 \pm .06	2.85 \pm .07	.0498
1072		.109 \pm .005	.127	2.30 \pm .05	17.7	2.85 \pm .06	3.12 \pm .06	.0475
1080		.101 \pm .006	.122	2.95 \pm .10	17.7	3.65 \pm .12	3.69 \pm .10	.0343
1148		.017 \pm .001	.034	2.25 \pm .10	*2.80 \pm .11	2.80 \pm .11	0.48 \pm .02	.0076
1153		.010 \pm .001	.019	1.90 \pm .10	*2.35 \pm .13	2.35 \pm .13	0.22 \pm .01	.0053
1157		.026 \pm .002	.053	1.82 \pm .07	*2.25 \pm .09	2.25 \pm .09	0.60 \pm .02	.0143
1157		.027 \pm .003	.053	2.65 \pm .15	*3.28 \pm .18	3.28 \pm .18	0.87 \pm .05	.0102
1160		.050 \pm .003	.054	1.45 \pm .05	17.7	1.80 \pm .06	0.89 \pm .03	.0345
1178		.111 \pm .010	.127	2.10 \pm .10	17.7	2.60 \pm .12	2.87 \pm .12	.0530
1193		.032 \pm .003	.037	2.12 \pm .12	17.7	2.63 \pm .15	0.85 \pm .04	.0151
1193		.033 \pm .005	.037	1.85 \pm .15	17.7	2.29 \pm .18	0.76 \pm .05	.0178
1207		.083 \pm .005	.095	2.08 \pm .07	17.7	2.58 \pm .08	2.14 \pm .07	.0399

(1) Calculated from IIP.

(2) $P = \frac{\rho_o U u_{fs}}{2}$ gave lower values, 1.5 kb for 905, 2.4 for 907.(3) $IIP = \frac{u_o A_{Al} Z_{BC323}}{Z_{Al} + Z_{BC323}}$

* BC323 impacted against BC323

In shots 1157, 1193 two crystals instrumented, speeds over separate paths.

Shots 905, 907 used charged pins as detectors, while all other shots used quartz crystals.

TABLE III. DATA FOR EQUATION OF STATE FOR BC326 RESIN

DENSITY, $\rho_o = 1.27 \text{ gm/cc}$

Serial	$\frac{u_{fs}}{2}$ (mm/ μ sec)	$u^{(1)}$ (mm/ μ sec)	u_o (mm/ μ sec)	U (mm/ μ sec)	Z_{Al} (cgsx10 ⁻⁵)	Z_{BC323} (cgsx10 ⁻⁵)	IIP ⁽³⁾ kb (cgsx10 ⁻⁹)	$\frac{u}{U}$
918	.034 \pm .001	.079 \pm .015	.095	3.00 \pm .30	17.7	3.80 \pm .38	2.96 \pm .25(2)	.0271
922	.093 \pm .015	.120 \pm .024	.149	3.61 \pm .43	17.7	4.58 \pm .53	5.40 \pm .50(2)	.0344
923	.073 \pm .024	.136 \pm .021	.170	3.64 \pm .31	17.7	4.62 \pm .31	6.24 \pm .41(2)	.0373
1192		.038 \pm .004	.044	2.34 \pm .13	17.7	2.97 \pm .16	1.12 \pm .05	.0162
1195		.033 \pm .002	.037	1.97 \pm .05	17.7	2.50 \pm .06	.82 \pm .02	.0167

(1) Calculated from IIP.

(2) $P = \frac{\rho_o U u_{fs}}{2}$ gave 1.3 kb for 918, 4.4 for 922, 3.5 for 923.

(3) $IIP = \frac{u_o Z_{Al} Z_{BC326}}{Z_{Al} + Z_{BC326}}$.

Shots 918, 922, 923 used charged pin detectors and shots 1192, 1195 used quartz crystals.

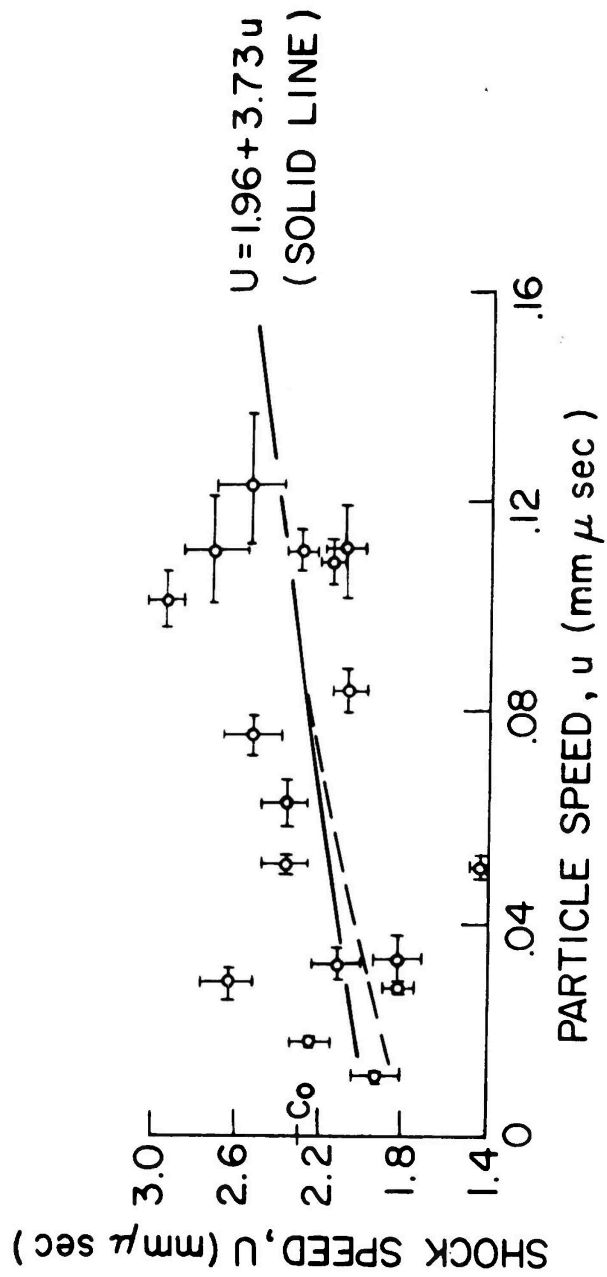


Figure 11. Equation of State Data for BC323 Resin

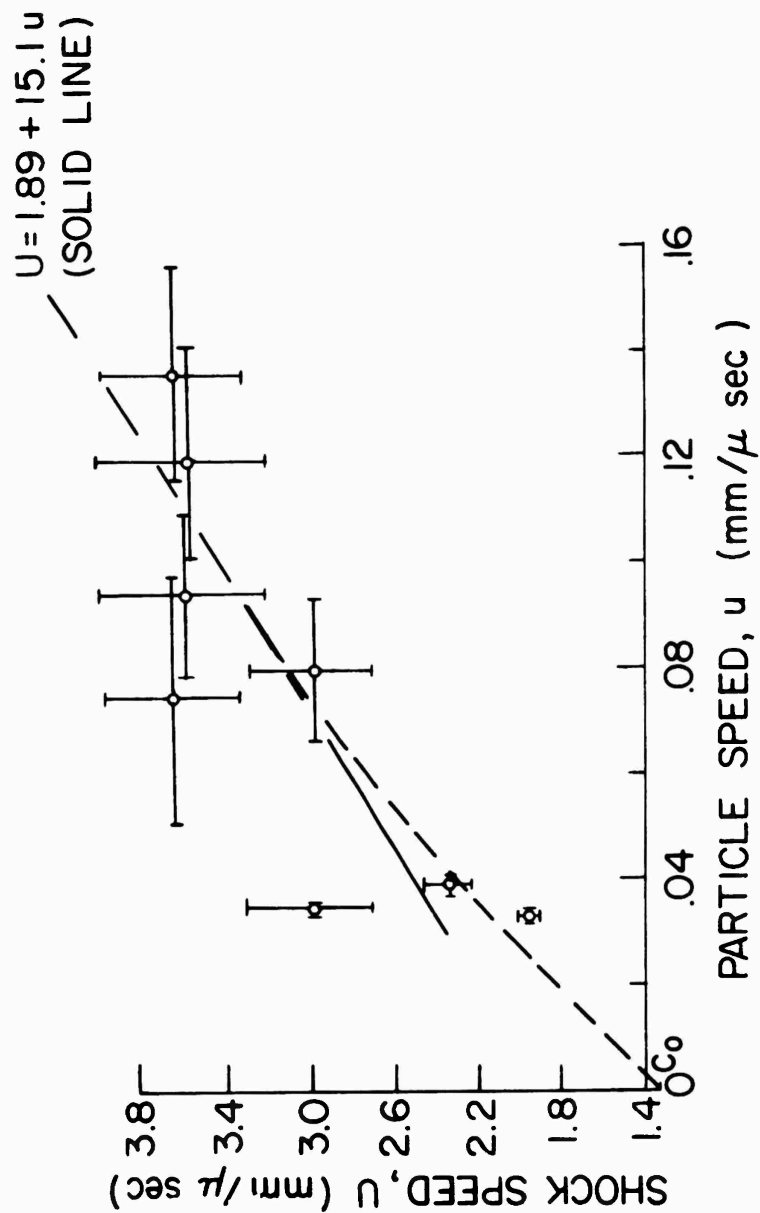


Fig. 12. Equation of State Data for BC326 Resin

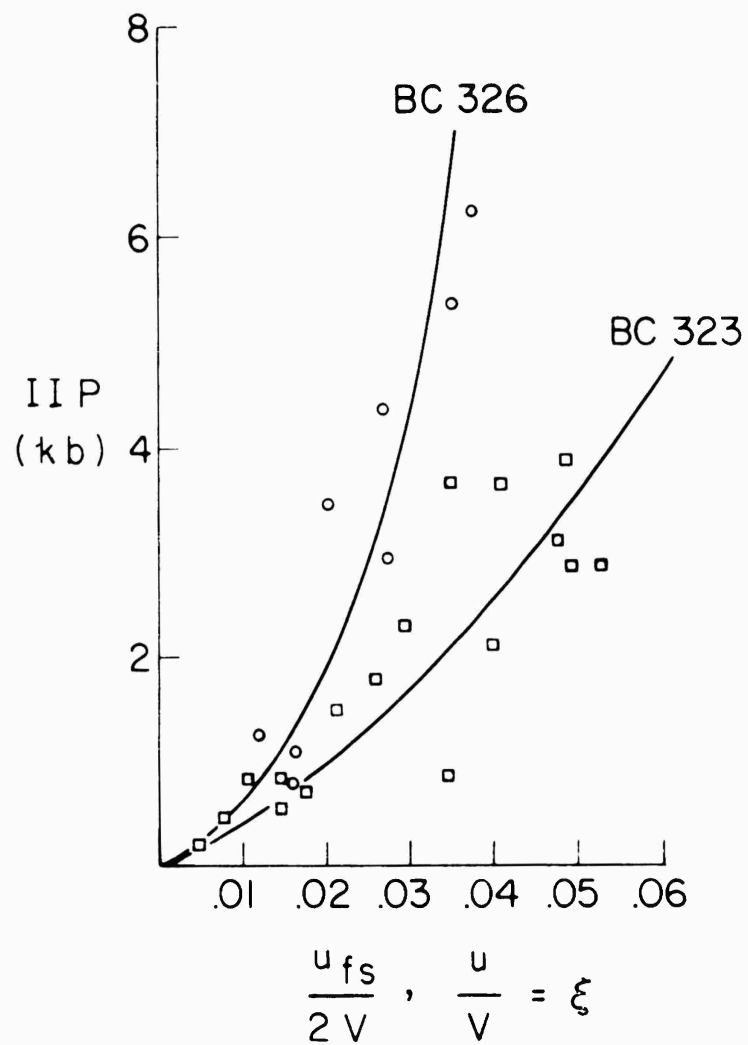


Fig. 13. Comparison of Equations of State For BC323 and BC326 Resins

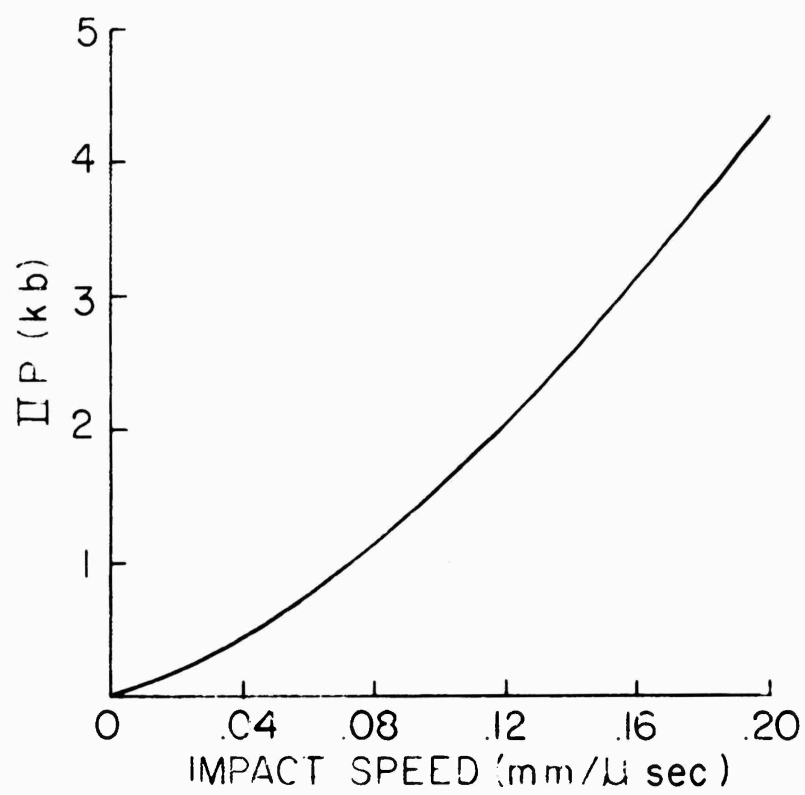


Fig. 14. BC326 Against BC326

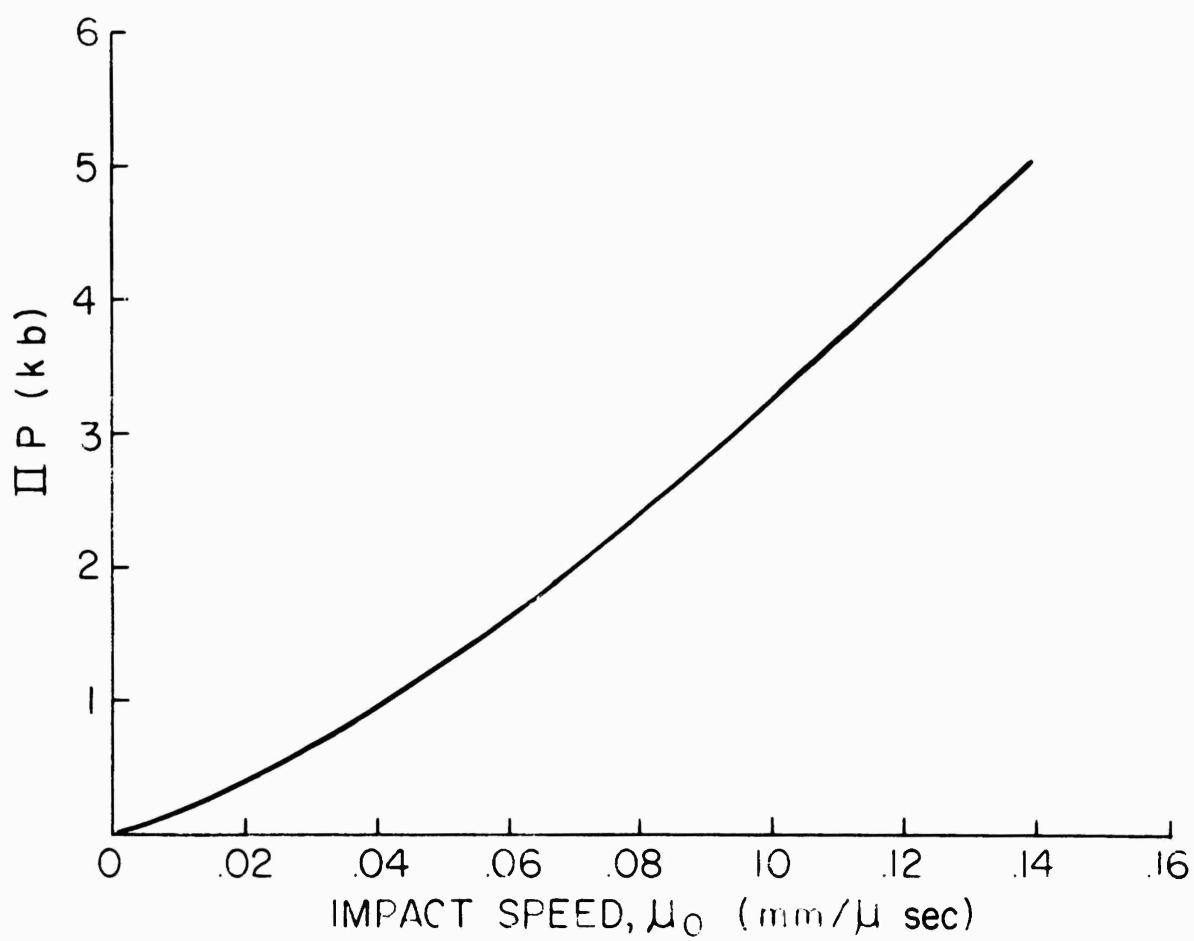


Fig. 15. Aluminum Against BC326

$$c = \left\{ \left[Y/\rho \right] \left[(1 - \nu) / (1 + \nu) (1 - 2\nu) \right] \right\}^{1/2} , \quad (13)$$

gave $c = 1.35 \text{ mm}/\mu\text{sec}$. Extrapolation to $d/l = 0$ (rod conditions),

$$c = \left\{ Y/\rho \right\}^{1/2} , \quad (14)$$

gave $c = 0.86 \text{ mm}/\mu\text{sec}$, where c is the sound speed. These values correspond to a Young's modulus Y for impulsive loading of about 9.4 kb (140,000 psi), with a dynamic Poisson's ratio ν of 0.41. Quasi-static measurements would be made difficult by creep, but these figures are in line with measurements on related materials. The Young's modulus for BC323 is about 4 times greater, and the dynamic Poisson's ratio is about 0.36.

b. Pulse Profiles in Rigid Resin

(1) General description

On the average, an oscilloscope trace begins with a rapidly damped noise pulse produced by the switching transient, continues with a straight sweep while the pulse is approaching the gauge crystal, then bends slightly up or down as the pulse (if tilted) enters the edge of the crystal. This slope of the record should not occur for perfectly simultaneous impact. Traveling lateral expansion of the quartz cylinder introduces a tension wave which (because of the directions of the particle motions) can induce slight negative voltages at the electrodes. Apparently, these occasionally override the positive contributions. For a perfect wave front, this preliminary deflection should not exist, and in fact it is often undetectable on the actual traces.

As the wave front reaches the central part of the gauge face, there is usually a precursor enduring for about a twentieth of the time of transit through the target, and rising typically to a stress of roughly 0.1 kb, where it blends into the main rise.

The records of the peak and the decay are not very reproducible. The sources of fluctuation discussed at the end of Section 2b(1) are probably largely responsible for the observed irregularities. Since the latter are so unreproducible, the responsibility probably does not lie with effects such as oscillatory coupling between electrical and mechanical relaxations, nor with preferential absorption of Fourier components in the intermediate frequency range.

Table IV contains data for impacts in which the target, with crystal (or crystals) attached, was stationary and the driver was moving prior to impact. Photographs of representative oscilloscope traces are shown in Figure 16, 17 and 18. Diagrams of initial portions of some of the more usable traces for which BC323 was the target are shown in Figures 19, 20 and 21.

Several of the records warrant individual mention. In shot 1068, (Figure 19) the rise of the record is close to that expected for a sum of the slope due to the measured asimultaneity plus an intrinsic slope lasting $0.3 \mu \text{ sec}$. This is followed by a slow decay such as has been indicated in the past by Hopkinson momentum traps applied to similar plastics (Ref. 8), with slight ripples which may be entirely instrumental, but may be partly caused by the preferential attenuation of certain Fourier components of intermediate frequency. This cannot be a large effect in BC323. (See Ref. 9, especially Chapter 10, and also Ref. 6).

There is, for shot 1068, practically no indication of an elastic-plastic transition. On all the other usable records, such as those from shots 1061 and 1080, there is a precursor, but always much slighter than those demonstrated for metals (Ref. 2). In BC323, the precursors all curved, indicating that the relaxations between the elastic condition and plastic yielding occur by various mechanisms and over a whole spectrum of stress levels rather than at a single well-defined stress level (Ref. 6). The plastic wave is usually well-formed when the pressure reaches 0.5 to 0.7 kb, but plastic yielding may start at pressures less than 0.1 kb.

When U (wave speed) is plotted against u (particle speed) for metals, the extrapolation to $u = 0$ gives a finite U_0 decidedly less than the dilatational sound speed c_0 . For BC323 also there appears to be a moderate difference between U_0 and c_0 , as is seen in Figure 11. This leads us to expect a precursor.

When a straight line sweeps at uniform speed across a disk, the swept-over area increases sinusoidally. If the pulse rise were instantaneous, except for the effect of asimultaneity, the record of a tilted wave should rise as a symmetrically inflected, slightly distorted $\sin^2 t$ curve; since the crystal face is circular. So-called maximum asimultaneity in Tables IV and V was measured across about 78 mm; so that the $\sin^2 t$ half-cycle across a 32 mm crystal should take about 0.4 the tabulated times. Actually, the measured rises tend to be less (especially when the precursors are subtracted) and by no means of $\sin^2 t$ form. Thus the wave of shot 1193, with "maximum asimultaneity" of $1.2 \mu \text{ sec}$ at impact, would have required at least $0.5 \mu \text{ sec}$ to sweep over the crystal face (See Figure 21). Any blurring produced during transit through the target would increase this period. There were two target steps, one of 6.4 mm, the other of 12.7 mm, each with a crystal. The thin step showed a precursor of about $0.06 \mu \text{ sec}$, followed by a slightly irregular rise of about $0.33 \mu \text{ sec}$, steeper than average at start and end (opposite to $\sin^2 t$ behavior), then an irregular decay of about the expected type. Subtract $0.04 \mu \text{ sec}$ for instrumental effects. The remaining $0.35 \mu \text{ sec}$ for precursor and plastic wave rise time must be divided between actual slope and the effect of wavefront tilt. The latter would be at least $0.2 \mu \text{ sec}$ for this case, leaving not more than $0.15 \mu \text{ sec}$ for actual precursor and slope, the latter therefore being less than $0.09 \mu \text{ sec}$.

Over the thicker part of the stepped target, the precursor length increased rather less than twofold, and the total rise required approximately $0.45 \mu\text{sec}$, corrected for cable charging and oscilloscope rise time. Allowing for the doubled length of the precursor and for $0.2 \mu\text{sec}$ of wave tilt, we find that the rise time of the plastic wave, at about $0.13 \mu\text{sec}$, had increased less than twofold. The steepest wave fronts found after transit of 25 mm of BC323 allow less than twice this rise time for the plastic front; so that apparently development of slope proceeds at its highest rate at first.

The quartz crystal method has been more successful in exploring details of shock fronts than in exploring shock decay phenomena. Table IV lists experiments in which the driver moved and therefore had to be so thick that not much decay could be expected during the first transit. Table V lists experiments using thin stationary drivers. Three of these gave records, all more or less vitiated by spurious signals possibly arising from imperfect contacts and thermoelectric effects. Shot 1207, indeed, gave a record distinctly resembling that expected for a pulse produced by a thin overmatching driver (driver of motional impedance higher than that of the target). See Figures 22 and 23 for details on this trace. Ideally, this pulse should have begun with a rise occupying 0.3 to 0.4 μsec , dotted by slight cable reflections at 0.1 μsec intervals (10 m cable, or 20 m for transit and return, at a pulse speed which is about $2/3$ the speed of light). Then there should have been a peak, followed by a sharp decrease of slope to a decaying near-plateau lasting less than the $1/2 \mu\text{sec}$ duration of a reverberation in the aluminum alloy driver. That is, the release wave should have caught or overrun the wave front. Then there should be a stepwise decay, with blurred sloping $1/2 \mu\text{sec}$ steps, representing further reverberation, terminating in a sharp decay: the elastic-plastic transition should cause an approach to a tension shock near the end of the pulse tail. As stated, the actual record somewhat resembles this expectation, but the differences cannot be analyzed and interpreted without checks to confirm their reality and statistical significance.

(2) Comparison of quartz data with equation of state

While the results of the pulse profile measurements using quartz crystals would appear to have yielded only limited information, those results were useful for serving as a check on the consistency of the data for aluminum impacts on BC323. The method of calculation will be described by means of an example, using shot 1068. That shot is chosen because the rise time was fairly short ($\sim 0.2 \mu\text{sec}$) and the top of the pulse profile, after the initial peak, was reasonably flat. A diagram of that pulse is repeated in Figure 24 and the pertinent data are presented in Table IV.

The IIP for the impact (3.2kb) was obtained from the calibration curve shown in Figure 25. That curve was determined from Equation (15), in which u_0 is the sabot velocity, ρ is initial density, U is the shock velocity, and the subscripts t and d refer to target and driver respectively.

$$P = u_o \left[\frac{\rho_d U_d \rho_t U_t}{\rho_d U_d + \rho_t U_t} \right] \quad (15)$$

By plotting the Hugoniot pressure-particle speed curve for aluminum (taken from Ref. 10) and drawing in the curve for the reflected rarefaction wave, one can determine from the impact speed and the IIP the particle speed, u , in the BC323 target at impact (See Figure 26). This procedure is valid; since at zero pressure the particle speed in the aluminum must be equivalent to the impact speed. Furthermore, if the reflected Hugoniot is drawn from this point on the abscissa, the pressure in the target must lie on this curve; since the pressure and particle velocity must be continuous across the driver-target interface at impact. The motional impedance curve for the BC323 derived on this basis is shown as a dotted line in Figure 26. From the Hugoniot relation expressing the conservation of momentum,

$$P = \rho_o U u, \quad (16)$$

the slope of the dotted line gives $\rho_o U$ for the target. This value is 29.4×10^4 dyne-sec/cc and is the motional impedance of the BC323.

To obtain the corresponding pressure in the quartz crystal from the pressure in the target, Equation 17 must be used:

$$P_q = P_t \left[\frac{2(\rho_o U)_q}{(\rho_o U)_q + (\rho_o U)_t} \right], \quad (17)$$

Taking the density of quartz as 2.6 and the shock velocity in quartz as 5.7 mm/ μ sec (essentially independent of pressure in the elastic region) the result is:

$$P_q = 3.2 (1.67) = 5.3 \text{ kb.}$$

Comparison of this calculated value with the observed values (Table IV) of 5.8 kb at the peak and 4.75 kb for the flat portion indicates fair agreement. If one assumes the flat top of the measured pulse to be the more accurate of the two recorded, the difference is in the right direction; since if the amplitude of the pulse changes during propagation, it would be expected to decrease rather than increase. As noted in Section 2. b (1), numerical integrations indicate reflected pressures somewhat higher than those computed by Equation (17), which was used for the sake of simplicity.

In a similar manner, the anticipated quartz pressures for other impacts were calculated. The results are given in Table IV, where the piezo-

electric pressures are labeled "observed" and compared to the pressures "calculated" from impact speeds, shock speeds, and the Hugoniot curves.

c. Pulse Profiles in Rubbery Resins

The plot of U vs u for BC326 (Figure 12) indicates little difference between the extrapolated U_0 and c_0 , the 1-dimensional dilatational sound speed. Also, the pulse histories show no definite precursors (Figs. 27 and 28). Rather, the relaxation spectrum seems to extend from the very start of the trace. The fronts develop a more gradual slope than do the fronts of similar pulses introduced into BC323. The details of pulse decay are seen even less well for BC326 than for BC323, but for shot 1253, which used a 1 mm BC326 driver against a 13 mm BC326 target, there appeared to be a tendency for the release wave to steepen (Figure 29). The pulse seemed to be back to zero before the end of the first transit, and appeared to decay from an expected input pressure of about a kilobar to less than 1/3 of this in the 13 mm of travel through the target. Two traces of this pulse were obtained, one based on internal triggering and one on raster pin triggering, but neither trace was considered sufficiently reliable for plotting a quantitative diagram.

d. Light Transmission Results

The experiments with the light transmission technique were not successful in providing supplementary information on pulse profiles. Signals were obtained which indicated changing light transmission through the targets, but the changes were not consistent with the expected changes in target density; nor did they appear only when the pulses were expected to pass the slits.

In the initial attempts, using homogeneous targets, there was some difficulty in sensing the light (from a mercury arc lamp) after passage through 8 inches of resin. This size of target was necessary; since it needed to be outside the gun and the most convenient method for holding it was by pressure against the evacuated dump tank. Also, edge effects in a large homogeneous target could become troublesome. Therefore, composite targets as described in Section 2.c were used for most of the early impacts, with the resin of interest comprising the central portion of a Lucite-Century Resin-Lucite composite. The first impact (No. 1046) for which data are given in Table VI utilized such a composite. In that experiment, the photomultiplier gave a negative signal (corresponding to increased light transmission) rather than the expected positive signal. Since this was contrary to the type of signal resulting from an increase in target density during passage of the compression pulse, considerable efforts were devoted in subsequent impacts to eliminating possible spurious light sources. In target 1075, for example, all outside surfaces were painted black, as were the two inside interfaces. Only a thin vertical slit was retained for passage of light. The blackening was primarily to eliminate light from compressed residual gas in the gun. Again, however, the signal went negative (~ 0.2 v) on impact and did not turn positive until

after 8.5 μ sec (Figure 30a). Prior to impact, a positive deflection of 0.1 volt corresponded to turning off the mercury arc light source; hence it is obvious that the deflections observed after impact must have resulted from additional sources, either optical (piezoluminescent) or electrical in nature.

A similar result was obtained for target 1077, except that the signal did not go negative until after 10 μ sec and then remained negative only a short time before turning positive (Figure 30b). Again, 0.1 volt corresponded to on-off light conditions.

The next several impacts recorded in Table VI were performed using no light source. In impact 1081, the oscilloscopes failed to record. In 1091, on the other hand, the photomultiplier gave a negative signal which eventually went off scale (Figure 30c). This result showed definitely that a signal was being generated from a source other than the mercury arc lamp.

In experiment 1093, a rotating mirror camera was used as a detector in addition to the photomultiplier. Light appeared on the film, but the pattern could not be interpreted meaningfully. Similar results were obtained in experiments 1101 and 1112, the latter utilizing an image converter camera as detector.

An Ascor xenon light source was then used, and the cathode follower in the photomultiplier circuit was removed. With this arrangement, light transmission through the full 8 inches of resin could be measured easily. Unfortunately, some of the signals in the next few impacts were lost, presumably because of premature and/or faulty triggering of the oscilloscope. In the last impact in this series (1214) a negative signal was obtained with momentary positive components early in the trace (on-off light conditions in this experiment corresponded to a signal of about 60 volts (Figure 30d). One of these components could have corresponded to the compression pulse, but the long time base of the one record obtained did not afford sufficient resolution to establish this fact definitely.

The difficulties encountered with the light transmission technique were too numerous to resolve within the time scope of this program. The results indicated that some of the possible reasons for a negative photomultiplier signal, such as stray electrical pick-up, were ultimately eliminated. Other reasons were advanced, including luminescence produced by relative particle motion within the target. While such effects during comminution are well known, e.g., triboluminescence, it is felt that the evidence in these experiments was insufficient to justify definite conclusions based on these considerations.

TABLE IV. MEASUREMENTS OF PULSE PROFILES WITH QUARTZ CRYSTAL TRANSDUCER. TARGET STATIONARY

Serial Number	Target (Stationary)	Driver (Moving)	Gas Pressure (Microns)	Sabot Velocity (mm/ μ sec)	Initial Impact Pressure (kb)	Pressure in Quartz (kb) Obs. Calc.	Maximum Asimultaneity (μ sec)	Tilt Angle	Pulse Width in Quartz (μ sec)	Remarks
1011	3/4" Al	1/8" Al	200	0.16	12	12.6	not measured		1.8	Foam alignment # Trigger Mode A. k value of 2.16×10^{-8} used for this impact only
1061	1"BC323	1/8" Al	600	0.13	3.4	4.3	5.7	not measured	2.6	Foam alignment. Trigger Mode A.
1068	1"BC323	1/8" Al	175	0.123	3.2	4.75 flat 5.8 max.	5.3	not measured	1.65	Foam alignment. Trigger Mode A. Pulse rise $\approx 0.2 \mu$ sec.
1072	1"BC323	1/8" Al	600	0.127	3.3	5.2	5.5	not measured	1.8	Foam alignment. Trigger Mode A. Evidence of a precursor.
1080	1"BC323	1/8" Al	100	0.122	3.2	4.0	5.3,	not measured	2	Foam alignment. Trigger Mode A.
1092	1"BC323	1/8" Al	200	0.127	3.3	6.4 max	5.5	26	1.9	Foam alignment Trigger Mode A. Ringing signal could not be interpreted.
1181	1"BC323	1/8" Al	50	0.042	1.0	2.5 max	1.7	0.8	1'10"	Rod alignment (no foam). Trigger Mode B. Rise time $< 0.2 \mu$ sec.
1148	1"BC323	1/4"BC323	35	not measured .034 expected	---	---	---	0.4	2'10"	Rod alignment. Trigger Mode B. Crystal recorded very late, showing start of rise.



1092	1"BC323	1/8" Al	200	0.127	3.3	6.4 max	5.5	26	22'42"	1.9	Foam alignment Trigger Mode A. Ringing signal could not be interpreted.
1181	1"BC323	1/8" Al	50	0.042	1.0	2.5 max	1.7	0.8	1'10"	2.5	Rod alignment (no foam). Trigger Mode B. Rise time < 0.2 μ sec.
1148	1"BC323	1/4"BC323	35	not measured .034 expected	---	---	---	0.4	2'10"	.5	Rod alignment. Trigger Mode B. Crystal recorded very late, showing start of rise.
1153	1"BC323	1/4"BC323	10	0.019	0.2	0.33 knee 0.47 max	0.33	1.7	1'28"	2	Rod alignment. Trigger Mode B. Rise time low.
1157	1/2"BC323 1"	1/4"BC323	50	0.053	0.7	0.13 knee 0.94 max	---	1.5	3'38"	1	Rod alignment. Trigger Mode B. Both crystals on same target-one recessed 1/2"
1160	1/4"BC323 1/2"BC323 1"	1/8" Al	20	0.555	1.2	lost 1.46 max off scale	---	not measured	---	1.9	Rod alignment. Trigger Mode B. All 3 crystals on same target. 1/4" signal was lost. 1/2" and 1" crystals in good agreement.
1193	1/4"BC323 1/2"BC323	1/8" Al	50	0.037	0.9	1.5 max 1.0 flat	1.5	1.2	2'2"	2	Rod alignment. Trigger Mode B. Rise time ~0.3 μ sec Two signals in good agreement.
1178	1/4"BC323	3/8" Al	200	0.127	3.3	6.3	5.5	0.8	4'40"	2	Rod alignment. Trigger Mode B. RG-8 cable used. Only record was on guard ring. 1 μ sec rise.
1187	1"BC326	1/8" Al	50	0.036	---	---	---	13.9	17'20"	---	No signal
1192	1"BC326	1/8" Al	75	0.044	---	1.04 flat	---	2.4	3'38"	2	Rod alignment. Trigger Mode B. Cyclic signal. Very gradual rise.
1195	1"BC326	3/8" Al	25	0.037	---	0.7 max	---	1.4	1'46"	2	Rod alignment. Trigger Mode B. Very similar to #1102. 1 μ sec rise. 3 cycles recorded.

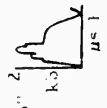
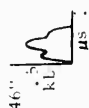
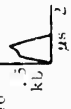
* Trigger Mode A - Flush pins

Trigger Mode B - Flush simultaneity pins

Trigger Mode C - Projecting raster trigger pin



TABLE V. MEASUREMENTS OF PULSE PROFILES WITH QUARTZ CRYSTAL TRANSDUCER. TARGET MOUNTED ON SABOT.

Serial Number	Target (Moving)	Driver (Stationary)	Gas Pressure (Microns)	Sabot Velocity (mm/ μ sec)	Initial Impact Pressure (kb)	Pressure in Quartz (kb)		Maximum Asimultaneity μ sec	Tilt Angle	Remarks
						Obs.	Calc.			
1207	1"BC323	1/16" Al	5	0.048	1.0	1.04-1.8	1.67	0.5	1'6"	Trigger mode B ⁽¹⁾ . Rapid drop in signal at 6.5 μ sec corresponds to 1st pass through driver. 
1228	1/2"BC323	0.039" BC323	5	0.059	0.8	--	--	1.3	--	Trigger mode B. No signal.
1242	1/2"BC323	0.039" BC323	75	0.05	0.7	--	--	1.7	2'56"	Trigger mode B. No signal.
1251	1/4"BC323	0.039" BC323	20	0.042	0.6	--	--	19.2	36'48"	Trigger mode B. No signal.
1252	1/4"BC323	1/16" Al	20	Not measured 0.05 expected	--	--	--	3.3	4'32"	Trigger mode B & C. Hashy cyclic signal, part of which resembled #1207.
1253	1/2"BC326	0.039" BC326	5	Not measured 0.06 expected	--	--	--	6.0	13'46"	Trigger mode C & D. Possible signal later than expected. 
1271	1"BC323	1/16" Al	5	0.035	0.85	0.25 flat 0.58 peak	1.42	1.1	1'46"	Trigger mode B. Pulse peak much lower than #1207. 

(1) Driver was aligned by rod and lock nut method.

Triggering modes were:

- A) Flush pins
- B) Flush simultaneity pins
- C) Projecting raster trigger pin.
- D) Internal trigger.

TABLE VI
Impacts for Studying Light Transmission Through Targets

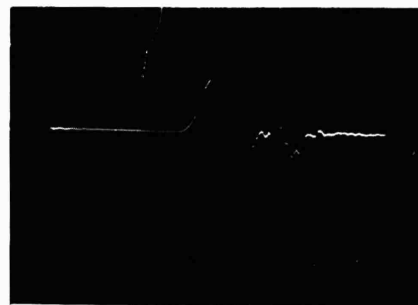
Serial Number	Target	Driver	Sabot Velocity (mm/ μ sec)	Initial Impact Pressure (kb)	Gas Pressure (microns)	Remarks
1046	1"x3"x8" BC323 with 1"x2 1/2" x 8" Lucite on either side	1/8" Al	0.114	3.0	100	Face of Target Clear. 2.5 μ sec after impact, photomultiplier indicated marked increase in light rather than dimming. Pulse width with 1/8" Al driver \approx 1 μ sec.
1050	1"x1"x8" 123 with 1"x3 1/2"x8" Lucite on either side	1/8" Al	0.124	3.4	75	No signal
1075	1"x1"x8" 123 with 1"x3 1/2"x8" Lucite on either side. All surfaces inside and out painted black except for 1"x1/16" vertical slit.	3/8" Al	0.122	3.3	300	Signal went negative (corresponding to increased light) on impact and lasted 8.5 μ sec. Signal then went positive. Pulse width with 3/8" Al driver \approx 3 μ sec.
1077	Same as 1075	3/8" Al	0.127	3.6	5	Signal indicated slight increase in light (for 3.3 μ sec) at end of 10 μ sec. Dimming then occurred.
1081	1"x1"x8" black BC323 with 1"x3 1/2"x8" Lucite on either side. 1mm x 1" slit. Surfaces black	3/8" Al	0.124	3.2	400	No light source used. No signal was obtained.
1091	1"x1"x8" black BC323 with 1"x1"x3 1/2" Lucite on either side. 1mm x 1" slit. Surfaces black	3/8" Al	0.123	3.2	500	No light source used. Photomultiplier showed light on impact, increasing stepwise until it went off scale.
1093	1"x8"x8" BC323 Black surfaces except for thin slit	3/8" AL	0.130	3.4	50	No light source used. Instrumented by photomultiplier and rotating mirror camera. Photomultiplier showed 3 damped oscillations of 5 Mc. Light appeared on camera film. Neither record could be analyzed.
1101	1"x8"x8" BC323 with Al foil on impact surface	3/8" Al	0.133	3.5	100	Same instrumentation as #1093. Photomultiplier had distorted damped oscillation of 1 Mc lasting 10 μ sec. Light appeared on film in rotating mirror camera but was not meaningful.
1112	1"x8"x8" BC323 Black face	3/8" Al	0.122	3.1	100	Instrumentation was by an image converter camera giving 0.2 μ sec exposures 2 μ sec apart. Light appeared but could not be analyzed.

TABLE VI (Cont'd)
Impacts for Studying Light Transmission Through Targets

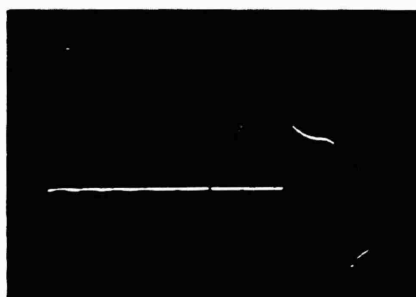
Serial Number	Target	Driver	Sabot Velocity (mm/ μ sec)	Initial Impact Pressure (kb)	Gas Pressure (microns)	Remarks
1174	1"x8"x8" BC323 Painted except for slit	3/8"AL	0.127	3.3	175	Ascor xenon light source - 8 millisec duration. Shot at night for low background. Output directly off photomultiplier. On & off condition gave 60 v signal. No record obtained on impact.
1175	1"x8"x8" BC323 composite (dyed-clear-dyed)	3/8"Al	0.122	3.1	50	Ascor light-daytime-bypassed follower. Short time base signal lost.
1188	1"x8"x8" BC323 (dyed) with 1"x8"x 1 mm clear slit	3/8"Al	0.122	3.1	25	Short time base signal lost. Changing light on long time base scope probably due to target breakup.
1189	1"x8"x8" BC323 (dyed) with 1"x8"x 1 mm clear slit	3/8"Al	0.122	3.1	25	Same as #1188, but initial dimming lasted about 250 microseconds.
1200	1"x8"x8" BC323 (dyed) with 1"x8"x 1 mm clear slit	3/8"Al	0.105	2.7	5	2nd photomultiplier was used to record possible electrical pickup - none occurred. Ascor light on 1st photomultiplier triggered too late to give a useful signal.
1204	1"x8"x8" BC326 (dyed) with 1/4" x 1"x8" clear slit	3/8"Al	0.124	4.3	5	Signal was lost.
1214	1"x8"x8" BC326 dyed	3/8"Al	0.129	4.5	5	Signal went negative, indicating increased light. Subsequent dimming occurred but trace could not be interpreted. Short time base signal was lost.



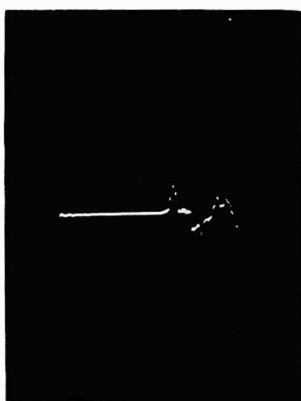
1011 - Al Target



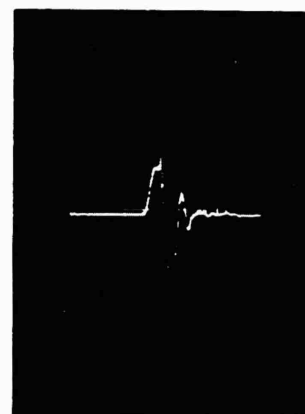
1061 - BC-323 Target



1068 - BC-323 Target

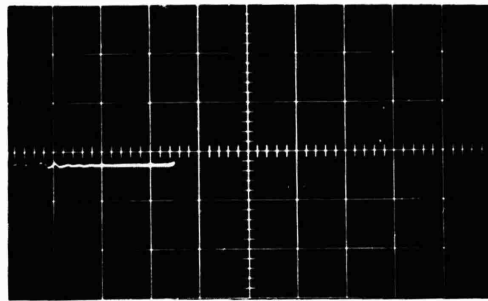


1072 - BC-323 Target

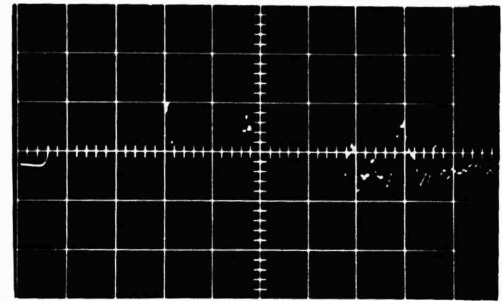


1080 - BC-323 Target

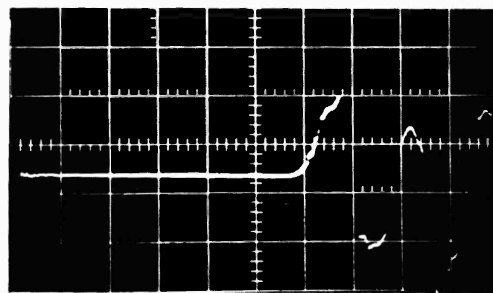
Figure 16. Quartz Crystal Oscilloscope Traces



1157 - BC323 Target
1/2" Thickness



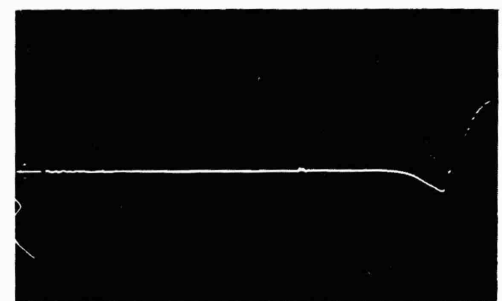
1157 - BC323 Target
1" Thickness



1153 - BC323 Target
1" Thickness

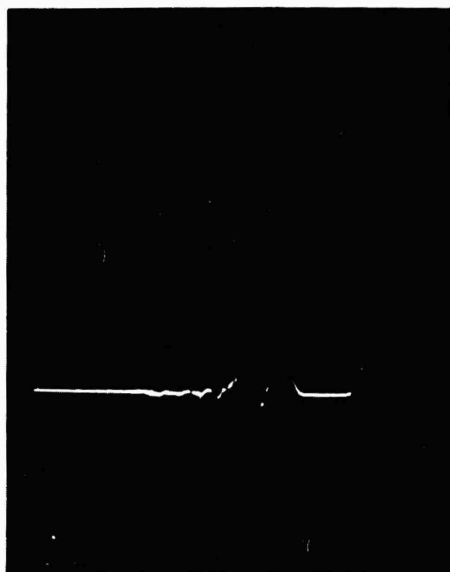


1160 - BC323 Target
1/2" Thickness

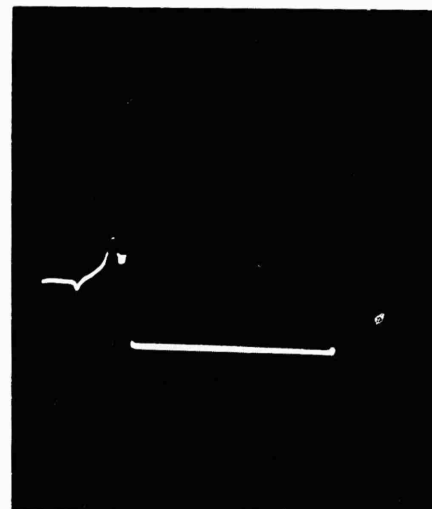


1160 - BC323 Target
1" Thickness

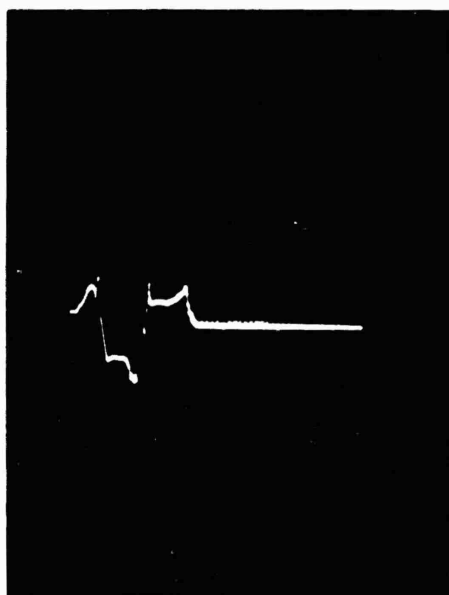
Fig. 17. Quartz Crystal Oscilloscope Traces



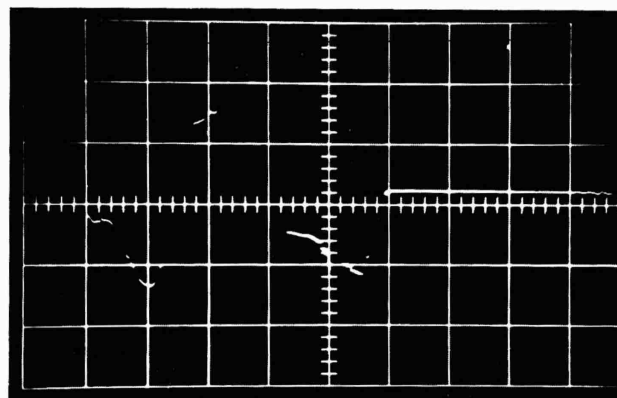
1178 - BC323 Target (Guard ring
signal only)



1181 - BC323 Target



1193 - BC323 Target - Crystal on
1/2 Inch Step



1193 - BC323 Target-Crystal on
1/4 Inch Step. (Pulse left
to right)

Fig. 18. Quartz Crystal Oscilloscope Traces - Time Increasing Right To Left
Unless Noted Otherwise

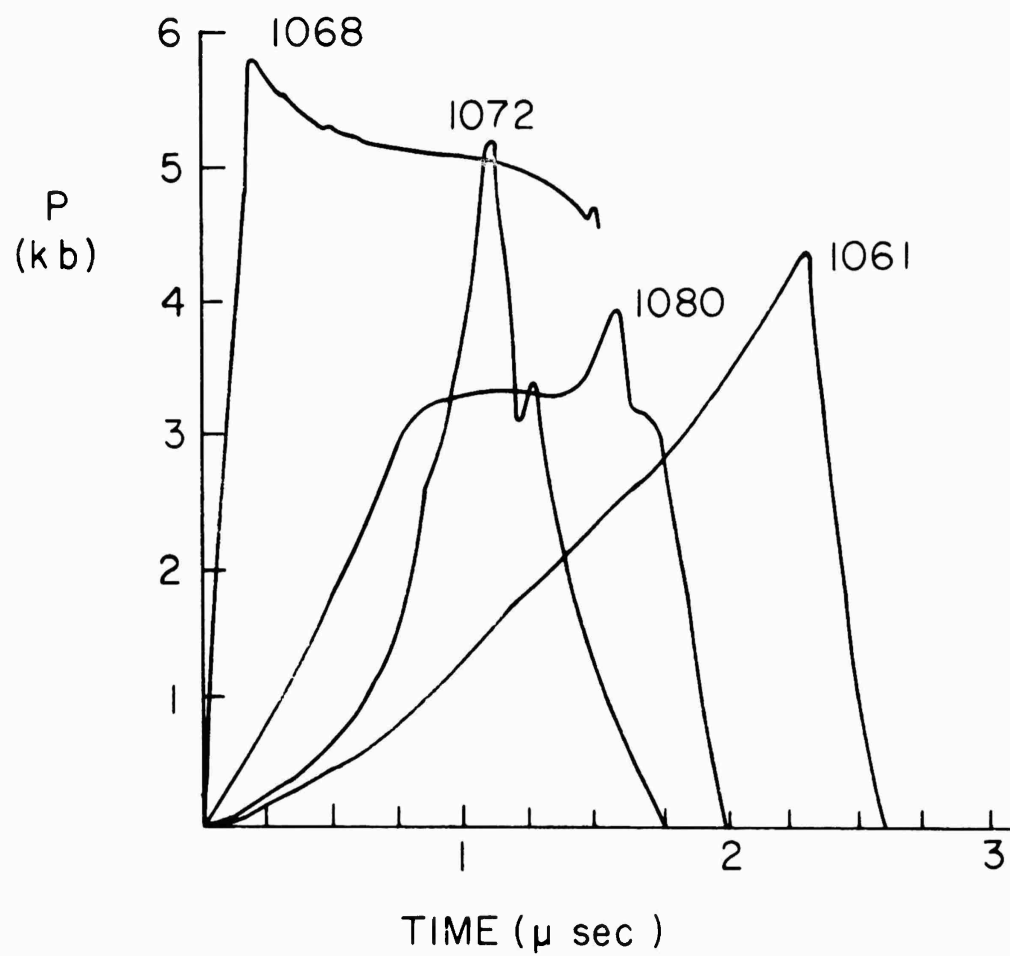


Fig. 19. Compression Profiles in Quartz for BC323 Targets, Impacted by a 1/8" Al Driver

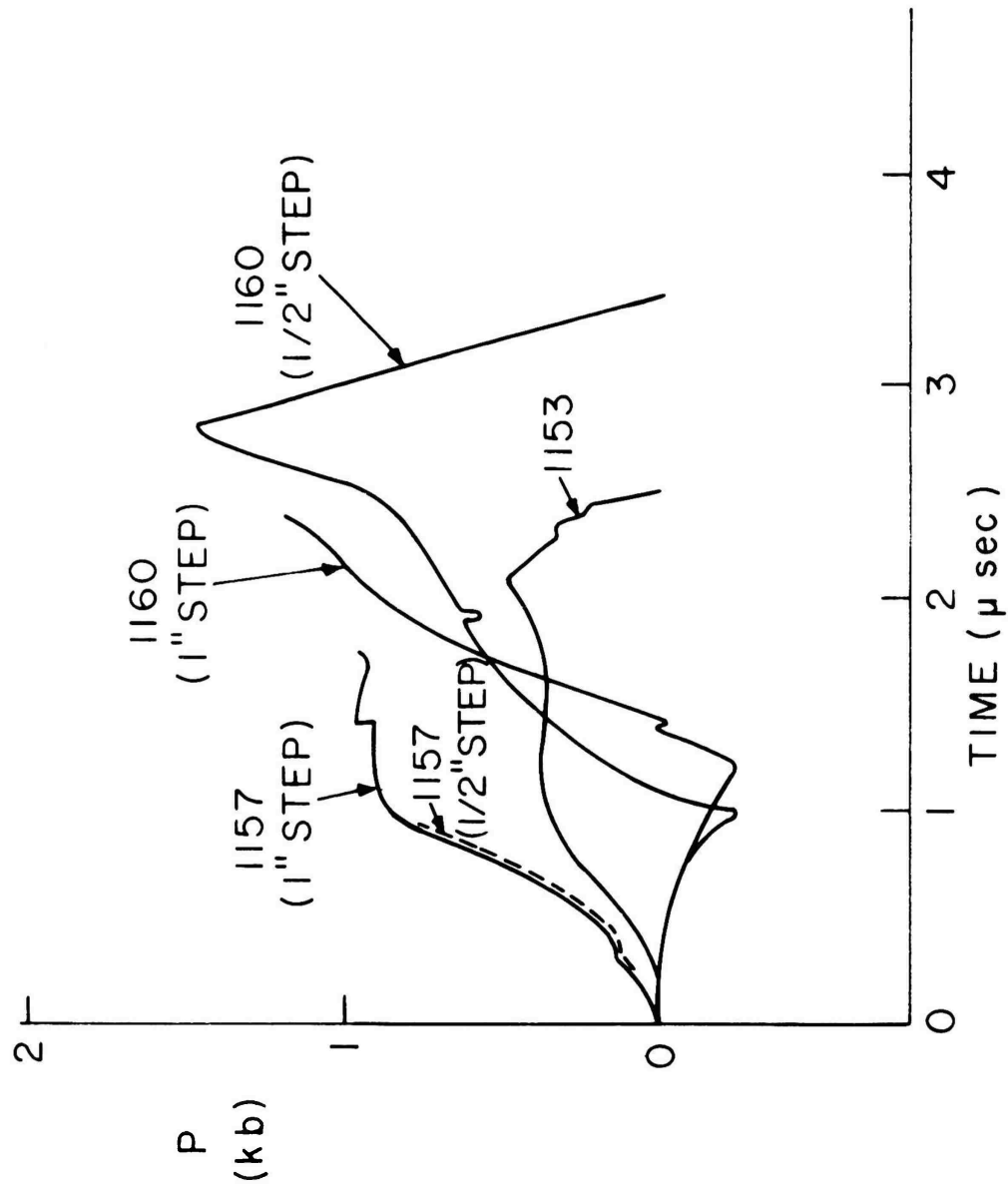


Fig. 20. Compression Profiles in Quartz for BC323 Targets, Impacted by a 1/8" Al Driver

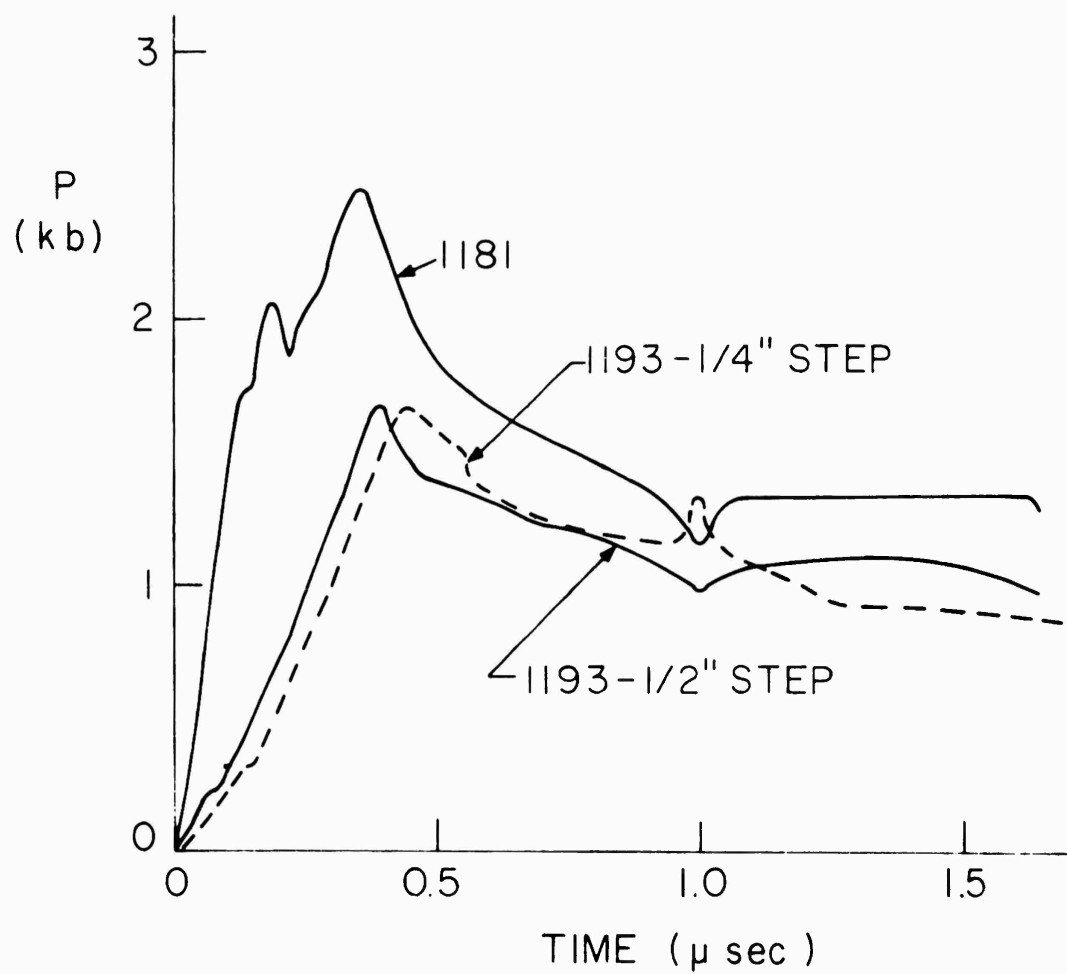


Fig. 21. Compression Profiles in Quartz for BC323 Targets, Impacted by a 1/8" Al Driver



Fig. 22. Quartz Crystal Oscilloscope Trace For Shot 1207. Moving BC323 Target (1 inch) and Stationary Aluminum Driver (1/16 inch). Time Increases From Right to Left.

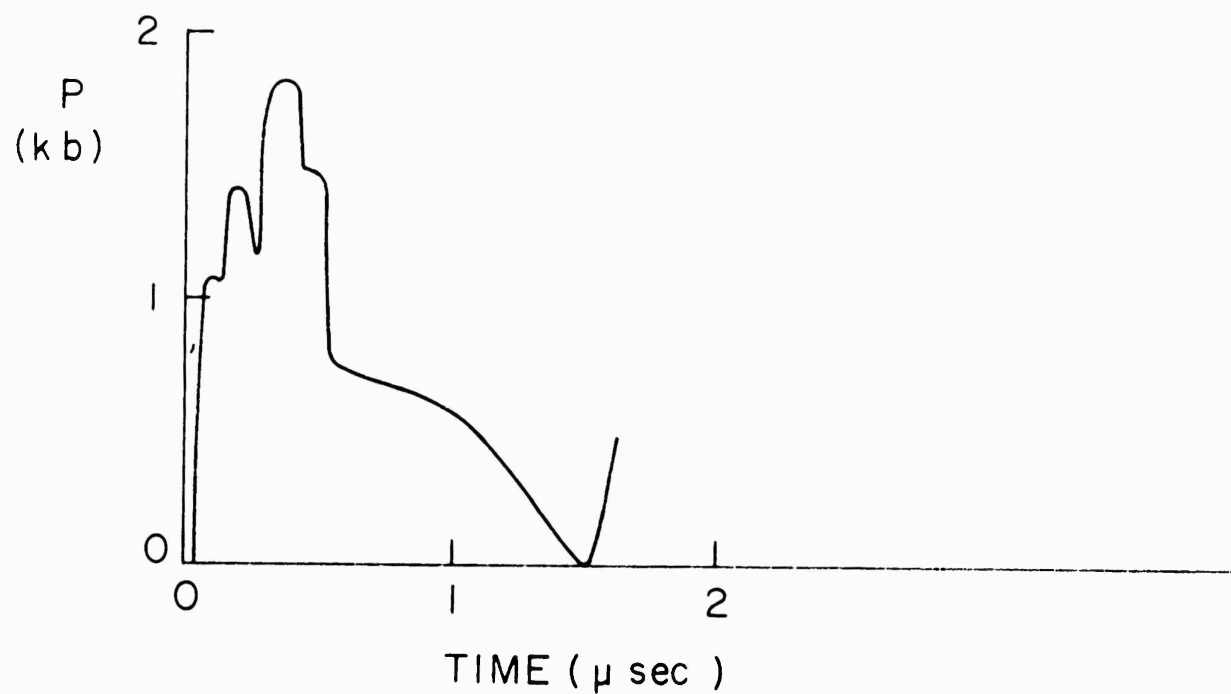


Fig. 23. Compression Profile for BC323 Target,
Impacted by 1/16" Al Driver

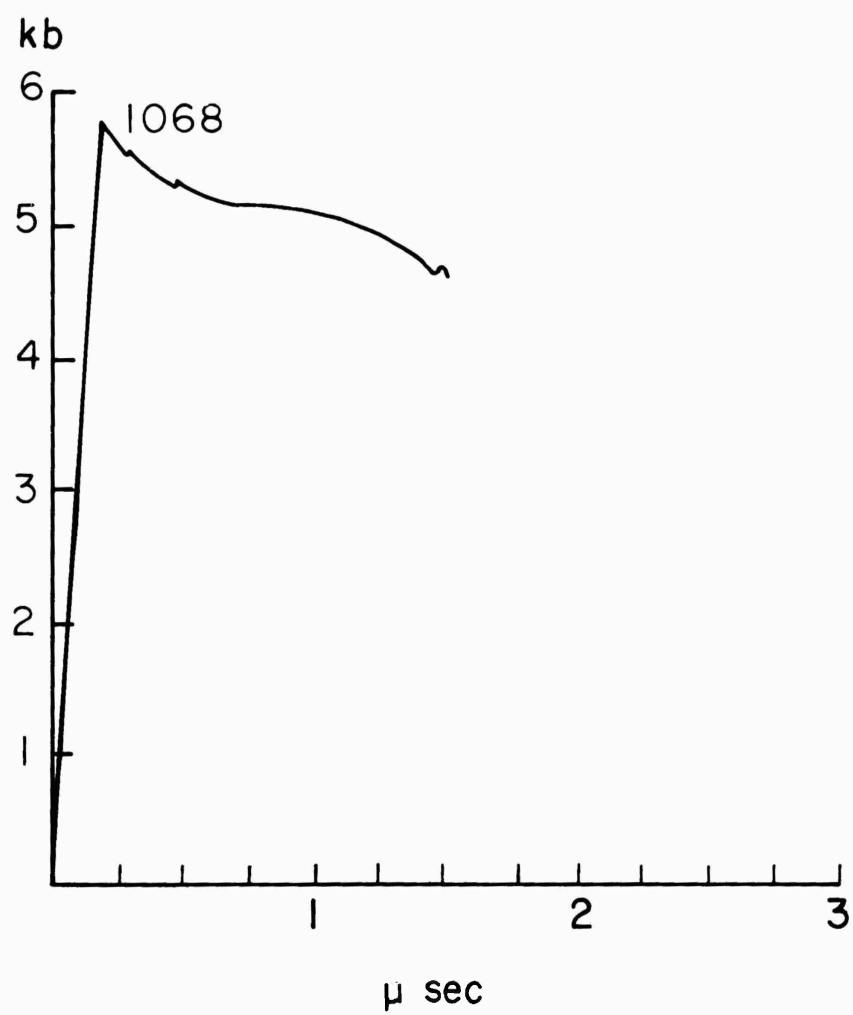


Fig. 24. Compression Profile in Quartz for BC323 Target, Impacted by a 1/8" Al Driver

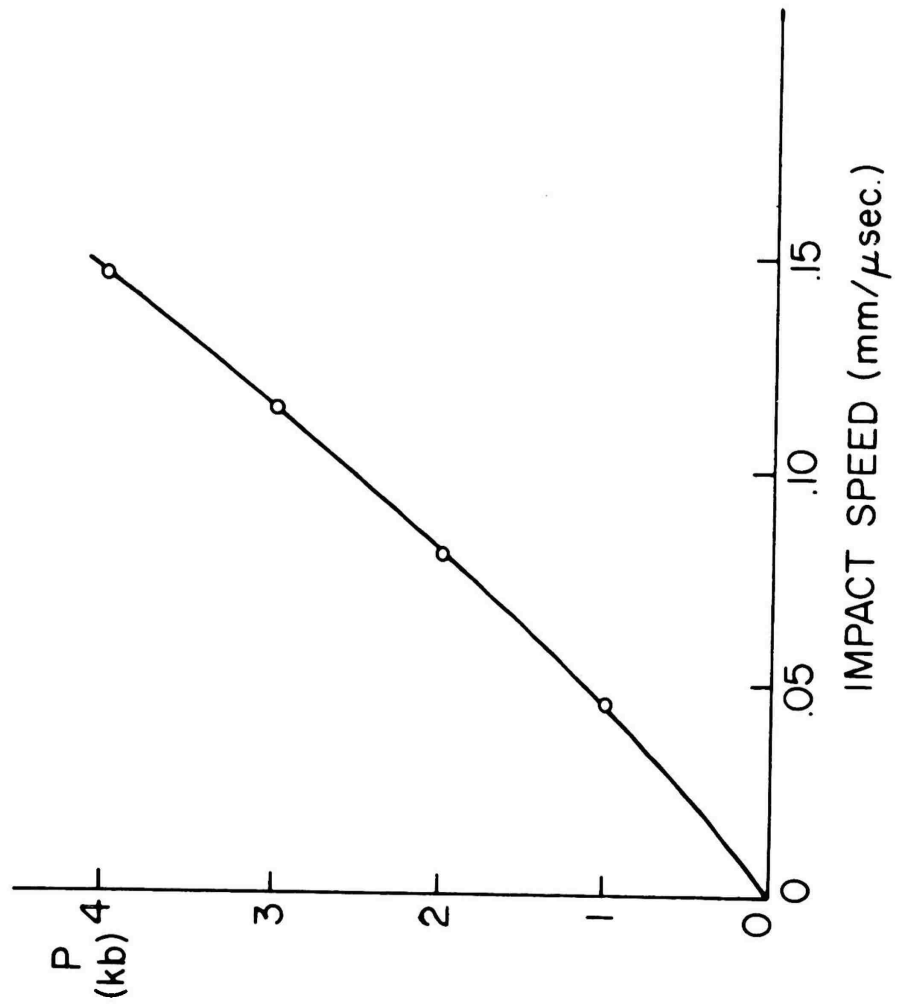
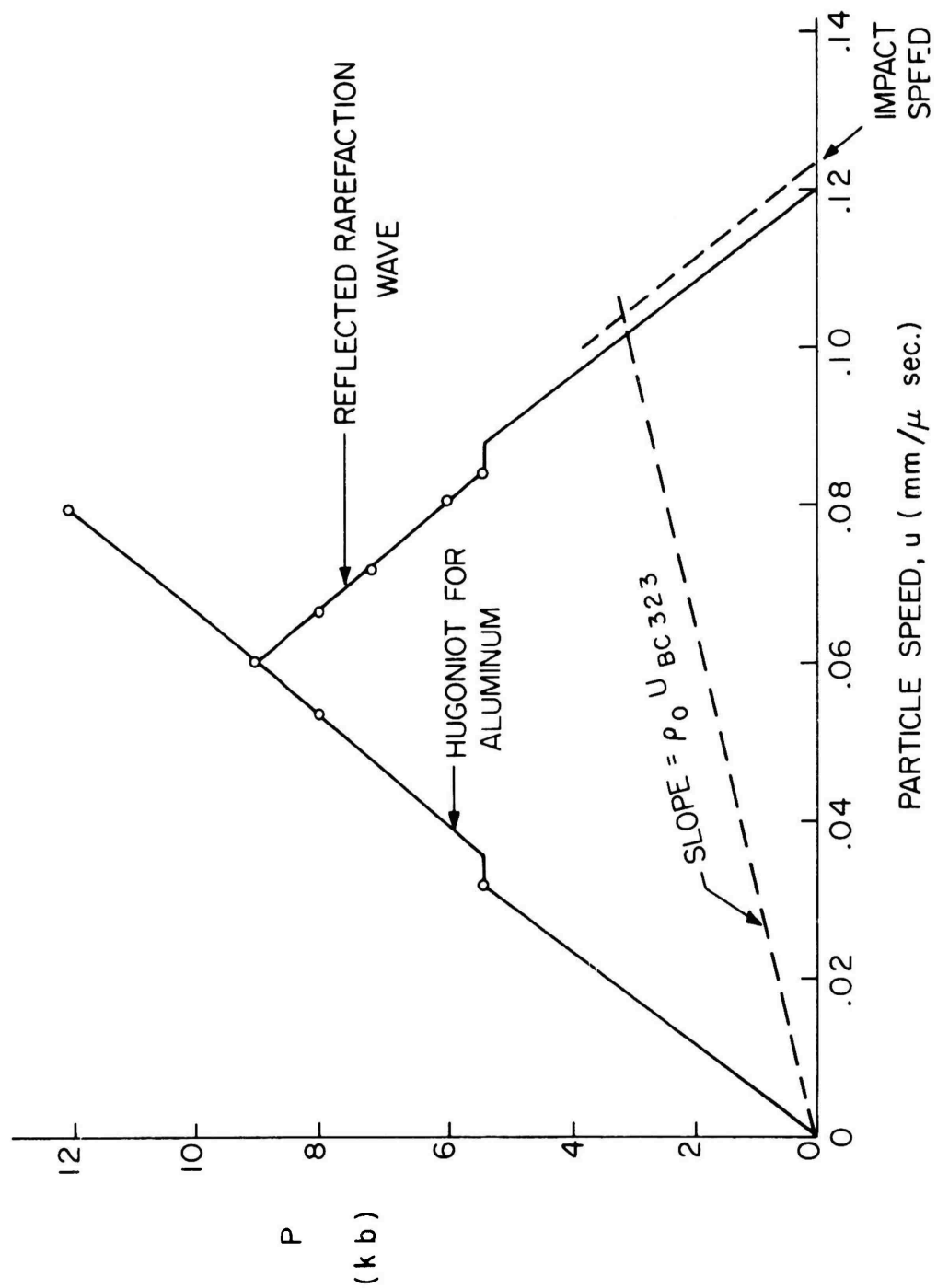
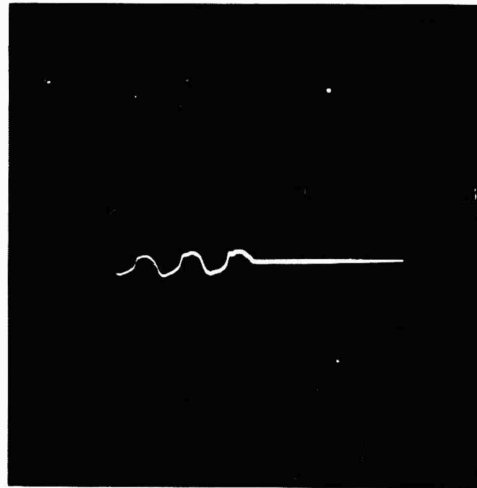
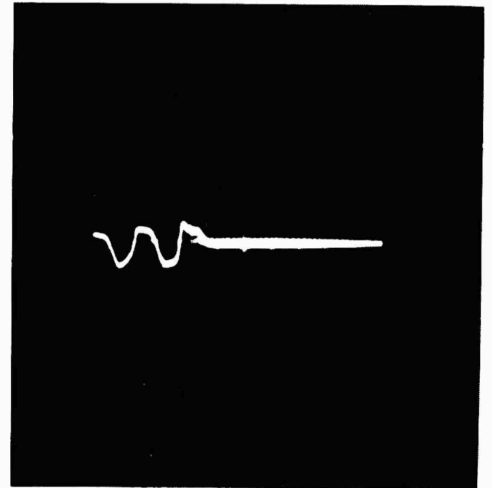


Figure 25. Impact Curve for Aluminum Against BC323





1192 - BC326 Target



1195 - BC326 Target

Fig. 27. Quartz Crystal Oscilloscope Traces For Impacts of Aluminum On BC326. Time Increases From Right to Left

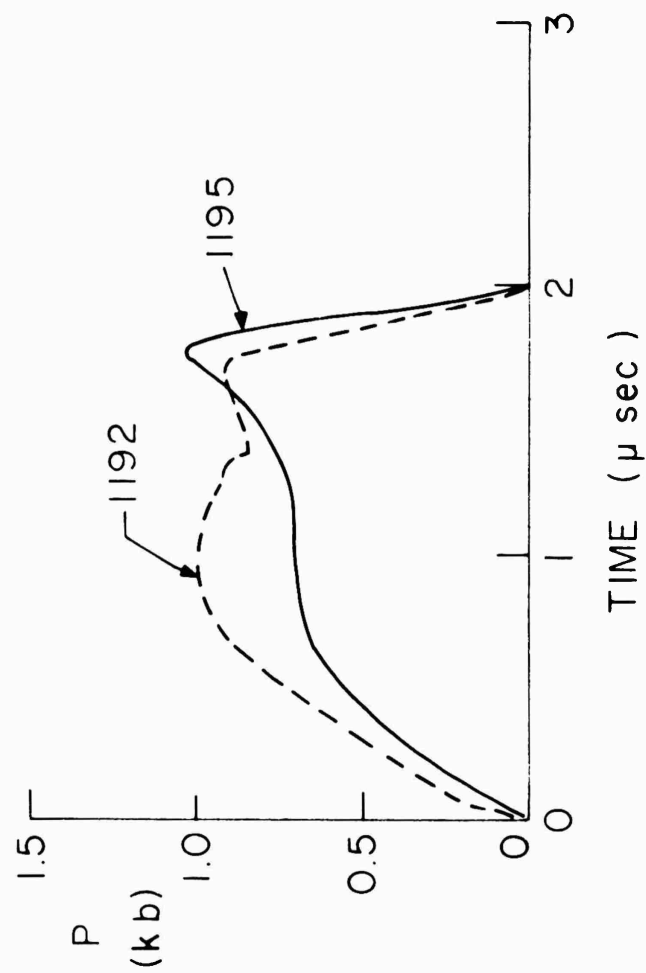
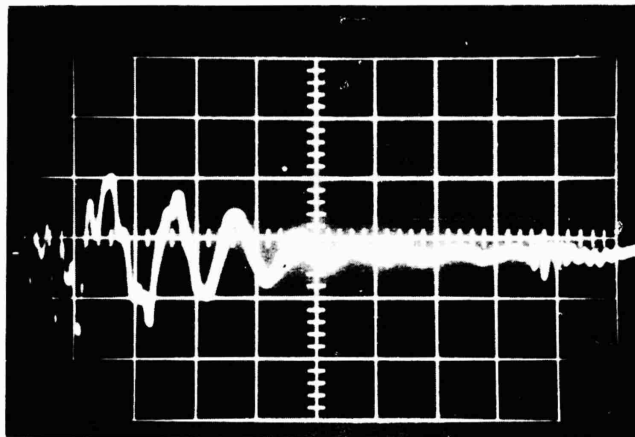
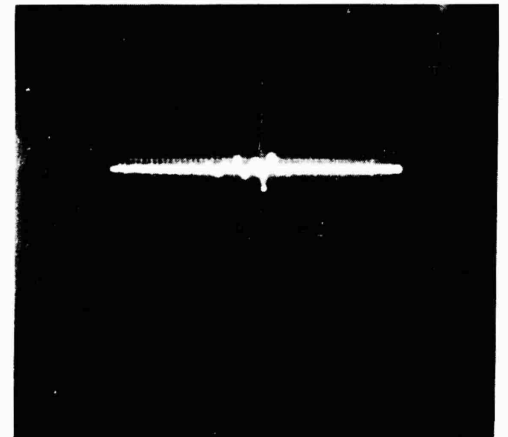


Fig. 28. Compression Profiles in Quartz for BC326 Targets
Impacted by a 1/8" Al Driver

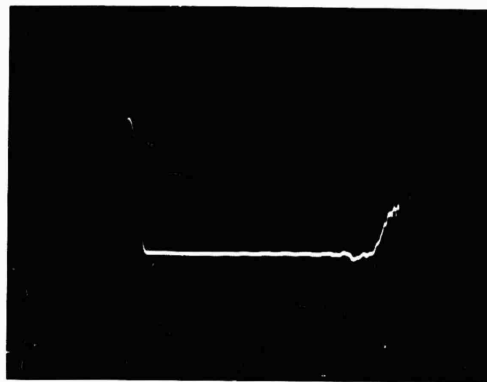


Internal Trigger, Sweep $1 \mu\text{sec/cm}$
From Left to Right. 0.2v/cm .

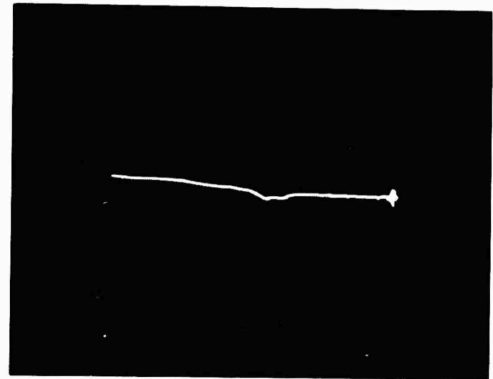


Raster Pin Trigger. Sweep $5 \mu\text{sec/cm}$
From Right to Left. 0.5 v/cm .

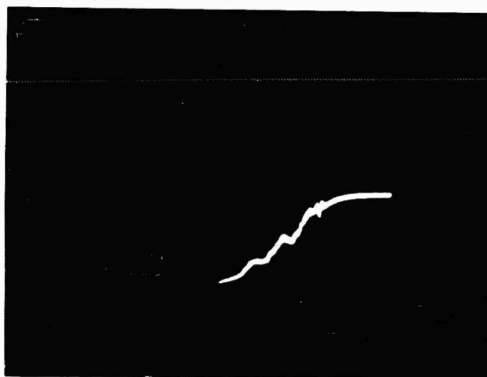
Fig. 29. Quartz Crystal Oscilloscope Traces for Impact of BC326 Target
Against 1 mm BC326 Driver. Shot 1253



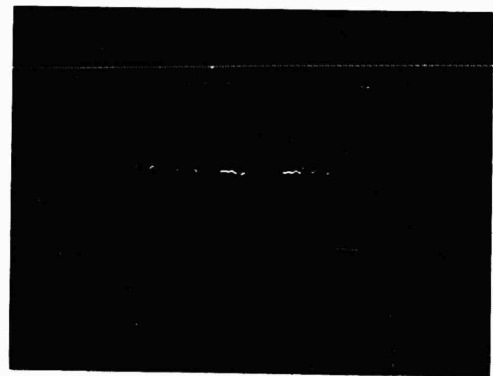
(a) 1075



(b) 1077



(c) 1091



(d) 1214

Fig. 30. Photomultiplier Signals Obtained in Light Transmission Impacts.
All sweeps, right to left.
(a) #1075 - $10\mu\text{sec}$ Full Sweep. Vertical Deflection, 0.1 v/cm .
(b) #1077 - $25\mu\text{sec}$ Full Sweep. Vertical Deflection, 0.2 v/cm .
(c) #1091 - $1\mu\text{sec/cm}$ Sweep. Vertical Deflection 0.2 v/cm .
(d) #1214 - $100\mu\text{sec}$ Full Sweep. Vertical Deflection 0.5 v/cm

e. Fracture Formation

(1) Fractures in BC323

As stated in the Interim Final Report (Ref. 1), the internal fractures produced in the glassy BC323 resin were well-defined disk-shaped fractures with irregularly-shaped initiation sites. The diameters of these disk fractures varied with the driver plate thickness and hence, presumably, with the shock pulse duration. During the present phase of the program, additional measurements were made on specimens from the previous shots, using only fractures which were parallel to the rear target surface and in a plane one driver-plate thickness from the rear surface. These were almost certain, therefore, to be primary fractures. The radii of such fractures were directly dependent on driver plate thickness, as is shown in Table VII and in Fig. 31. Those results show that each fracture radius was about 25% of the thickness of the driver plate which produced that fracture. It might be concluded from this that either the fractures grew with roughly constant velocity during passage of a tensile pulse equivalent in duration to that of the initial compressive shock or the fractures grew with increasing velocity during passage of a tensile pulse whose effective duration was less than that of the initial compressive shock.

Since the initiation sites also changed in size with changing driver plate thickness, it was supposed that there might also be a direct dependence of disk radius on "equivalent" initiation radius. This did not prove to be the case, as is shown in Fig. 32, although a fairly smooth curve was obtained. In theory, if one considered the initiation sites to be Griffith-type flaws (either present initially or generated by the stress), it should be possible to extend Berry's one-dimensional treatment of the motion of a moving crack (Ref. 11) to two dimensions. From the relationship of disk fracture radius vs initial crack radius, one might obtain a measure of how greatly the observed stress exceeded that critical stress which is just sufficient to initiate fracture growth. Such a treatment was considered in this program but was not pursued at length; because it was felt the number of required assumptions rendered the treatment unwarranted. For example, the one-dimensional theory assumes constant applied stress and an infinitely thin initial line crack. In the fractures caused by impact, the stress was most certainly not constant, and the irregularity of the initiation sites obtained would invalidate any assumption regarding initial crack shape.

It was found earlier that any dependency of IIP threshold for fracture on pulse duration was sufficiently small to be hidden within the experimental scatter. To determine whether the length of run through a target would change the threshold IIP, impacts were made on 2-inch thick BC323 targets (Table VIII). A single fracture was obtained at an IIP of only 0.39 kb—less than that obtained on 1-inch targets for drivers of the same thickness. The result would indicate that the pulse amplitude had not decreased in going from

a thickness of 1 inch to a thickness of 2 inches. Clearly, this could not be expected to extend to targets of infinite thickness. There was evidence for edge effects in the 2-inch targets; since several fractures were obtained oriented at a large angle from the rear surface. Photographs of primary fracture surfaces from two of the impacts in this series are shown in Figs. 33 and 34. The presence of debris in the central initiation site is evident in Fig. 34b.

For some materials, such as organic glasses, it is known that internal fractures heal with time and that patterns initially present after impact gradually disappear (Ref. 12). Fractures in BC323 were examined within a few minutes after impact (Table VIII) to determine whether or not such an effect might also be present in this resin. Optical microscopy revealed no changes in pattern at intervals of 5 minutes, 1 hour, and 24 hours after impact. A photograph of such a fracture is shown in Figure 35. Electron micrographs of replicas of portions of the same fracture surface are shown in Figures 36-38. These replicas were prepared as follows:

- (1) Cellulose acetate wet with acetone was pressed against the surface.
- (2) After drying, the replica was mechanically stripped from the surface,
- (3) The replica was then shadowed with platinum (at a 45° angle) in vacuum.
- (4) Carbon film was evaporated normally onto the metal-shadowed replica.
- (5) The cellulose acetate primary replica was dissolved in acetone, leaving a carbon film replica with a metal deposit. This replica was then ready for photographing in the electron microscope. The arrows in the photographs indicate the direction in which light would fall on the surface at an angle of 45° if one were viewing the original fracture specimen. An electron micrograph of the fracture surface from Shot 1164 is shown in Fig. 39. The texture of this surface resembled closely that shown in Figs. 36-38.

(2) Fracture in BC326

In previous impacts using BC326 as the target material, conical fractures were obtained, indicating tearing of the rubbery type resin. During the more recent work, fractures were obtained, particularly at low impact velocities, exhibiting rather marked differences in appearance from those fractures obtained previously. Higher impact velocities resulted in a mixture of fractures, some of which resemble conical tearing and others which exhibit completely different features. An example of a low velocity fracture within the bulk specimen, photographed by transmitted light, is shown in Fig. 40. One of the striking points to be noted is the lack of distinguishing features immediately surrounding the initiation site (Fig. 40b). In addition, the initiation site or region appears as a cluster of individual sites rather than as one cohesive region (Fig. 40c). The fracture shown in Figure 40 was obtained from the target in shot 986, the detailed data for which are listed in Table IX. This target had remained in one piece after impact. Figure 41a, taken by transmitted light, shows a relatively high concentration of initiation sites and the considerable overlapping of the fractures radiating from these sites. At the edge of the area of severest damage, the individual fracture

features can be distinguished more clearly (Fig. 41b). The most prominent fracture here shows a fairly well defined circular boundary. Surrounding this boundary is a second fracture zone which is reasonably but not exactly concentric with the boundary of the first. In fact, there is no indication of the secondary fracture zone in the bottom right hand quadrant. Apparently, the secondary zone is the result of reflected stress waves. However, the extent of the secondary fracture was insufficient to result in comminution of the sample such as normally appears in the more rigid, glassy resin. This might have resulted in part, from greater attenuation of the stress pulse in the lossy material.

Other single fractures from shot 986 are shown in Figs. 42 and 43. In Fig. 42a both the primary and secondary fractures are clearly defined, but the more interesting point is that the initial fracture is essentially featureless. It displays neither the tear lines usually associated with the "star" fracture nor the fine surface markings characteristic of the disk fractures produced in the rigid material. The two crescents which appear at the top left and at the bottom right of the primary fracture circle are optical artifacts resulting from depth of field and scattering effects. In Fig. 43a, showing another fracture area, the boundary of the primary fracture is well defined, but there does not seem to be any definite boundary of the secondary fracture.

The fractures shown in Figs. 42a and 43a were made by observations of light transmitted through the bulk sample. This did not permit any definite conclusion regarding the topographical details of the fracture planes. To reveal the free surfaces of some of these fractures, cylinders of material were removed from the bulk samples by means of a cork borer. The cores were then broken or cut to reveal the free surfaces of the fractures. Photographs of these surfaces are shown in Figs. 42b and 43b.

For the surface shown in Fig. 42b, the plane of the fracture was not parallel to the boundary of the sample, and the fracture had to be exposed by cutting away the extraneous material. In doing so, part of the feature was damaged. It is evident that the feature is essentially circular, rather than elliptical as might have been inferred from Fig. 42a. This is because the plane of the fracture in the latter figure was not normal to the optical axis. From the exposed surface it can be seen that the fracture is essentially featureless, there being essentially no tear marks. Both the primary and secondary fracture zones have well defined boundaries. It appears that the primary fracture zone is not absolutely planar; since at the upper end of the surface in the photograph there is a depression indicated by the shadow and at the lower end there is an elevation sliced through in the cutting operation. Even so, the fracture is essentially planar rather than conical as was observed for the earlier fractures (Ref. 1).

This characteristic is also evident in Fig. 43b, where again the primary fracture zone is essentially planar and is featureless except for the

pronounced tear line almost exactly bisecting the disk. Again the primary fracture zone is circular; whereas it appeared elliptical in Figure 43a because of its orientation. Both the primary and secondary fracture boundaries are well defined. The surface was marred at the lower edge by the cutting procedure.

Fractures obtained in another impact (shot 996) exhibited features similar to those just described. Of the five major fractures in the central portion of that specimen, not one of the surfaces was found to lie in a plane parallel to the target surface. Rather, the fracture surface was inclined from 10° to 45° to the expected plane. While not conical in shape, the fracture surfaces were not perfectly planar either, but appeared to be disk-shaped. They were characteristically featureless, showing neither tears nor parabolic features. Of the five initiation sites, three were nearly round and two were irregular in shape.

On the supposition that the marked differences in the more recent fractures in the rubbery material were the result of the lower impact velocity, a shot was made (1023) more closely approximating a shot obtained earlier in the program (849). Photographs of the free surfaces of the fractures so produced were obtained using transmitted light. These surfaces were revealed by breaking apart the sample during the examination procedure. Typical fracture surfaces obtained in this way are shown in Fig. 44. The central fracture zones do not necessarily have the same diameter. Neither are the fracture zones limited in number. An example is that of Fig. 44b in which there are at least four roughly concentric, though poorly defined, boundaries. These fractures appear to be essentially planar. However, this can be misleading because some of the features displayed in the figures lie within the bulk of the specimen rather than at the surface. Fig. 44c illustrates the added complexity that parabolic markings were obtained similar to those observed previously in the more rigid resin. (See Figs. 23 to 25 in Reference 1). However, the apex of each parabola in Fig. 44c is oriented away from the central initiation site rather than towards it. In this respect, the orientation is consistent with the orientation of the conical tears observed earlier.

Shot 1027 was made using an impact velocity somewhat lower than that in shot 1023. The free surfaces of fractures so obtained are shown in Fig. 45. The features here range from rather pronounced tear lines to almost negligible markings. The central dark region in Fig. 45a was a cylindrical hole extending into the sample, indicating a void in the material at that point. Fig. 45b is a further illustration of a rather poorly defined fracture zone boundary. Fig. 45c, on the other hand, indicates the presence of ripple marks which were previously seen only in fractures in the rigid BC323.

An example of an internal fracture in BC326, with more striking features than exhibited by most fractures, is shown in Fig. 46. This specimen

was obtained from an impact with a 13 mm driver and measured nearly 8 mm in diameter. Although the fracture was circular and well defined, each of the circles in Fig. 46 merely denotes the field of view of the microscope, and thus only a portion of the fracture is shown.

On first appearance, the features in Fig. 46 resemble the parabolas observed in BC323 fractures. There is an important difference, however. The parabolas in the more brittle material are oriented towards the initiation site (that is, the apex is closest to the center of spall); whereas the reverse is true for the rubbery material. In one instance the latter was also found for the more brittle resin. Of all the fractures in BC326 examined, only one displayed markings resembling true parabolas. A photograph of that surface is shown in Fig. 47. Such features were much more prevalent in the more brittle BC323 where the effects of stress concentrations ahead of the main crack are more pronounced.

A simple diagram serves to illustrate how such parabolas are formed (Fig. 48). If the moving planar wave front intersects circular wave fronts emanating from a stress concentration such as A, and both fronts move with the same velocity, the intersection defines a parabola. If the circular wave front moves faster than the planar front, a hyperbola is described and if the circular front moves slower than the planar front, an ellipse is described. Generally, these velocities are the same, hence a parabola is usually described. Berry has discussed this phenomenon at some length previously in Ref. 13. It should be noted that in the case of the fractures discussed in this report we are not dealing with planar wave fronts but with relatively large circular fronts (from the central initiation sites) which then overtake the small circular fronts emanating from sites such as A in Fig. 48.

An example of a possible stress concentration site which could be the focus of a parabola is shown in the central portion of the electron micrograph in Fig. 49. The replica was prepared from the BC326 fracture surface.

Additional electron micrographs of a BC326 fracture surface are shown in Figs. 50 and 51. It is of interest to note that the texture of this surface resembles closely that of the other BC326 surface (Fig. 30) but differs markedly from the surface textures in the BC323 surface (Figs. 36-39).

To determine whether or not the fracture surfaces in BC236 would heal with time, an impact was made and the surface examined within five minutes. A photomicrograph was taken within an hour and again at the end of 24 hours. As shown in Fig. 52, on this scale no change in surface features had taken place. Slight differences in the photographs are the result of change in focus.

TABLE VII

Disk Fracture and Initiation Site Radii in BC323 Resin

Serial	Driver Thickness (mm)	Disk Fracture Radius (mm)	Initiation Site Radius (mm)	IIP (kb)
932	12.7	3.32	0.157	0.42
864	6.4	1.5	0.0513	0.55
864	6.4	1.5	0.0463	0.55
843	6.4	1.25	0.0302	0.59
909	3.2	0.81	0.0247	0.49
912	3.2	0.756	0.0198	0.6
912	3.2	0.756	0.0236	0.6

TABLE VIII
Impact Data for BC-323 and BC-323 Drivers (1/4" thick)

Serial	Target Thickness (in.)	Breech Pressure (psi)	Sabot Mass (g)	Gas Pressure (microns)	Impact Speed (mm/ μ sec)	IIP (kb)	Remarks
1164	2	--	2234	75	0.03	0.39	Sabot broke loose prior to firing, due to pressure leak—one internal fracture 1/4" from rear surface.
1165	2	55	2334	50	0.048	0.64	One fracture 7/16" from impact surface. One fracture 9/32" from rear surface.
1183	2	56	2620	200	0.031	0.40	Many fractures in central region 5/16" to 1/2" from rear surface of target.
1231	1	60	2213	5	0.036	0.45	Fresh fracture produced for immediate optical and electron microscopic examination.

TABLE IX
Impact Data for BC-326 Targets (1" x 4" x 4") and BC-326 Drivers

Serial	Driver Thickness (in.)	Breech Pressure (psi)	Sabot Mass (gms)	Gas Pressure (microns)	Impact Speed (mm/ μ sec)	IIP (kb)	Remarks
845	1/4	70	1875	150	0.057	0.74	No fracture: target intact.
846	1/4	200	1886	5	0.094	1.45	Single conical fracture denotes threshold.
848	1/4	300	1957	5	0.110	1.80	Very many conical fractures, most in a plane 6 mm from free surface, a few 6mm from hit surface oriented 180° to the former, a few randomly distributed.
849	1/4	260	1825	20	0.104	1.68	Very many fractures in a plane 6 mm from free surface.
982	1/4	270	2037	50	0.097	1.55	Several well defined fractures resembling neither conical tears nor disk fractures.
986	1/4	255	2026	50	0.095	1.48	Same type of fractures as observed in #982.
996	1/8	250	2000	50	0.094	1.45	Five major fractures in central region of target and positioned from 5 to 10 mm from free surface. Appearance of fractures similar to those in #986.
1023	1/4	270	2000	100	0.102	1.65	Large number of fractures with varying appearance, both conical and disk type included. Boundary of fractures about 7 mm from free surface.
1027	1/2	240	2057	100	0.095	1.48	Same type of fractures as in 1023 but not quite so numerous. Central plane of fractures equidistant from free and struck surfaces.
1215	1/4	120	2069	20	0.071	1.0	Many internal fractures but no detached spall. Used for immediate study of fresh fracture.

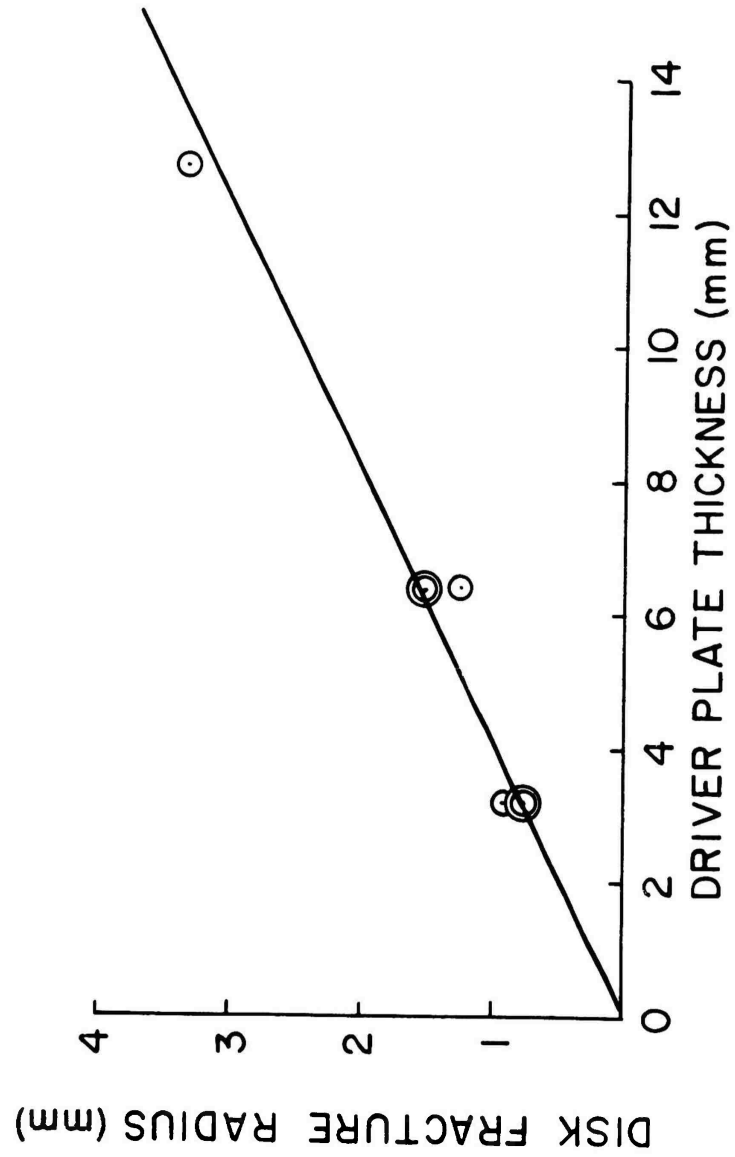


Figure 31. Dependence of Disk Fracture Radius In BC323 Resin
On Driver Plate Thickness

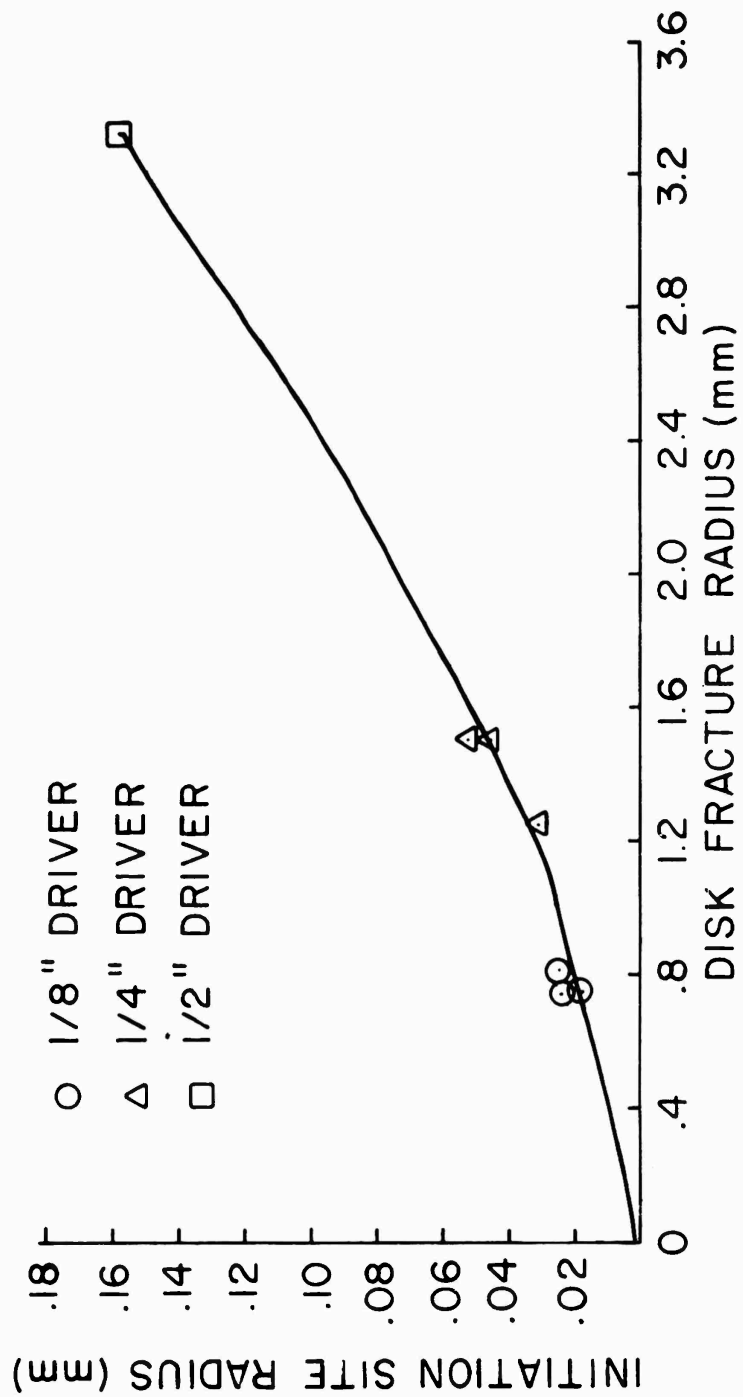
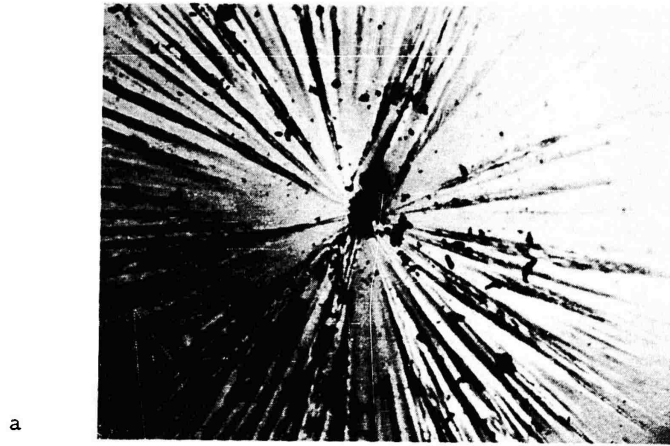
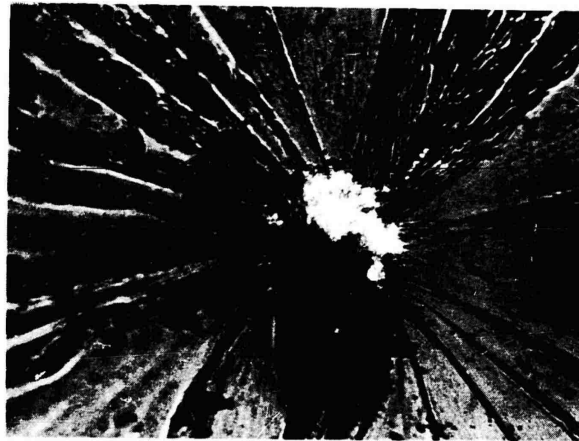


Fig. 32. Relation Between Fracture Radius and Size of Initiation Site in BC323 Resin



a



b

Fig. 33. Disk Fracture Surface (Impact Side) Produced in 2-Inch Thick BC323 Resin. Shot 1164 (a) Mag. 76X (b) Mag 300 X

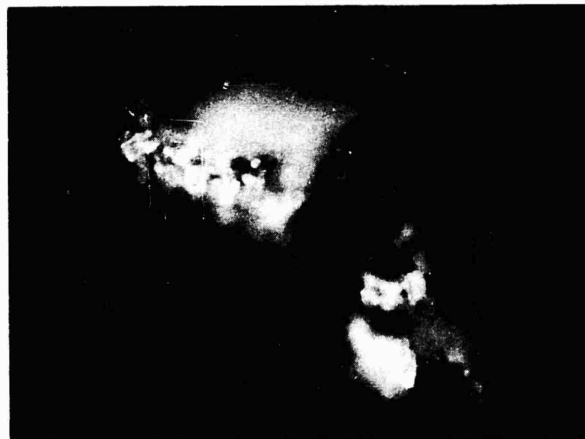
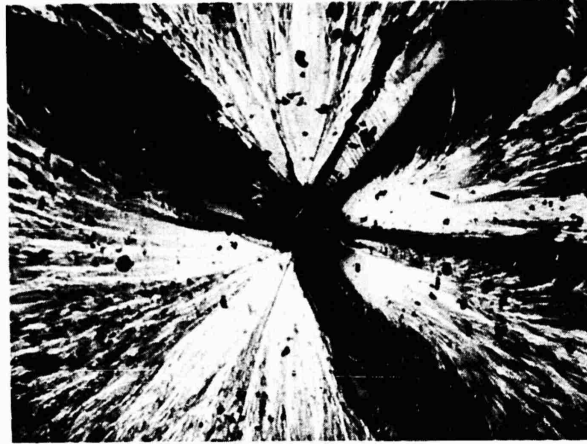


Fig. 34. Disk Fracture Surface (Opposite Impact Side) Produced in 2-inch Thick BC323 Resin. Shot 1165 (a) Mag 76X (b) Mag 300X. Note Debris in Central Hole



Fig. 35. Fresh Fracture Surface in BC323 Resin.
Shot 1231



Figure 36. Electron Micrograph of BC323 Fracture Surface.
Shot #1231. 16,400X



Figure 37. Electron Micrograph of BC323 Fracture Surface.
Shot #1231. 20,000X



Figure 38. Electron Micrograph of BC323 Fracture Surface.
Shot #1231. 16,400X
80

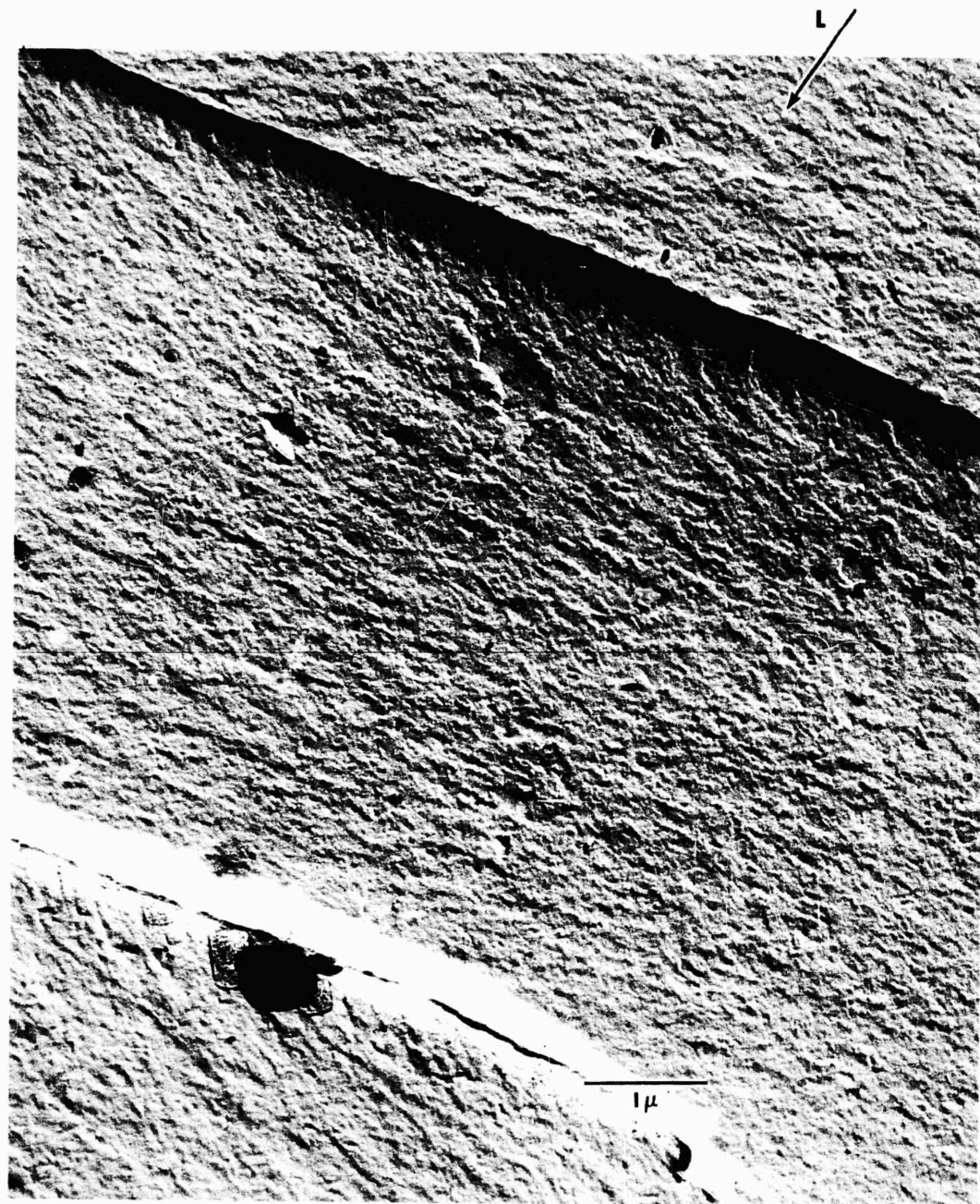


Figure 39. Electron Micrograph of BC323 Fracture Surface.
Shot #1164. 20,000X

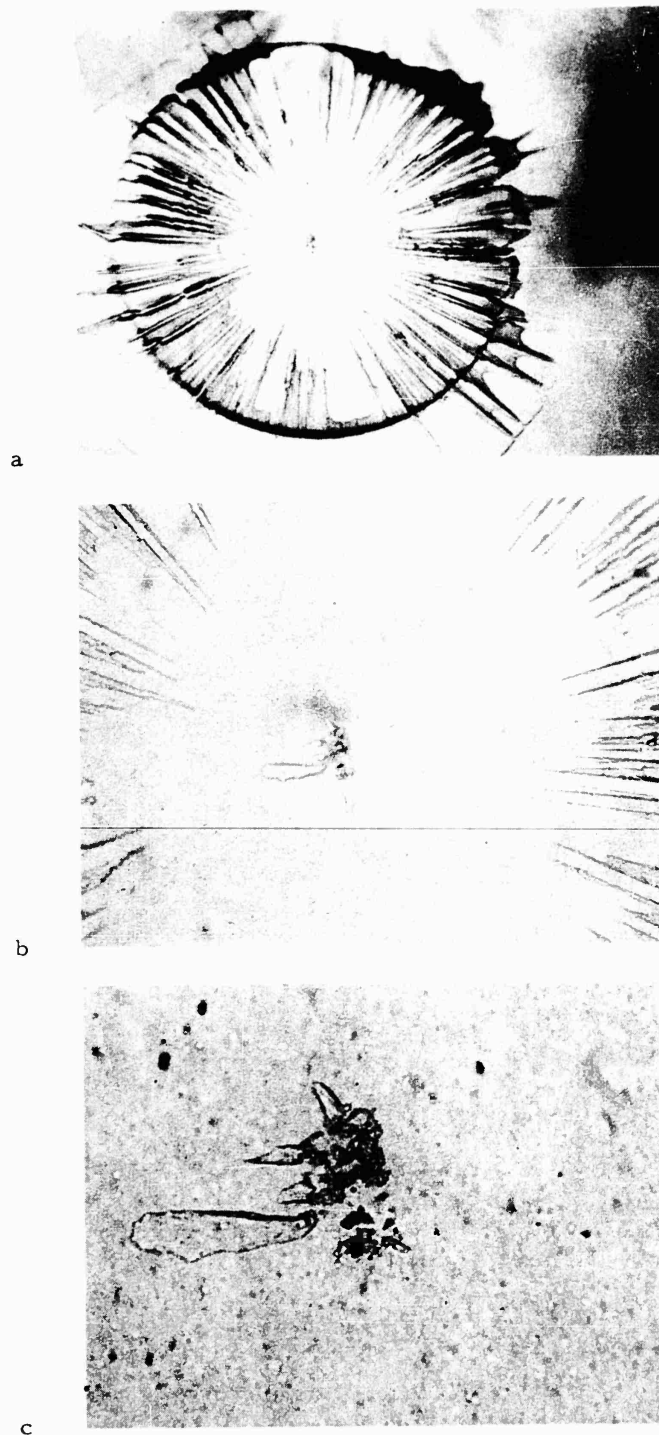
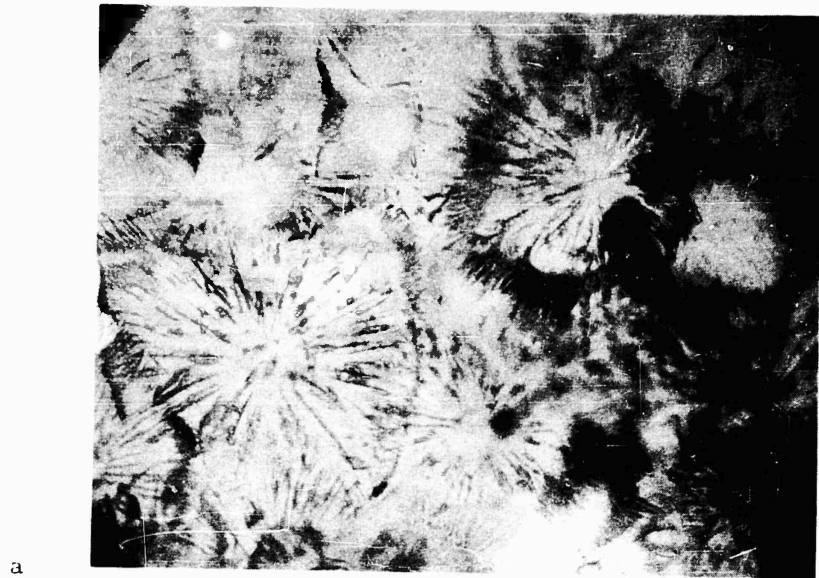
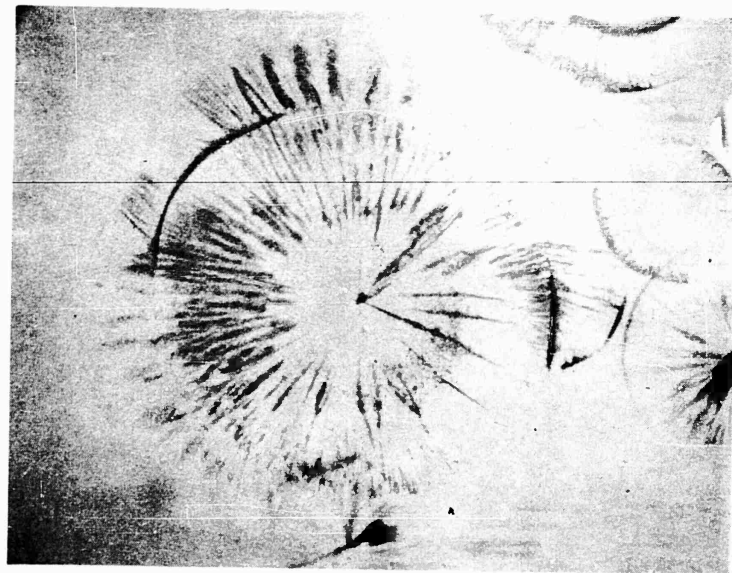


Fig. 40. Fracture Surface Within Impacted BC-326 Specimen. Shot #986.
 (a) Fracture Disk. 29X. (b) Initiation Site .106X. (c) Initiation
 Site - 300X



a



b

Fig. 41. Fractures Within Impacted BC-326 Specimen. Shot #986 Mag. 10.6X
 (a) Cluster of Sites. (b) Individual Sites

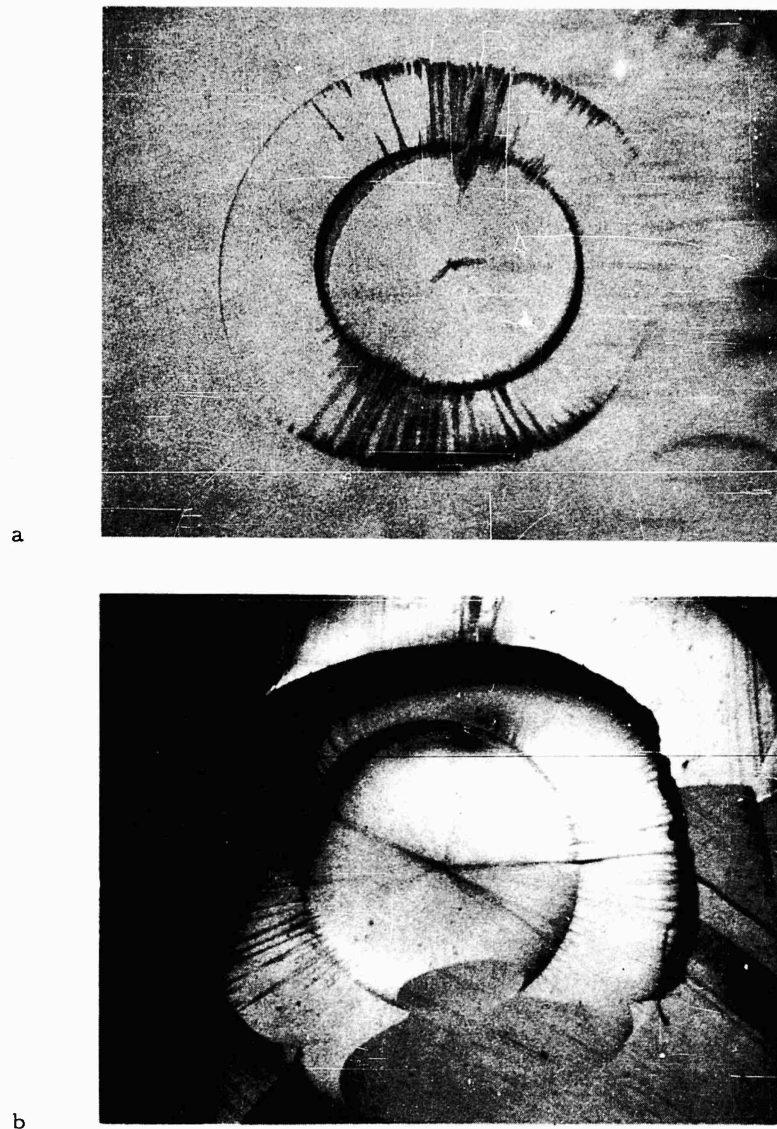
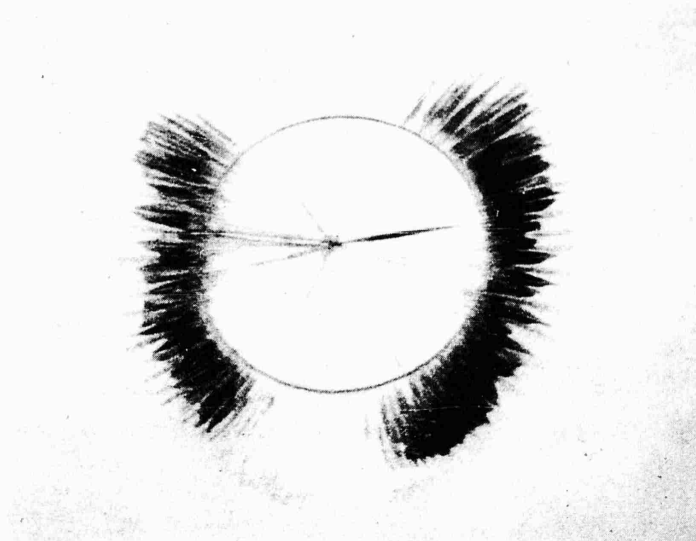


Fig. 42. Single Fracture Within BC-326 From Shot #986.
(a) Fracture Intact Within Specimen. Transmitted Light. Mag. 17X
(b) Free Surface of Fracture. Reflected Light. Mag. 18X



a



b

Fig. 43. Single Fracture Within BC-326 From Shot #986. Mag. 17X
 (a) Fracture Intact Within Specimen. Transmitted Light.
 (b) Free Surface of Fracture. Reflected Light

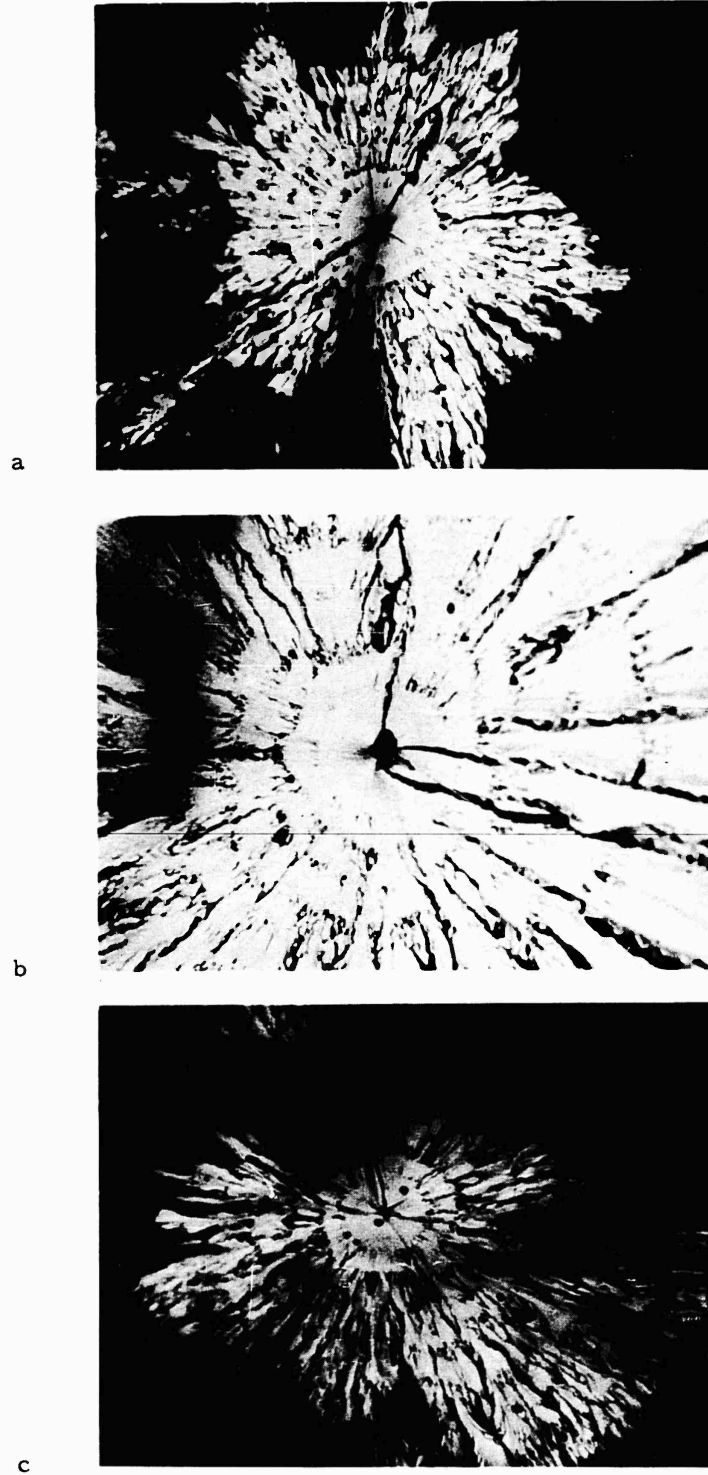


Fig. 44. Free Surfaces of Fractures From Impacted BC-326. Shot #1023.
Magnification 108X



Fig. 45. Free Surfaces of Fractures From Impacted BC-326. Shot #1027. Magnification 108X

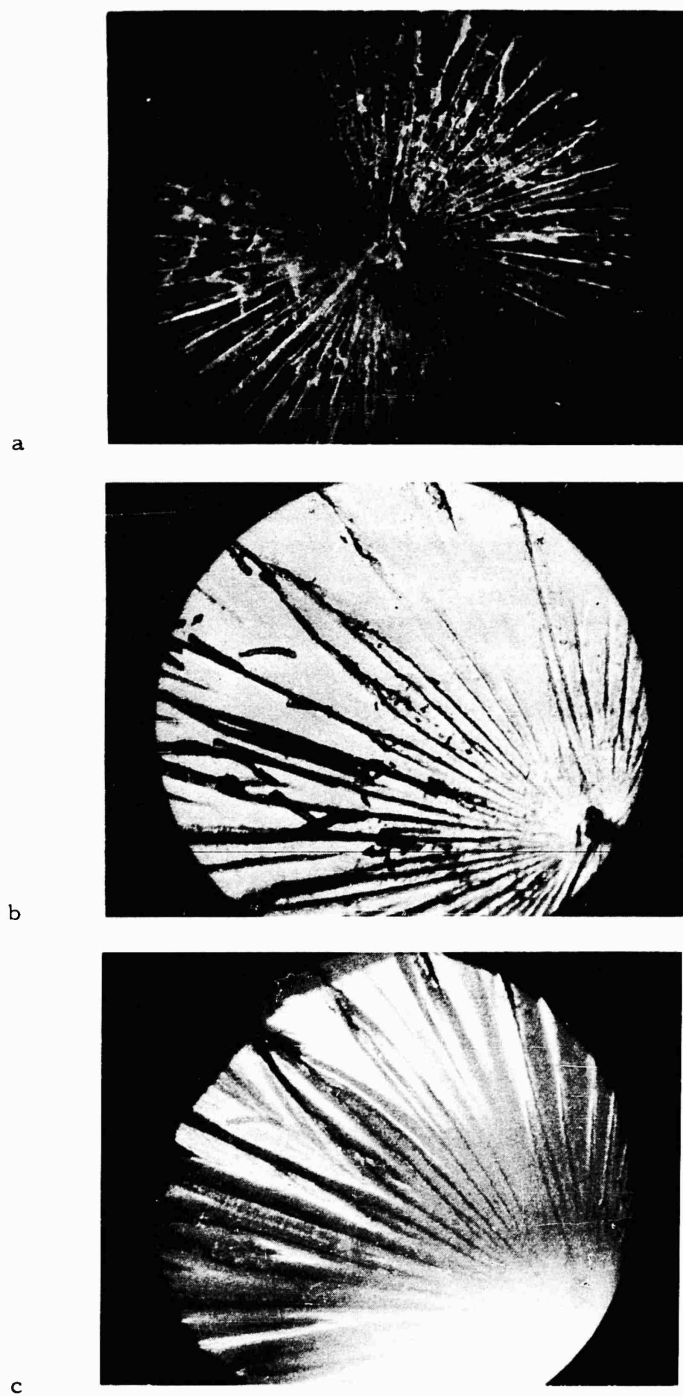


Figure 46. Internal Fracture in BC326. Magn. = 40x
 (a) Transmitted Light. Dark Field Illumination
 (b) Transmitted Light. Bright Field Illumination
 (c) Viewed by Oblique Reflection from Within

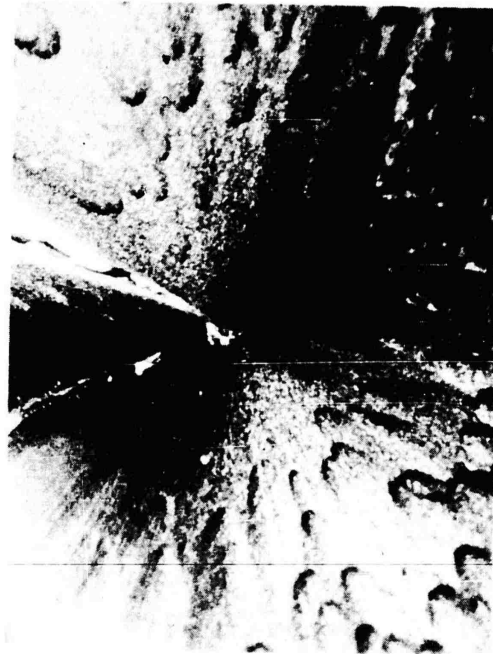


Fig. 47. Parabolas in Fracture Surface of BC326

MOVING WAVE FRONT

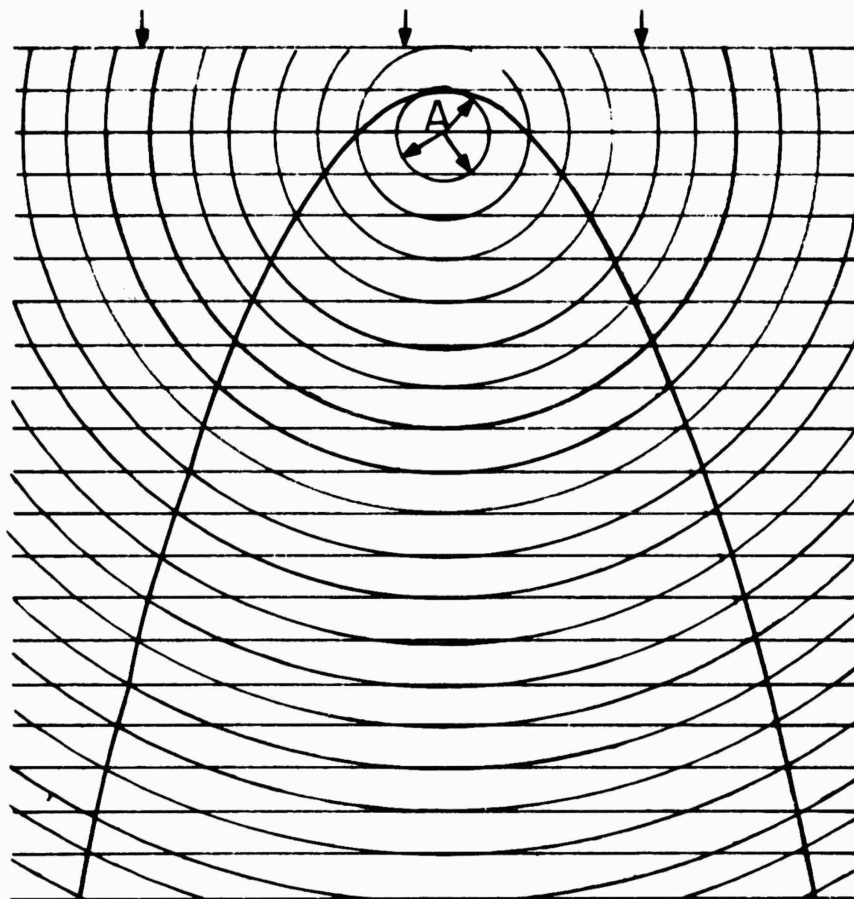


Fig. 48. Formation of Parabolic Marking by Intersection of Planar and Circular Wave Fronts

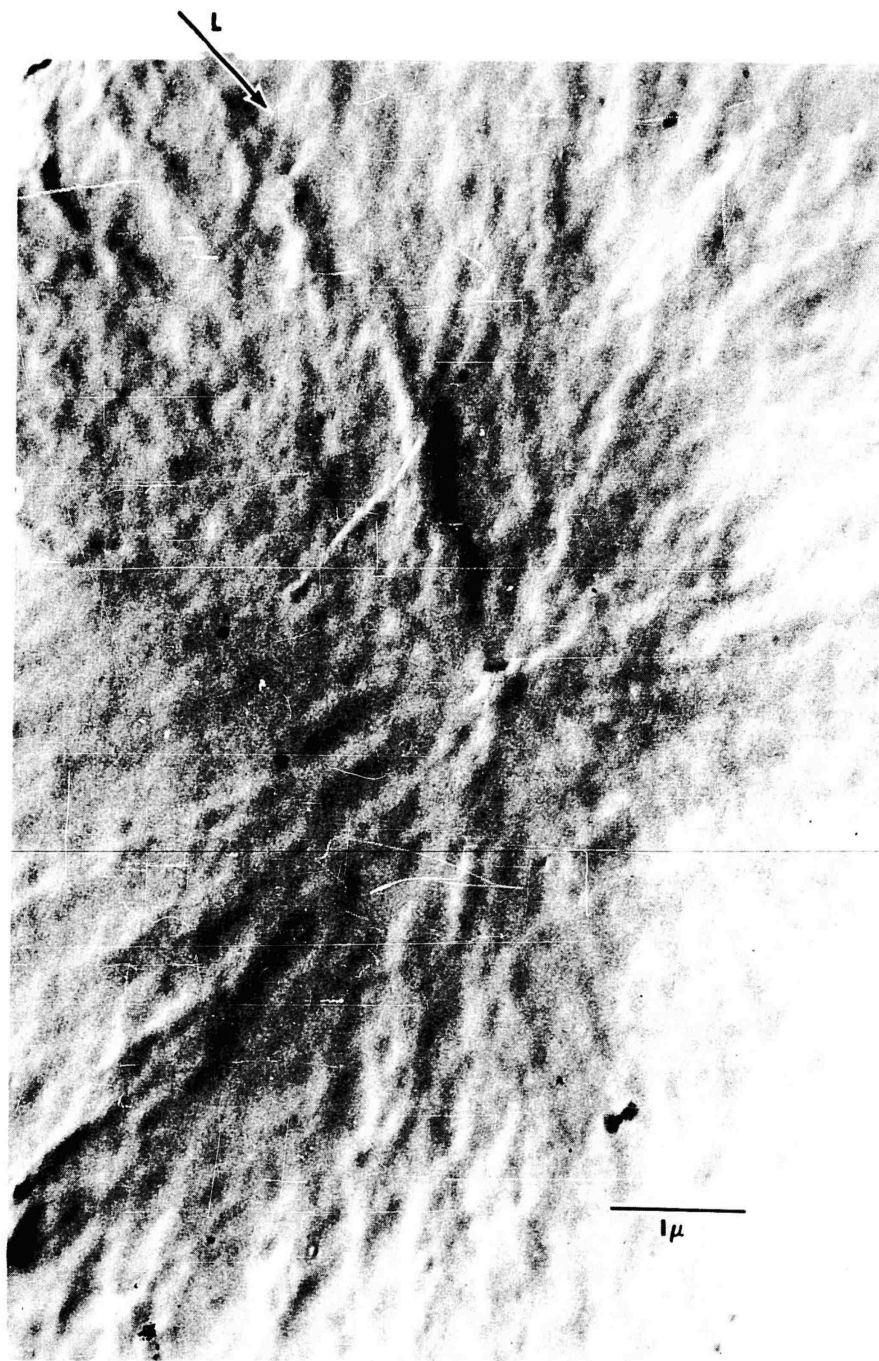


Figure 49. Electron Micrograph of BC326 Fracture Surface
Showing Stress Concentration Site. Shot #1215.
20,000X

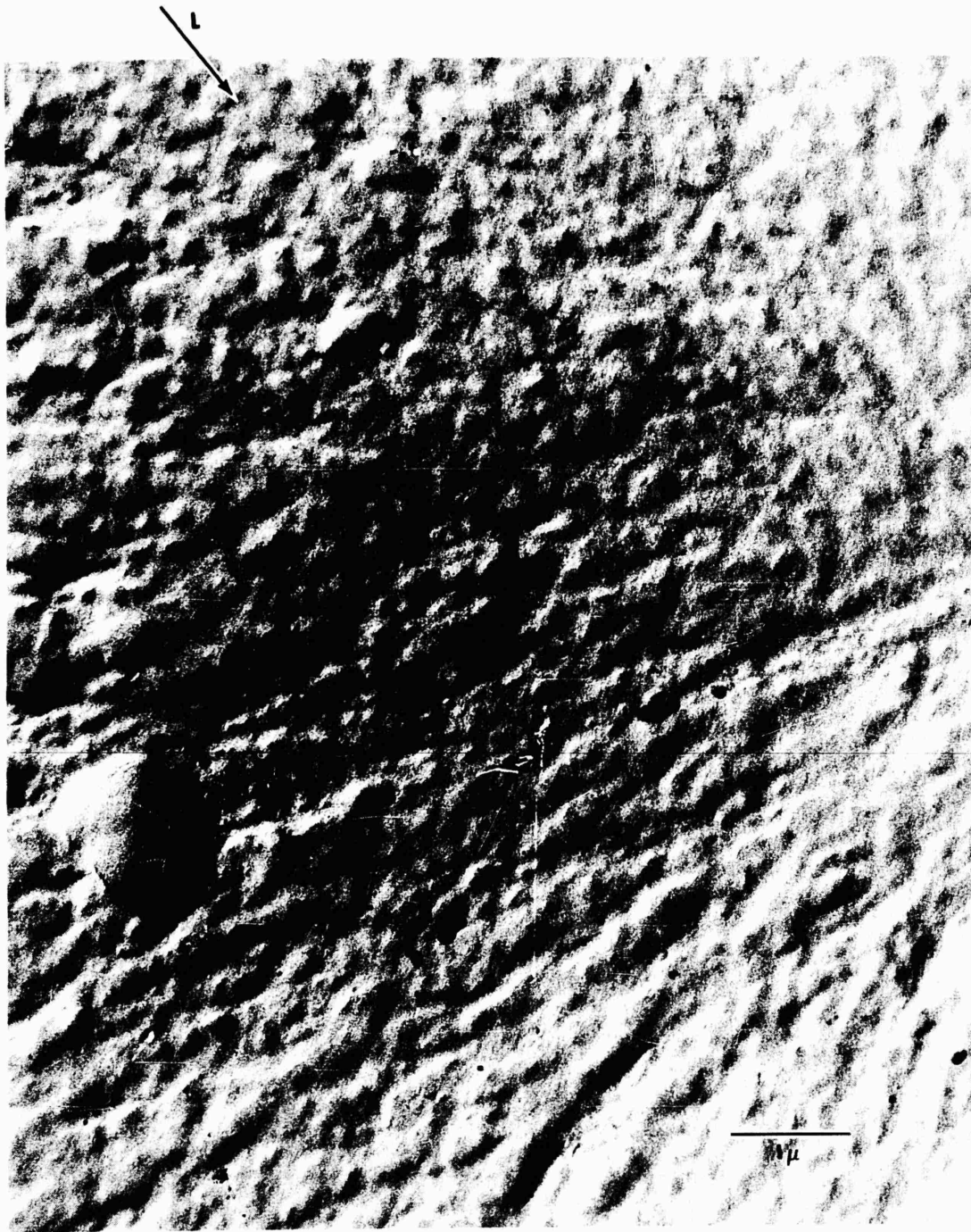
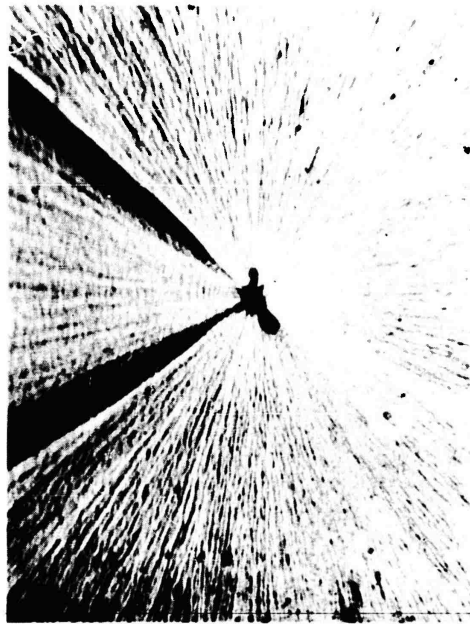


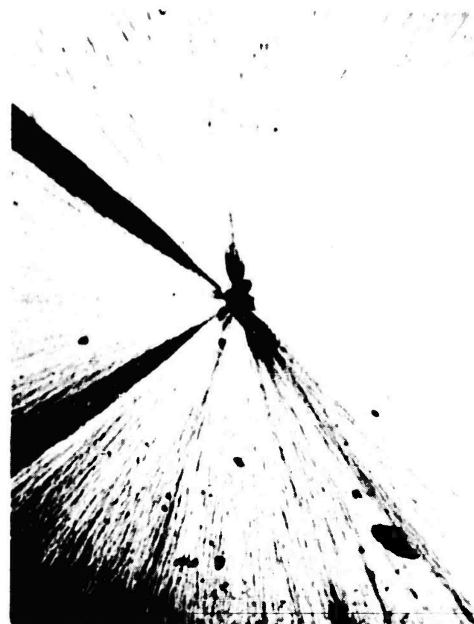
Figure 50. Electron Micrograph of BC326 Fracture Surface.
Shot #1215. 20,000X



Figure 51. Electron Micrograph of BC326 Fracture Surface.
Shot #1215. 60,000X



(a) Immediately After Impact



(b) 24 Hours After Impact

Fig. 52. Fracture Surface in BC326 Resin. Shot 1215. Mag. 76X

(3) Comparison of rigid and rubbery resins

In Ref. 2, it was noted that the convexity and concavity (of concentric zones of increasing radius around any one initiation site) indicated that the reflecting tension wave is at first concave toward the free surface. A forming crack curves toward the region of strongest tension. At first, this is the rear target surface from which the tension wave has just been reflected. Then, characteristically, there is a momentary half followed by a crack straight across nearly parallel to the free surface, then a curvature of the crack which now goes into the tearing mode, with parabolas away from the free surface, as if the peak tensile stress had passed. The crack then stops propagating, as if the stress level has become insufficient to maintain propagation.

In the current work, it was observed that (for both resins but more noticeably for the BC323) further concentric zones can be produced, concave in alternate directions, as if the crack is spread by each of several passes on successive reverberations. Some corroboration for this idea is obtained by observation of interaction of spall-type cracks (roughly parallel to the target faces) with diagonal cracks from edge effects (Ref. 12). Near a corner, where an edge-effect crack has cut back before the arrival of a disk crack, the disk will stop at the diagonal crack, while propagating several more cycles into the body of the target.

The fractures produced in the relatively rubbery BC326 resin exhibited some marked differences from those produced in the more rigid BC323 resin; although several similarities appeared as well. Perhaps the most prominent difference was that the fractures in BC323 were much more predictable than those in BC326. That is to say, the primary fractures in the former were almost invariably well defined, disk-shaped and reasonably parallel to the free surface of the target. Also, the fracture radii were directly dependent on driver thickness. Examination of the microstructure of these fractures generally revealed a large number of parabolic markings indicative of the primary crack front (circular) intercepting smaller crack fronts emanating from stress concentration sites just ahead of the primary front.

The fractures in the rubbery material, on the other hand, varied from star-shaped, conical structures with multitudinous features to fairly well defined circular structures that were virtually featureless, at least to the naked eye. Also, the fracture radii were not directly proportional to driver thickness; even though larger fractures were generally produced by the thicker drivers, within broad limits. Parabolic markings were only infrequently found in the BC326 resin, and the one fracture which displayed these markings most vividly was directly adjacent to a fracture which displayed no parabolic features whatsoever. Some of the fracture surfaces in BC326 were parallel to the rear target surface, but more often they were inclined at angles up to 45° from the expected plane.

In both resins, secondary fractures were often found concentric with the primary fractures, indicating multiple reflections of the shock in the target. As many as six or more of these concentric features were frequently in evidence for the BC323; while in BC326 it was unusual to find spreading during later reverberations.

Other differences include changes of ratio of the area of the central portion to the area of the whole disk. In BC326, the fracture disk produced during the rise of the tension tends to be slightly larger in area, relative to that in BC323; while the surrounding annulus produced after the tension crest has passed appears to be relatively narrower in BC326 than in BC323. This effect is consistent with the indications of quartz crystals: BC326, relative to BC323, appears to show more gradual slope of the wave front and greater tendency toward development of tensile shock in the tail of the pulse.

Another feature, rather common in BC326 and apparently absent in BC323, is the tendency of the edge of a fracture disk to curve sharply away from the free surface (thus following the retreating tensile crest) and burst into a star of thin cracks with their greatest component normal to the target faces. This effect is probably related to the greater Poisson's ratio for the BC326, which causes the lateral components of the stress tensor to be nearly equal to the component along the wave vector. If continued, this type of fracture will lead to the break up of a BC326 target into small fragments, even in the absence of applied bending moments. This type of breakup has indeed been noticed for strongly pulsed plastic targets of all types, including BC323. However, for the latter material, it has not been actually observed in the arrested phase.

Turning from the macroscopic aspects to the microscopic, we note that detailed quantitative treatments of deformation, creep, dissipation, hysteresis, the formation and propagation of cracks, etc., have been given for crystalline materials on the basis of dislocation theory. See Ref. 9, especially pages 231-285, and the bibliography cited there. These considerations apply only in part, and not quantitatively, to plastics. For the latter, irregularities in the packing of molecules cover a wide spectrum of sizes and types, and have a range of effects on fracture initiation and propagation. Qualitatively, we still may expect suitable gaps in the structure to act as crack initiation sites, as in crystalline solids, and may expect to find effects similar to defect production when propagating cracks cut across irregular molecular distributions. That is, in crystals, when one dislocation is dragged across another, it leaves vacancies in its wake.

In addition, plastics offer the complication of two types of bonding. Along molecular chains and around the rings, the bonding is covalent, while between chains and rings the bonding consists of an occasional covalent cross-link but is mainly van der Waals type, weaker than the covalent type by roughly two orders of magnitude.

X-ray diffraction shows some difference between the organization of BC323 and BC326 resins, although both are nearly randomly arranged. The more glassy, less dense 323 gives a broader, flatter densitometer record, suggesting that the cross links interfere with molecular packing. Indeed, this interference seems to be more serious than the addition of internal plasticizer in BC326.

Covalent cross links increase the number of bonds to be broken by a propagating crack, thus increasing the yield strength when failure is primarily by the Bueche mechanism (Ref. 14). Since the denser, less cross-linked BC326 is actually the more spall resistant, the implication is that most of the bonds involved are van der Waals type rather than covalent, and that even while spalling there is considerable molecular slippage, allowing the molecules to draw into positions more nearly normal to the crack and thus more resistant to parting.

The x-ray diffraction densitometer traces are shown in Figs. 53 and 54 and can be analyzed with the aid of the Bragg formula $d = n\lambda/2 \sin \theta$. Cylindrical film was used, with the sample on axis in a powder camera having 57.3 mm radius, to make 1 mm on film = 1° total deflection, the total deflection being 2θ . Traces are 5 times the scale of the photographic record, making each 2.5 mm from the center of the record equal to 1° of 2θ , or each 10 mm across the record from a feature to its mirror image equal to 1° of θ . Here $\lambda = 1.54\text{\AA}$, $\lambda/2 = 0.77\text{\AA}$.

The first feature is about 49 mm from its image, making $\theta = 4.9^\circ$, $\sin \theta = 0.0854$. For this feature, $d = n \cdot 9\text{\AA}$. This feature is obvious on the BC323 trace and slightly more intense on the BC326 trace. The next feature corresponds to $d = n \cdot 4.53\text{\AA}$ on BC326 and to $n \cdot 4.57\text{\AA}$ on the BC323 trace, with considerable uncertainty in the second decimal. This feature is more intense than the first, being the main peak on the record.

In these plastics, benzene rings contain the main concentrations of scattering electrons. It is therefore perhaps appropriate to discuss the results relative to the graphite diffraction pattern. For the latter, the most prominent scattering comes from the main interlayer spacing ($d = 3.368\text{\AA}$). Since these layers are stacked ABAB..., there are atoms from two layers in a unit cell. If BC323 and BC326 are considered as substituted and highly distorted graphite, the interlayer spacing may be taken as 4.5 to 4.6\AA , with a faint resemblance to hexagonal closest packing indicated by the 9\AA spacing of the approximate unit cell.

If graphite layers were spaced out this far, the density would be about 1.67, rather than the actual 1.24 or 1.27 of our resins. Of course, the resins contain much nonaromatic material, thus lowering the density.

Note that BC326 is better organized and slightly denser than BC323, in spite of having more nonaromatic material. This agrees with the lower compressibility found for BC326 (Section 3.a). These features are all contrary to our preconceptions, but seem to be established: in the presence of intermolecular lubricant and in the absence of cross linking, BC326 appears to settle into an arrangement more compact than that of BC323.

There are slight increases of diffracted intensity corresponding to aliphatic chain spacing (packed for BC326 but for BC323 roughly 5% looser than close packing), C-C distances, etc., but the rest of the record is too smooth to interpret. Evidently the organization is comparable to that in a liquid, rather than that in some polymers for which relatively large well-organized micelles are found embedded in an amorphous matrix.

Another comparison between the glassy and rubbery resins was made by electron micrography of replicas taken from fresh fracture surfaces. At 20,000 times magnification, the region from which a crack in BC326 was initiated may show no flaws, or a barely detectable cluster within a few hundred Å of the center. Cracks do not seem to start from inclusions, and the slight flaws found are not necessarily pre-existent as required by the Griffith theory. On the other hand, the initiation site in BC323 usually seems to be centered on some jagged inclusion or a group of flaws with large components normal to the target surfaces and therefore normal to the stress wave front, to such an extent that the center of an initiation site in BC323 cannot be sharply focussed in a high power optical microscope, and does not yield a satisfactory micrograph even in the electron microscope. This suggests the applicability of some fracture criterion and fracture initiation process in which shear flow is important. The ineffectiveness of artificial flaws' introduced parallel to the wave front (See Ref. 1) also suggests the desirability of a 3-dimensional theory. However, direct application of one which has been worked out for crystalline solids is certainly inappropriate. At the moment, we merely note that the fracture nucleus in either resin appears to be irregular and rather randomly oriented.

The surface of a BC326 crack, replicated within an hour of the fracturing at the firing point, was seen to be covered by rounded domes, usually roughly circular or elliptical, particularly at more than 75,000 Å from the initiation site. Closer to the site, the surface is smoother except for radiating steep edges which are perhaps somewhat analogous to the jogs and surface steps of crystal dislocation theory.

The dome structure or pebbling suggest micelles (regions of well-packed molecular structure in an amorphous matrix), and might be so interpreted except for the x-ray diffraction evidence to the contrary. The breadth of the diffraction features shows that order can hardly be traced much farther than next-nearest neighbors; whereas an inspection of the electron micrograph shows that the domes or pebbles have sizes which approximately

follow a Poisson distribution with a peak near 1100\AA . However, BC326 shows larger regions of approximate order than are found in BC323. Also, the diffraction shows that BC323 itself is not completely random.

Conceivably, the domes in BC326 are the result of fiber-drawing during separation of the fracture surfaces. Snapped fibers could retract, and the stubs could spread to give a pebbled surface. The replication process could help to reduce their heights, particularly in such rubbery material. This explanation is made more plausible by the tendency of the pebbles to occur frequently in rows aligned with the tear marks. Apparently fillets were first drawn radially from the initiation site. The fillets apparently then broke up to fibers, which snapped and partially retracted. These fillets may have occurred when cracks started to propagate on different levels. If cracks start to pass each other, immediate clean tearing can occur, while if roughly parallel cracks succeed in passing on different levels, the included material will then be twisted and stretched to a fillet, which can break up laterally to fibers and separate, as just described.

Elsewhere near the rim of a propagating crack, parting of the BC326 resin will occur most readily where the material is weakest, passing still-intact small regions, which conceivably then draw out and snap. When the fracture disk stops propagating, there should be a jagged or starred edge, trailing off to indistinctness where the gap becomes much less than a wave length of light in thickness. This is observed.

It was stated above that the BC326 replica indicated domes on the fracture surface of the BC326, with a modal diameter near 1100\AA , the average diameters roughly following a Poisson distribution. However, very small domes are practically absent. There are practically none with diameters less than 250\AA . On the other hand, the fracture surface of BC323 is covered with angular block ends, bimodally distributed about peaks at 100\AA and 250\AA (roughly), with very few which are larger than 500\AA . If BC323 breaks into fibers before parting, these evidently tend to be much smaller than those formed by BC326, and snap with much less extension. See Fig. 55.

This contrast is compatible with the differences in organization and in ductility.

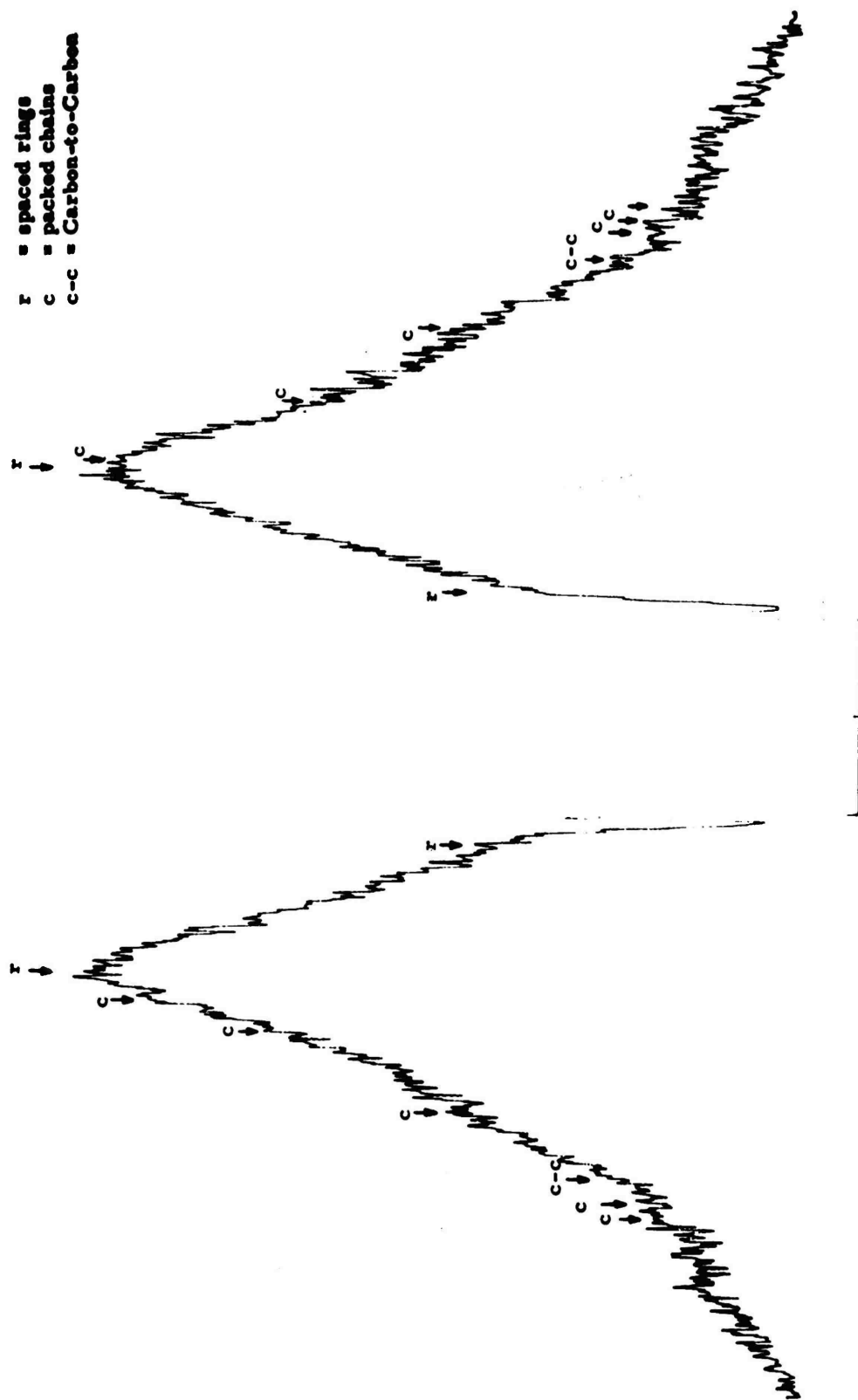


Figure 53. X-Ray Diffraction Densitometer Patterns of BC 326

r = spaced rings
 c = packed chains
 c-c = Carbon-to-Carbon

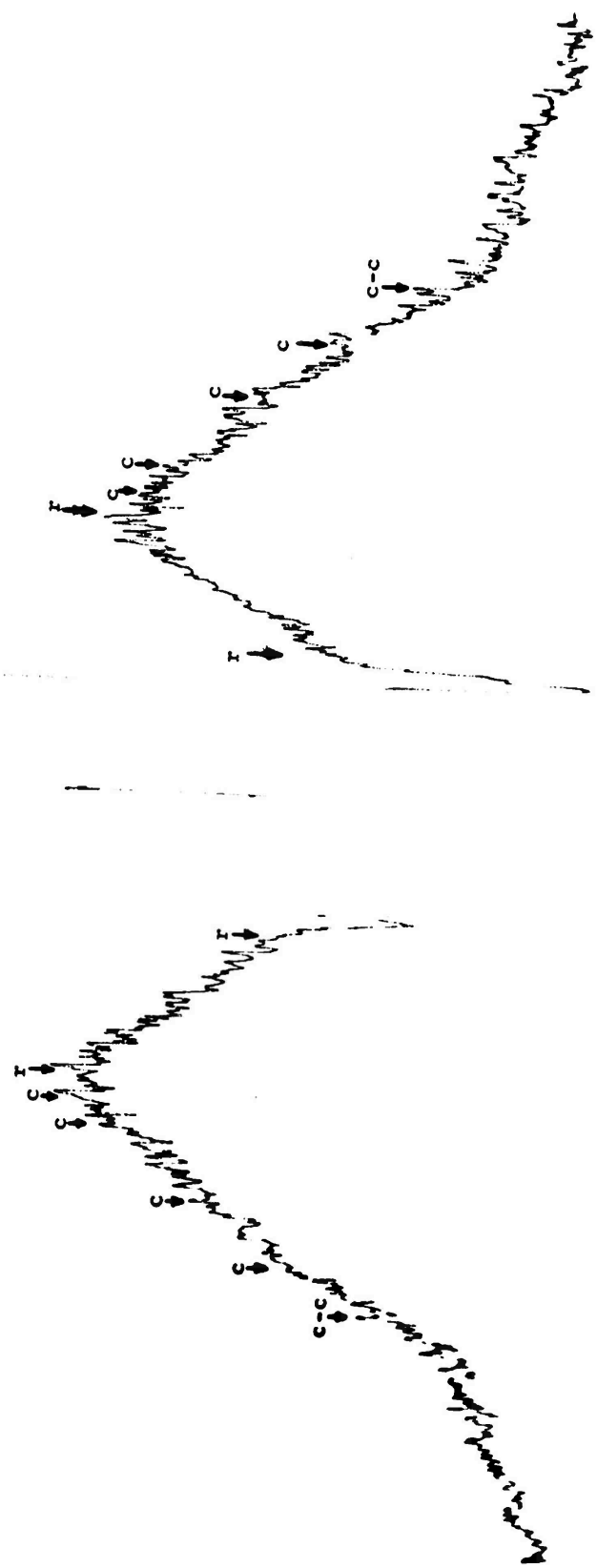


Figure 54. X-Ray Diffraction Densitometer Patterns of BC323

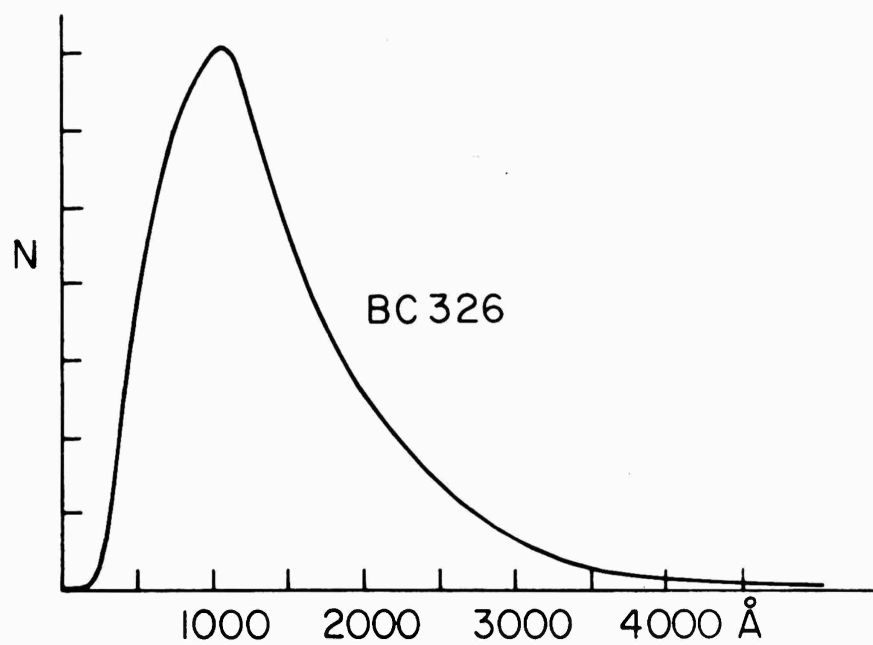
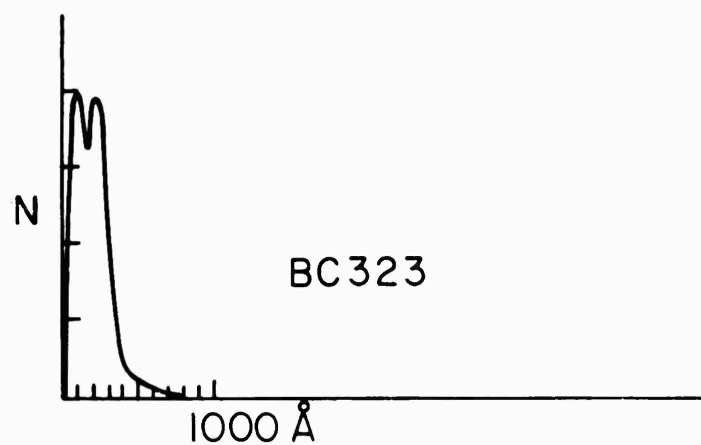


Figure 55. Relative Frequency N as a Function of Diameter of Surface Features

4. SUMMARY

The fracture of plastics under impulsive stress is sufficiently complicated to require a variety of disciplines in any attempt to gain a better understanding of the processes involved. In this program a flying-plate technique has been used to provide the short duration stress pulses. Initial results showed that the initiation and growth of internal fractures depend on the driver-plate thickness and hence on the pulse duration. If this initial impact pressure is sufficiently low, but above a given threshold value depending on the particular plastic used as target, only a few internal fractures are formed. At higher pressures more fractures are formed, and if these are sufficiently numerous they can join or overlap to cause detached spallation.

Two plastics have been studied in detail, both of which are based on an epoxy-novolak structure. One (BC323) is relatively rigid, and at room temperature is well below its glass transition temperature. The other (BC326), containing a plasticizer, is relatively rubbery at room temperature. The threshold IIP for fracture in the BC323, by pulses lasting about a microsecond, is about 0.4 to 0.6 kb; whereas that for the BC326, while not accurately located, is somewhat above 1 kb and perhaps near 1.4 kb. To determine these values, it has been necessary to obtain the equations of state for these materials. This work has revealed that while the plots of shock speed versus particle speed are not linear except over a limited range, particularly for BC326, best fits to the data indicate the BC326 resin to be slightly less compressible than the BC323 resin. This is contrary to first expectation, but is supported by x-ray diffraction data which show that the more rubbery BC326 is somewhat better ordered than the more rigid BC323. Also, the density of BC326 (1.27 gm/cc) is slightly greater than that of BC323 (1.24 gm/cc).

The need to know more about the shape and nature of the stress pulse to define better the initiation of fracture has led to the use of a quartz crystal transducer technique for determining pulse characteristics. While such a method can yield information on the rate of rise of the compressive pulse, and in principle should yield the shape of such a pulse as it crosses the target-crystal interface, it does not reveal directly that nature of the reflected tensile pulse in the region where fracture occurs. Nevertheless, the quartz crystal method has been useful, and has shown that the compressive wave fronts in BC326 develop a more gradual slope than do the fronts of similar pulses in BC323. Also, there is no evidence of precursors in the pulses in BC326, whereas these nearly always appear in pulses in BC323.

The use of multiple crystals at various depths in BC323 has shown that the pulse shape changes very little in going from one target thickness to another (e.g., 1/2 inch to 1 inch). That is, development of wave front slope is most rapid during the first part of the pulse travel.

Very thin, stationary drivers have been hit by moving targets (containing quartz crystals) in an attempt to study the tails of the compressive pulses. On the more usable oscilloscope traces obtained from such impacts, it appears that for an aluminum driver and a BC323 target the compressive stress does not drop to zero at the end of one reverberation in the driver. Rather, the stress drops in stepwise fashion during the recording time of the crystal. For a single experiment using BC326 target and driver in similar manner, it appears that the stress drops much more quickly.

The quartz crystal technique has demonstrated the need to attain extremely high simultaneity of impact to obtain sharp-rising pulses. Considerable effort in the program has been devoted to this aspect, with the magnitude of the problem being increased by the large diameter (6 inches) of the compressed-air gun used.

Attempts have been made to supplement the information on stress profiles gained from the quartz crystals by using a light-transmission technique, the object being to utilize the change in optical density of a material as a stress wave moves through it. In most of the signals obtained, however, it appears that light received by the photomultiplier is increased rather than decreased on impact of the target. This has led to interesting speculation on the possible production of light during impact by either mechanical, thermal, or electrical luminescent effects. The study of such effects could be extensive, however, and lies well beyond the scope of this program.

In the study of fracture surface morphology, some striking differences, as well as a few similarities, are exhibited by the BC323 and BC326 resins. The types of fractures obtained in the more rigid material are more predictable than those obtained in the more rubbery material. For example, in BC323 the fractures are invariably disk-shaped and well defined, and the radii of these fractures are directly dependent on driver thickness ($R \cong 0.25 T$). The fracture surfaces often contain many parabolas indicative of the main crack front intercepting secondary fronts emanating from sites of high stress concentration.

The fractures in BC326, on the other hand, range from star-shaped conical ruptures, resembling the results of tearing, to circular, well-defined structures practically devoid of features. Parabolas in the surface are generally absent and the fracture radii are not directly dependent on driver thickness.

Complete correlation of fracture characteristics with stress-pulse profiles cannot yet be made with confidence; since the profiles are not known with respect to the tensile stress in the region of damage. However, comparison of the areas of fracture for the two resins during the rise of the tensile pulse are consistent with the profiles which have been measured. That is, this area is relatively larger, for a single wave transit near threshold, in BC326 than in BC323, and this may be the result of the more gradually sloping wave front in the rubbery material.

REFERENCES

1. Barry, W. T., Semon, H. W., Berry, J. P., Lucy, F. A., and Flom, D. G., "Behavior of Plastics Under Impulsive Stress," Interim Final Report, AFSWC TDR 62-85, September 21, 1962.
2. Jones, O. E., Neilson, F. W., and Benedick, W. B., "Dynamic Yield Behavior of Explosively Loaded Metals Determined by a Quartz Transducer Technique," J. Appl. Phys., 33, 3224 (1962).
3. Rice, M. H., McQueen, R. G. and Walsh, J. M., "Compression of Solids by Strong Shock Waves," pp. 1-63 in Solid State Physics, vol. 6, Academic Press, 1958.
4. McQueen, R. G., and Marsh, S. P., "Equation of State for Nineteen Metallic Elements from Shock-Wave Measurements to Two Megabars," J. Appl. Phys. 31, 1253 (1960).
5. Al'tshuler, L. V., Krupnikov, K. K., and Brazhnik, M. I., "Dynamic Compressibility of Metals under Pressures from Four Hundred Thousand to Four Million Atmosphere," Zhur. Eksp. Teor. Fiz. 34, 886 (1958). Translation Sov. Phys. JETP 34 (7), 614 (1958).
6. Richardson, E. G., Relaxation Spectrometry, North Holland or Interscience 1957.
7. Ferry, J. D., Viscoelastic Properties of Polymers, Wiley 1961.
8. Dank, M. et al., "Material Responses to Microsecond Impulses Produced by Explosives," (Title Unclassified, Report Secret Restricted Data), AFSWC-TR-61-50, Air Force Special Weapons Center 12 July 1961.
9. Mason, W. P., Physical Acoustics and the Properties of Solids, van Nostrand 1958.
10. Fowles, G. R., "Shock Wave Compression of Hardened and Annealed 2024 Aluminum," J. Appl. Phys., 32, 1475 (1961).
11. Berry, J. P., "Some Kinetic Considerations of the Griffith Criterion for Fracture - I. Equations of Motion at Constant Force," J. Mech. Phys. Solids, 8, 194 (1960).

REFERENCES (Cont'd)

12. Kolsky, H., "Fractures Produced by Stress Waves," p. 281, Fracture, Averback, B. L., et al., ed., Technology Press and John Wiley & Sons, 1959, New York.
13. Berry, J. P., "Fracture Processes in Polymeric Materials. III. Topography of Fracture Surfaces of Poly (Methyl Methacrylate)," J. Appl. Phys., 33, 1741 (1962). Also "The Morphology of Polymer Fracture Surfaces," GE Research Laboratory Report No. 63-RL-(3396C), July 1963.
14. Bueche, F., "Tensile Strength of Plastics: Effects of Flaws and Chain Relaxation," J. Appl. Phys., 29, 1231 (1958).

DISTRIBUTION

No. cys

MAJOR AIR COMMANDS

1	AFSC (SCT), Andrews AFB, Wash, DC 20331
1	AUL, Maxwell AFB, Ala 36112
1	USAFIT (USAF Institute of Technology), Wright-Patterson AFB, Ohio 45443
1	USAFA, United States Air Force Academy, Colo 80840

AFSC ORGANIZATIONS

1	FTD (Library), Wright-Patterson AFB, Ohio 45433
1	ASD (ASNRR, Tech Info Ref Br., Reports Div.), Wright-Patterson AFB, Ohio 45433

KIRTLAND AFB ORGANIZATIONS

1	AFSWC (SWEH), Kirtland AFB, NM 87117
	AFWL, Kirtland AFB, NM 87117
10	(WLL)
2	(WLRP)

OTHER AIR FORCE AGENCIES

1	Director, USAF Project RAND, ATTN: RAND Physics Division, via: Air Force Liaison Office, The RAND Corporation, 1700 Main Street, Santa Monica, Calif 90406
1	AFOAR, Bldg T-D, Wash, DC 20333
1	AFOSR, Bldg T-D, Wash, DC 20333

ARMY ACTIVITIES

1	Chief of Research and Development, Department of the Army (Special Weapons and Air Defense Division), Wash, DC 20310
1	Director, Ballistic Research Laboratories (Library), Aberdeen Proving Ground, Md 21005

NAVY ACTIVITIES

1	Commanding Officer and Director, David Taylor Model Basin, Wash 7, DC
1	Commander, Naval Ordnance Laboratory, ATTN: Dr. Rudlin, White Oak, Silver Spring, Md
1	Director, Special Projects, Dept. of the Navy, Wash 25, DC
1	Office of Naval Research, Wash 25, DC

DISTRIBUTION (cont'd)

No. cys

OTHER DOD ACTIVITIES

1	Chief, Defense Atomic Support Agency (Document Library), Wash, DC 20301
20	Hq Defense Documentation Center for Scientific and Technical Information (DDC), Bldg 5, Cameron Sta, Alexandria, Va 22314

AEC ACTIVITIES

1	Sandia Corporation (Information Distribution Division), Box 5800, Sandia Base, NM 87115
1	Sandia Corporation (Technical Library), P.O. Box 969, Livermore, Calif 94551
1	University of California Lawrence Radiation Laboratory (Technical Information Division), P.O. Box 808, Livermore, Calif 94551
1	Director, Los Alamos Scientific Laboratory (Helen Redman, Report Library), P.O. Box 1663, Los Alamos, NM 87554
1	Brookhaven National Laboratory, Upton, Long Island, NY
1	Oak Ridge National Laboratory (Tech Library), Oak Ridge, Tenn 37831
1	Argonne National Laboratory (Tech Library), 9700 S. Cass Ave., Argonne, Ill 60440

OTHER

1	OTS, Department of Commerce, Wash 25, DC
1	General Electric Company, MSD, ATTN: Dr. F. A. Lucy, Room M9505, P.O. Box 8555, Philadelphia 1, Pa
1	Official Record Copy (Lt Brightman, WLRPX)